Title

Multi-carrier Coupling and Hot Carrier Dynamics at Interfaces and Surfaces

Author

Ge, Yijun

Publication Date

2022

Peer reviewed|Thesis/dissertation

UNIVERSITY OF CALIFORNIA

Los Angeles

Multi-carrier Coupling and Hot Carrier Dynamics at Interfaces and Surfaces

A dissertation submitted in partial satisfaction

of the requirements for the degree

Doctor of Philosophy in Mechanical Engineering

by

Yijun Ge

2022

ABSTRACT OF THE DISSERTATION

Multi-carrier Coupling and Hot Carrier Dynamics at Interfaces and Surfaces

by

Yijun Ge
Doctor of Philosophy in Mechanical Engineering
University of California, Los Angeles, 2022
Professor Timothy S. Fisher, Chair

Electrons are the major heat carriers in metals, as are phonons in semiconductors. The role of spin waves (magnons) in thermal transport problems has attracted attention in recent years with the discovery of spin Seebeck effects (SSE) in spintronics. Interactions among these particles or excitations are the origin of many fascinating phenomena and the focus of this work. Despite the computational cost, first-principles calculations use fewer approximations and no fitting parameters in comparison to semi-classical methods; therefore they produce more reliable results. Chapter 1 considers the theory of electron-electron, electron-phonon and phonon-magnon couplings from first principles. Chapter 2 reports first-principles calculations of electron-phonon coupling in bilayer graphene and the corresponding contribution to carrier scattering. At the phonon Γ point, electrons with energies less than 200 meV are scattered predominantly by LA$'$ and TA$'$ modes while higher-energy electron scattering is dominated by optical phonon modes. Based on a two-temperature model, heat transfer from electrons with an initial temperature of 2000 K to the lattice (phonons) with an initial temperature of 300 K is computed, and in the overall relaxation process, most of this energy scatters into K-point phonon optical modes due to their strong coupling with electrons and their high energies. A Drude model is used to calculate photoconductivity for bilayer graphene with different doping levels. Good agreement with prior experimental trends for both the real and imaginary components of photoconductivity confirms the model's applicability. The effects of doping levels and electron-phonon scattering on photoconductiviy are analyzed. We also extract

acoustic and optical deformation potentials from average scattering rates obtained from density functional theory (DFT) calculations and compare associated photoconductivity calculations with DFT results. The comparison indicates that momentum-dependent electron-phonon scattering potentials are required to provide accurate predictions. Chapter 3 combines first-principles calculations, spin-lattice dynamics and the non-equilibrium Green's function (NEGF) method to compute thermal boundary conductance at a three-dimensional Co-Cu interface, considering spin-lattice interactions. Spin-lattice interactions are quantified through exchange interactions between spins, and the exchange constants are obtained from first principles. Equilibrium molecular dynamics (EMD) is used to calculate heat flux across the interface after the spin and lattice subsystems are in equilibrium. Because of the weak interaction between Co and Cu layers adjacent to the interface, spin-wave transmission is low. Spins are scattered by phonons inside the Co contact, and interfacial thermal conductance is reduced. We also compare the results to the NEGF method. Phonon and magnon scattering rates are incorporated into Büttiker probes attached to the device. NEGF results exhibit a similar trend in thermal boudary conductance with spins included. The Green's function is solved recursively; therefore it can be applied to large devices. Chapter 4 investigates electronic and optical properties of single layer and bilayer armchair graphene nanoribbons using the first-principles method. An increase of nanoribbon width reduces the band gap and causes a redshift in photon absorption energy. We find that the $3n+2$ family nanoribbons have the smallest band gaps and lowest onset photon absorption energy among all three families considered due to the most π-conjugation indicated by the exciton wavefunctions. We also compare the bilayer α and β alignments of armchair graphene nanoribbons with their single-layer counterparts. The extra layer of these nanoribbons reduces the band gap and the onset photon absorption energy, and the difference between the α alignment and the single-layer configuration is more significant than that of the β alignment and the single layer. Our calculations indicate that the optical properties of graphene nanoribbons depend on the details of atomic structures, including nanoribbon width, edge alignment, and number of layers. Chapter 5 investigates the photo-thermal effect in the methane decomposition process. By calculating electronic transitions in polycyclic aromatic hydrocarbons from TDDFT, we extract the absorption coefficients. Further, the absorption coefficients are mapped to the experimental light intensity profile to predict the total absorption spectra.

Temperature rise can be further induced by calculating heat capacities of the polycyclic aromatic hydrocarbons using frequencies of the vibrational modes.

The dissertation of Yijun Ge is approved.

Jayathi Y. Murthy

Yongjie Hu

Jaime Marian

Timothy S. Fisher, Committee Chair

University of California, Los Angeles

2022

TABLE OF CONTENTS

LIST OF FIGURES

LIST OF TABLES

ACKNOWLEDGMENTS

I would like to thank my advisor Professor Fisher for his guidance, patience and help throughout the years. He taught me knowledge, writing skills, presentation skills and so much more. I will always be grateful that I have such a wonderful, understanding and kind advisor. I also want to thank my other committee members, Professor Murthy, Professor Hu and Professor Marian for giving me valuable advice on my research and being very supportive during my entire PhD.

I would like to thank Professor Emily Carter for her suggestions on photocatalysis modeling. I also want to thank Professor Gregory Carman and his students Matthew and Yuching for the fruitful discussions on nanomagnetics. I would like to thank Professor Zhiting Tian for her advice on molecular dynamics simulations. I would like to thank Professor Tillmann Kubis for the productive discussions on modeling 2-D materials. I learned non-equilibrium Green's function, transport mechanisms and solid state physics in Professor Supriyo Datta, Professor Mark Lunstrom and Professor Muhammad Ashraful Alam's courses. I would like to thank them for their great lectures that have helped me significantly in my own research.

Dr. Sridhar Sadasivam helped me a lot in learning Density Functional Theory and running simulations in general. Dr. Yanguang Zhou has always been a great person to talk to regarding multi-scale simulations. I benefited a lot from all the discussions we had and was always encouraged by his enthusiasm towards research and life. I want to thank all the members of the NTRG group, Yuan, Kaiyuan, Bryce, Ujash, David, Mostafa, Abdullah, Indronil, Akshay and many others.

I would like to acknowledge UCLA hoffman2 resources and Xsede high performance computation resources.

Last but not the least, I want to thank my family especially my parents for their support and love. They have always been there for me when there is difficulty and when I'm stressed out. I want to thank three of my grandparents who have passed away when I was in graduate school. I still remember them smiling at me and asking me to take good care of myself even when they were feeling very sick. I'm forever grateful that they loved me so much.

VITA

2014-2017	M.S. in Mechanical Engineering
	Purdue University, West Lafayette, IN
2010-2014	B.E. in Naval Architecture and Ocean Engineering
	Huazhong University of Science and Technology, Wuhan, China

PUBLICATIONS

Ge, Y., Zhou, Y., & Fisher, T. S. (2021). Thermal boundary conductance across Co/Cu interfaces with spin–lattice interactions. *Journal of Applied Physics, 130*(23), 235108.

Ge, Y., & Fisher, T. S. (2020). Photoconductivity calculations of bilayer graphene from first principles and deformation-potential approach. *Physical Review B, 101*(23), 235429.

Zhou, Y., Tranchida, J., Ge, Y., Murthy, J., & Fisher, T. S. (2020). Atomistic simulation of phonon and magnon thermal transport across the ferromagnetic-paramagnetic transition. *Physical Review B, 101*(22), 224303.

CHAPTER 1

Introduction

1.1 Introduction

Three major carriers exist in solid state systems: electrons, phonons and magnons. We address them as 'carriers' as they carry charge, energy or spin; and their continuous motions produce electric, thermal or spin currents. The coupling among carriers is the origin of many intriguing phenomena.

Intrinsic photocurrent has been detected at the edge of charge-neutral graphene sheets, as opposed to doped graphene. Due to graphene's unique linear dispersion, only collinear electron-electron scattering is allowed at the charge-neutral point in order to satisfy momentum and energy conservation; therefore the reduction of electron-electron scattering preserves photocurrent [1]. In fact, the electron-electron interaction is a key factor in designing optoelectronics. For example, plasmonics have received great interest for their ability to concentrate light in a region smaller than the wavelength of the electromagnetic waves. This strong light-matter interaction enables applications of plasmonics in photodetectors, lasers, and optical microscopy. One major limitation to the performance of such devices is the decay of plasmons. Other than impurity scattering, electron-electron and electron-phonon interactions are also possible decay channels.

Electron-phonon coupling is well known to be responsible for superconductivity in conventional superconductors. While Bardeen, Cooper and Schrieffer (BCS) theory works in the weak electron-phonon coupling regime [2], Eliasherg theory [3][4] is applicable for materials with strong electron-phonon coupling. The fundamental quantity in describing the electron-phononn interaction is the Eliashberg function $\alpha^2(\omega)$, the integral of which over the frequency range can be ex-

perimentally extracted from angle-resolved photoemission spectroscopy (ARPES). The effects of electron-phonon interactions on devices' electric and thermal properties have always been important in their design. In bulk metals, electron-phonon scattering is the primary source of reduced electron mobility and thermal conductivity. As temperature increases, electron-phonon scattering rates increase accordingly and further deteriorate transport properties. However, theoretical work on Si-$CoSi_2$ interfaces has indicated that electron-phonon interactions across the interface actually increase the thermal boundary conductance, and a large amount of the contribution comes from the delocalized phonon modes [5].

The spin Seebeck effect refers to the generation of spin voltage driven by a temperature gradient in a ferromagnetic material. Spin current was detected by attaching a Pt wire to a $Ni_{81}Fe_{19}$ layer [6] with a temperature gradient applied to the ends using the inverse-spin-Hall effect [7, 8]. The spin voltage was observed in different positions of the $Ni_{81}Fe_{19}$ layer, which spans a few millimeters, much longer than the spin-diffusion length of $Ni_{81}Fe_{19}$. The long range characteristic of the spin current generated by spin Seebeck effect suggests its great potential for making spin-based devices [9, 10, 11]. Later, the longitudinal spin Seebeck effect was observed along the temperature gradient in an experiment using $Y_3Fe_5O_{12}$(YIG)/Pt [12], suggesting that the spin wave is the carrier of spin current instead of conduction electrons because YIG is an insulator.

More and more interest has emerged in studying the mechanism of the spin Seebeck effect, and different theories have been proposed in recent years. Xiao et al. [13] presented a theory based on spin pumping at a ferromagnet and normal metal interface driven by the temperature difference between magnons and electrons/phonons. Their theory predicts the correct spatial scale of the spin Seebeck effect in YIG while it fails for the ferromagnetic metal permalloy. The authors assumed the cause for the failure in permalloy to be inaccurate magnon-magnon scattering and magnon-phonon scattering times used in the calculations, and the existence of conduction electrons in permalloy. Adachi et al. [14] explained the spin Seebeck effect in YIG using linear response theory considering local spin injection into the normal metal from YIG driven by the temperature difference between YIG and a normal metal and the non-local magnon-mediated spin injection due to the temperature difference between magnons and phonons inside YIG. The linear response

theory framework can be generalized to include phonons and electrons; therefore the method can be extended to metals and semiconductors. Uchida et al. [15] reported spin Seebeck effect in a $Ni_{81}Fe_{19}$/Pt wire on an electrically and magnetically insulating sapphire substrate with a uniform temperature gradient applied along the sapphire substrate and that the measured voltage is linearly proportional to temperature gradient. It was indicated that the spin Seebeck effect is phonon-mediated in this experiment because there are no electrons or magnons transmitted through the insulating substrate. Magnon distributions in the $Ni_{81}Fe_{19}$ wire are modulated by non-equilibrium phonons through magnon-phonon interactions, causing spin pumping from the $Ni_{81}Fe_{19}$ wire to the Pt wire. A comparison experiment with $Ni_{81}Fe_{19}$/Pt wires on a silica-glass substrate observed little spin voltage with the same temperature gradient, confirming that the spin Seebeck effect is phonon-mediated. The silica-glass substrate has a large acoustic impedance mismatch with the $Ni_{81}Fe_{19}$ wire, and phonon waves are less likely to propagate. Further, the authors directly injected acoustic waves to a YIG slab on a piezoelectric actuator and observed a dip in the measured voltage curve around the piezoelectric resonance frequency, proving the effect of phonon-magnon coupling on the spin voltage generated by the spin Seebeck effect.

One circumstance involving multiple coupling mechanisms is the metal-insulator phase transition observed in transition metal oxides. A debate exists over its origin between Peierls-type (electron-phonon) and Mott-type (electron-electron) mechanisms [16][17]. Peierls transitions involve symmetry-breaking of the structure and open a gap at the zone boundary. Mott transitions are a competition between Coulomb repulsion and electron hopping energy. If the distance between nuclei is reduced, then electrons have more hopping energy to overcome the repulsion, and the system becomes conducting. On the other hand, adding electrons/holes screens the Coulomb repulsion and promotes the non-conducting to conducting transition. Because distorting of the lattice alters the structure and at the same time the interactions between nuclei, determining whether the Peierls or Mott transition is the driving force to the phase transition is difficult; therefore both mechanisms must be considered in the study of such problems.

Density functional theory (DFT) is a mean-field method in which electron-electron Coulomb interactions are treated as repulsion between one electron and the average charge density in its

surroundings, neglecting the self-interaction. Exchange and correlation effects are all lumped into an approximate term called the exchange-correlation potential. This causes problems especially in strongly correlated systems. Taking VO_2 for example, conventional DFT predicts the monoclinic phase VO_2 to be a metal instead of an insulator. By adding the U correction which explicitly adds an on-site Coulomb repulsion, a band gap opens. Magnons interact via the exchange energy, which is the J term in the Heisenberg model. However, the exchange is not exact in DFT; therefore the usually method of extracting J by calculating the difference between spin-parallel and spin-antiparallel systems is also an estimate. Hartree-Fock theory provides the exact exchange through a Slater determinant approach but leaves the correlation problem unaddressed.

This chapter introduces the theory of electron-electron, electron-phonon and phonon-magnon interactions, and related challenges associated with first-principles calculations.

1.2 Electron-electron interactions

While the static Density Functional Theory (DFT) reliably predicts ground-state properties including ground-state energies, atomic structures, phase stability and electron densities, it underestimates electronic band gaps and is unable to accurately capture optical properties [18, 19]. Besides the fact the exchange-correlation potentials are not exact in the static DFT, the independent particle Kohn-Sham band gap does not represent the fundamental band gap which is essentially an excited-state property in a many-body system. Electrons are removed from the system in photoemission processes and added to the system in reverse photoemission processes. The interactions between the electrons and the charged system can not be accounted for in static DFT theory. In optical obsorption processes, electrons are excited from occupied states to unoccupied states leaving holes behind. The system remains charge neutral; however the carriers around the excited electrons adjust their positions due to repulsion or attraction. This screening effect reduces the effective range and magnitude of the Coulomb potential. To consider interactions between excited electrons and the remaining system, methods like Time-dependent Density Functional Theory (TDDFT) and Many-body Perturbation Theory (MBPT) are more suitable to describe excited state properties.

We start from the static DFT, and then introduce TDDFT within the framework of linear response theory and MBPT with the GW approximation.

1.2.1 Static density functional theory

Within the Born-Oppenheimer approximation, the solution to the time-independent Schrödinger equation reduces to the electron band structure problem.

$$\hat{H}_e \Psi_n(\mathbf{r};\mathbf{R}) = \varepsilon_n(\mathbf{R})\Psi_n(\mathbf{r};\mathbf{R}) \tag{1.1}$$

where the electron Hamiltonian $\hat{H}_e$ consists of three parts: kinetic energy ($\hat{T}_\mathbf{r}$), interaction with the nuclei ($\hat{H}_{\mathbf{r};\mathbf{R}}$), and interaction within electrons ($\hat{V}_\mathbf{r}$):

$$\hat{H}_e = \underbrace{-\sum_i \frac{1}{2}\nabla^2}_{\hat{T}_\mathbf{r}} \underbrace{-\sum_{i,I} \frac{Z_I}{|\mathbf{r}_i - \mathbf{R}_I|}}_{\hat{V}_{\mathbf{r};\mathbf{R}}} + \underbrace{\frac{1}{2}\sum_{i\neq j} \frac{1}{|\mathbf{r}_i - \mathbf{r}_j|}}_{\hat{V}_\mathbf{r}} \tag{1.2}$$

Here, i and j run over all electron degrees of freedom, and I runs over nuclei degrees of freedom.

The Hohenberg-Kohn theorem states that total energy is a unique function of electron density, and ground-state density can be determined by minimizing the total energy. In principle, this is a many-body problem since the wave function relies on knowledge of all particles' distribution information; therefore the complexity of the problem grows tremendously with increases in the number of particles, making this kind of solution impractical. The Kohn-Sham ansatz provides a way to decompose the many-body wave function into a set of non-interacting particle wave functions, and constitutes the foundation of many modern DFT codes.

$$\Psi(\mathbf{r}_1, \mathbf{r}_2, \cdots, \mathbf{r}_n) \Rightarrow \psi_1(\mathbf{r}_1)\psi_2(\mathbf{r}_2)\cdots\psi_n(\mathbf{r}_n) \tag{1.3}$$

The one-particle Kohn-Sham Hamiltonian is written as:

$$\hat{H}_{KS}[\rho] = \underbrace{T_0[\rho](\mathbf{r})}_{\substack{one-particle \\ kinetic\ energy}} + \int dr\rho(\mathbf{r})v_{ext}(\mathbf{r}) + E_H[\rho](\mathbf{r}) + E_{xc}[\rho](\mathbf{r}) \tag{1.4}$$

$$v_{ext}(\mathbf{r}) = -\sum_I \frac{Z_I}{\mathbf{r} - \mathbf{R}_I} \tag{1.5}$$

$$E_H[\rho] = \frac{1}{2}\int\int d\mathbf{r}d\mathbf{r}' \frac{\rho(\mathbf{r})\rho(\mathbf{r}')}{|\mathbf{r} - \mathbf{r}'|} \tag{1.6}$$

Here v_{ext} is the external potential associated with the nuclei, E_H is the classical Coulomb potential (also known as the Hartree potential), and E_{xc} is the exchange-correlation term. The exchage part takes care of the anti-symmetric nature of electron wave functions by interchanging two electrons, and the correlation part is associated with electron correlations. The difference between the many-body kinetic energy and one-particle kinetic energy is lumped into the exchange-correlation term.

1.2.2 Time-dependent density functional theory and linear response theory

Variations in charge density caused by external perturbations induce Hartree and exchange-correlation variations that screen the effects of external perturbations. The electron screening effects are considered through the calculation of the dielectric function ε. The dielectric function relates the external potential v_{ext} to the total Kohn-Sham potential v_{KS} via:

$$v_{KS} = \varepsilon^{-1} v_{ext} \tag{1.7}$$

ε can be obtained from the density-density response function χ by applying TDDFT and linear response theory. The basis of TDDFT is the Runge-Gross theorem [20] which states that a one-to-one mapping exists between the time-dependent external potential $v_{ext}(\mathbf{r},t)$ and the time-dependent charge density $\rho(\mathbf{r},t)$ of the system.

We first introduce the time-dependent Kohn-Sham equation:

$$i\frac{\partial \psi(\mathbf{r},t)}{\partial t} = \left\{ -\frac{\hbar^2}{2m}\nabla^2 + v_{KS}[\rho](\mathbf{r},t) \right\} \psi(\mathbf{r},t) \tag{1.8}$$

where v_{KS} is the Kohn-Sham potential and consists of three parts: the external potential $v_{ext}(\mathbf{r},t)$, the Hartree potential $v_H[\rho](\mathbf{r},t)$, and the exchange-correlation potential $v_{xc}[\rho](\mathbf{r},t)$.

$$\begin{aligned} v_{KS}[\rho](\mathbf{r},t) &= v_{ext}(\mathbf{r},t) + v_H[\rho](\mathbf{r},t) + v_{xc}[\rho](\mathbf{r},t) \\ v_H[\rho](\mathbf{r},t) &= e^2 \int d^3\mathbf{r}' \frac{\rho(\mathbf{r}',t)}{|\mathbf{r}-\mathbf{r}'|} \end{aligned} \tag{1.9}$$

In the framework of linear response theory, we assume the perturbation to the system is small, and the density response to the external perturbation is calculated with the density-density response function χ:

$$\chi(\mathbf{r}t,\mathbf{r}'t') = \frac{\delta\rho(\mathbf{r},t)}{\delta v_{ext}(\mathbf{r}',t')} \tag{1.10}$$

From Eq. (1.10), we can see that the density response at position $\mathbf{r}$ and time t depends on the perturbation at position $\mathbf{r}'$ and time $t'(t' < t)$; therefore the density response function is non-local and retarded. The density variation can also be computed in a non-interacting Kohn-Sham system:

$$\chi^0(\mathbf{r}t,\mathbf{r}'t') = \frac{\delta\rho(\mathbf{r},t)}{\delta v_{KS}(\mathbf{r}',t')} \tag{1.11}$$

Here χ^0 is the non-interacting density-density response function (also known as irreducible polarizability) and can be expressed through the Adler-Wiser equation [21]:

$$\chi^0(\mathbf{r},\mathbf{r}',\omega) = \frac{2}{\Omega}\sum_{i\neq j}(f_i - f_j)\frac{\psi_i^\dagger(\mathbf{r})\psi_j(\mathbf{r})\psi_j^\dagger(\mathbf{r}')\psi_i(\mathbf{r}')}{\varepsilon_i + \omega - \varepsilon_j + i\eta} \tag{1.12}$$

In reciprocal space, the Fourier transform of Eq. (1.12) is expressed as:

$$\chi^0_{\mathbf{G},\mathbf{G}'}(\mathbf{q},\omega) = \frac{2}{\Omega}\sum_{\mathbf{k},v,v'}(f_{v\mathbf{k}} - f_{v'\mathbf{k}+\mathbf{q}})\frac{\langle\psi_{v,\mathbf{k}}|\, e^{-i(\mathbf{q}+\mathbf{G})\mathbf{r}}\,|\psi_{v',\mathbf{k}+\mathbf{q}}\rangle\langle\psi_{v',\mathbf{k}+\mathbf{q}}|\, e^{i(\mathbf{q}+\mathbf{G}')\mathbf{r}}\,|\psi_{v,\mathbf{k}}\rangle}{\varepsilon_{v,\mathbf{k}} - \varepsilon_{v',\mathbf{k}+\mathbf{q}} + \hbar\omega + i\eta} \tag{1.13}$$

Here, Ω is the volume, f is the Fermi-Dirac distribution, and η is the broadening parameter.

Defining an exchange-correlation kernel $f_{xc}[\rho](\mathbf{r},\mathbf{r}',t-t') = \dfrac{\delta v_{xc}(\mathbf{r},t)}{\delta\rho(\mathbf{r}',t')}$ and inserting Eq. (1.9) into Eq. (1.11), we obtain a Dyson equation with the use of Eq. (1.10):

$$\chi(\mathbf{r},\mathbf{r}',\omega) = \chi^0(\mathbf{r},\mathbf{r}',\omega) + \int d^3\mathbf{r}_1 d^3\mathbf{r}_2 \chi^0(\mathbf{r},\mathbf{r}_1,\omega)\{\frac{e^2}{|\mathbf{r}_1-\mathbf{r}_2|} + f_{xc}(\mathbf{r}_1,\mathbf{r}_2,\omega)\}\chi(\mathbf{r}_2,\mathbf{r}',\omega) \quad (1.14)$$

A Fourier transform of Eq. (1.14) produces:

$$\chi_{\mathbf{G},\mathbf{G}'}(\mathbf{q},\omega) = \chi^0_{\mathbf{G},\mathbf{G}'}(\mathbf{q},\omega) + \sum_{\mathbf{G}_1,\mathbf{G}_2} \chi^0_{\mathbf{G},\mathbf{G}_1}(\mathbf{q},\omega)\{\frac{4\pi e^2}{|\mathbf{q}+\mathbf{G}||\mathbf{q}+\mathbf{G}'|} + f_{xc,\mathbf{G}_1,\mathbf{G}_2}(\mathbf{q},\omega)\}\chi_{\mathbf{G}_2,\mathbf{G}'}(\mathbf{q},\omega) \quad (1.15)$$

Inserting Eq. (1.9), (1.10) and (1.11) into Eq. (1.7), we obtain:

$$\varepsilon^{-1}_{\mathbf{G},\mathbf{G}'}(\mathbf{q},\omega) = \delta_{\mathbf{G},\mathbf{G}'} + \{\frac{4\pi e^2}{|\mathbf{q}+\mathbf{G}||\mathbf{q}+\mathbf{G}'|} + f_{xc,\mathbf{G},\mathbf{G}'}(\mathbf{q},\omega)\}\chi_{\mathbf{G},\mathbf{G}'}(\mathbf{q},\omega) \quad (1.16)$$

and

$$\varepsilon_{\mathbf{G},\mathbf{G}'}(\mathbf{q},\omega) = \delta_{\mathbf{G},\mathbf{G}'} - \{\frac{4\pi e^2}{|\mathbf{q}+\mathbf{G}||\mathbf{q}+\mathbf{G}'|} + f_{xc,\mathbf{G},\mathbf{G}'}(\mathbf{q},\omega)\}\chi^0_{\mathbf{G},\mathbf{G}'}(\mathbf{q},\omega) \quad (1.17)$$

The central functionals in TDDFT are the exchange-correlation potential v_{xc} and the exchange-correlation kernel f_{xc}. The exact form of the exchange-correlation kernel is unknown, and approximations are required for TDDFT calculations. In the Random Phase Approximation (RPA) [22, 23], electrons are treated as independent particles, and exchange-correlation effects are neglected with $f_{xc} = 0$. This is similar to Hartree-Fock theory in the static system; therefore TDDFT within RPA is also called Time-dependent Hartree-Fock Theory (TD-HF).

Another widely used approximation of the exchange-correlation kernel in TDDFT is the adiabatic local density approximation (ALDA) where

$$f^{ALDA}_{xc}(\mathbf{r},\mathbf{r}') = \delta(\mathbf{r}-\mathbf{r}')\frac{\delta v^{LDA}_{xc}(\rho(\mathbf{r}),\mathbf{r})}{\delta\rho(\mathbf{r})} \quad (1.18)$$

In electron energy loss spectroscopy (EELS) calculations, both ALDA and RPA quantitatively match experimental results. In finite systems, ALDA performs well in predicting optical absorp-

tion spectra and improves the result of RPA. However, in extended systems the optical absorption spectra predicted by ALDA shows a large discrepancy from experiments due to incorrect asymptotic behavior of the ALDA potential. The Kohn-Sham gap is smaller than the fundamental band gap, and ALDA does not account for the excitonic effects [24, 25, 26].

1.2.3 GW and Bethe-Salpeter equation (BSE)

Despite the simplicity of TDDFT, the optical properties predicted by TDDFT greatly depend on the choice of the exchange-correlation potential and exchange-correlation kernel. The many-body Green's function, on the other hand, explicitly calculates the energies of adding and removing electrons and is more straightforward in terms of analysing the physics. The exchange-correlation potential is contained within the non-local and frequency dependent electron self-energy term Σ in the many-body Green's function framework. Adding or removing charges in a system induces the relaxation of wave functions. To account for such a relaxation or response to charge perturbation, the dielectric matrix is used to compute the screened potential induced by the external potential.

In this work, we study the optical properties of graphene nanoribbons in Chapter 4 using GW + BSE methodology within the many-body Green's function framework. Within the GW approximation, electron self-energy is evaluated as the convolution of a single-particle Green's function G and screened Coulomb interaction W:

$$\Sigma(\mathbf{r},\mathbf{r}';\omega) = i\int \frac{d\omega'}{2\pi} e^{-i\eta\omega'} G(\mathbf{r},\mathbf{r}';\omega-\omega')W(\mathbf{r},\mathbf{r}';\omega-\omega') \tag{1.19}$$

where $\eta = 0^+$. The single-particle Green's function is:

$$G(\mathbf{r},\mathbf{r}';\omega) = \sum_{n,\mathbf{k}} \frac{\psi_{n\mathbf{k}}(\mathbf{r})\psi^*_{n\mathbf{k}}(\mathbf{r}')}{\omega-\varepsilon_{n\mathbf{k}}-i\eta} \tag{1.20}$$

and the screened Coulomb potential is expressed as:

$$W(\mathbf{r},\mathbf{r}';\omega) = \int \varepsilon^{-1}(\mathbf{r},\mathbf{r}'';\omega)v(|\mathbf{r}'-\mathbf{r}''|)d\mathbf{r}'' \tag{1.21}$$

In the static limit when $\omega = 0$, the electron self-energy term is decomposed into the an energy-independent Coulomb-hole (COH) term and screened exchange (SEX) term [27]:

$$\Sigma_{COH}(\mathbf{r},\mathbf{r}') = \frac{1}{2}\delta(\mathbf{r},\mathbf{r}')[W(\mathbf{r}-\mathbf{r}') - v(\mathbf{r},\mathbf{r}')] \tag{1.22}$$

$$\Sigma_{SEX}(\mathbf{r},\mathbf{r}') = -\sum_{n\mathbf{k}}^{occ} \phi_{n\mathbf{k}}(\mathbf{r})\phi^*_{n\mathbf{k}}(\mathbf{r}')W(\mathbf{r},\mathbf{r}') \tag{1.23}$$

The COH part of self-energy represents the interaction between the quasi-particle and the potential induced by electron screening around the quasi-particle, and the SEX part of self-energy is the exchange energy with static electron screening. The SEX part requires a summation over occupied states while the δ function in the COH part requires a summation over occupied and unoccupied states [28, 29].

The quasi-particle eigenvalues and wave functions are calculated by solving the Dyson's equation [30]:

$$\left[\frac{-1}{2}\nabla^2 + v_{ext} + v_H + \Sigma(E^{QP}_{n\mathbf{k}})\right]\psi^{QP}_{n\mathbf{k}} = E^{QP}_{n\mathbf{k}}\psi^{QP}_{n\mathbf{k}} \tag{1.24}$$

where $E^{QP}_{n\mathbf{k}}$ and $\psi^{QP}_{n\mathbf{k}}$ are the quasi-particle energies and quasi-particle wave functions, respectively. The quasi-particle energy is evaluated by:

$$E^{QP}_{n\mathbf{k}} = \varepsilon^{DFT}_{n\mathbf{k}} + \langle\psi^{DFT}_{n\mathbf{k}}|\Sigma^{GW}(E^{QP}_{n\mathbf{k}}) - v^{DFT}_{xc}|\psi^{DFT}_{n\mathbf{k}}\rangle \tag{1.25}$$

In this work, we use a zeroth-order G_0W_0 approximation for the calculations of the Green's function and the screened Coulomb interaction. Neither the Green's function nor the screened Coulomb interaction is self-consistently calculated in the Dyson's equation but instead is based on the eigenvalues and wave functions obtained in the static DFT. The quasi-particle energy contributed by exchange-correlation in static DFT is replaced by the electron self-energy in the G_0W_0 approximation. The algorithm of calculating the quasi-particle energy is summarized as follows:

1. Construct the Green's function G_0 with Kohn-Sham eigenvalues and wave functions.

2. Calculate the irreducible polarizability χ^0.

3. Calculate the dielectric function ε.

4. Calculate the screened Coulomb potential W_0.

5. Calculate the self-energy Σ.

6. Solve the Dyson's equation to obtain quasi-particle energies E^{QP}.

While GW accurately predicts quasi-particle energies (including electron ionization energy, electron affinity and band gaps) and matches photoexcitation and inverse photoexcitation measurements well, it does not do a good job in predicting optical absorption, especially in semiconductors and insulators. The GW methodology describes one-particle excitation while optical absorption processes involve two-particle excitation: the excited electron and the Coulomb hole. To account for the interaction between the electron-hole pair, the Bethe-Salpeter equation [31, 32, 33, 34, 35, 36] can be used along with GW quasi-particle energies to simulate optical absorption spectra in charge neutral systems.

The Bethe-Salpeter equation reads:

$$\left(E^{QP}_{c\mathbf{k}} - E^{QP}_{v\mathbf{k}}\right) A^S_{vc\mathbf{k}} + \sum_{v'c'\mathbf{k}'} \langle vc\mathbf{k}| K^{eh} |v'c'\mathbf{k}'\rangle = \Omega^S A^S_{vc\mathbf{k}} \tag{1.26}$$

where $E^{QP}_{c\mathbf{k}}$ and $E^{QP}_{v\mathbf{k}}$ are quasi-particle energies of the conduction and valence band electron states obtained from GW calculations , K^{eh} is the electron-hole interaction kernel, Ω^S is the excitation energy, and $A^S_{vc\mathbf{k}}$ is the exciton amplitude. $vc\mathbf{k}$ indicates the exciton state is formed by the quasi-electron state $\mathbf{k}c$ and the quasi-hole state $\mathbf{k}v$; therefore the exciton wave function is a linear combination of quasi-electron and quasi-hole states:

$$\psi(\mathbf{r}_e, \mathbf{r}_h) = \sum_{\mathbf{k},v,c} A^S_{v,c,\mathbf{k}} \psi_{\mathbf{k},c}(\mathbf{r}_e) \psi^*_{\mathbf{k},v}(\mathbf{r}_h) \tag{1.27}$$

The electron-hole kernel K^{eh} contains contributions from the direct interaction K^d and the bare

exchange interaction K^x [37], where

$$\langle vc\mathbf{k}|\, K^d\, |v'c'\mathbf{k}'\rangle = -\int d\mathbf{r}d\mathbf{r}'\psi_c^*(\mathbf{r})\psi_{c'}(\mathbf{r})W(\mathbf{r},\mathbf{r}')\psi_{v'}^*(\mathbf{r}')\psi_v(\mathbf{r}') \tag{1.28}$$

and

$$\langle vc\mathbf{k}|\, K^x\, |v'c'\mathbf{k}'\rangle = \int d\mathbf{r}d\mathbf{r}'\psi_c^*(\mathbf{r})\psi_v(\mathbf{r})v(\mathbf{r},\mathbf{r}')\psi_{v'}^*(\mathbf{r}')\psi_{c'}(\mathbf{r}') \tag{1.29}$$

The absorption spectra is proportional to the imaginary part of the macroscopic dielectric function:

$$\varepsilon_2(\omega) \propto \sum_S |\mathbf{e}\cdot\langle 0|\,\mathbf{v}\,|S\rangle\,|^2\delta\left(\omega-\Omega_S\right) \tag{1.30}$$

where $\langle 0|\,\mathbf{v}\,|S\rangle = \sum_{vc\mathbf{k}} A^S_{vc\mathbf{k}}\langle v\mathbf{k}|\,\mathbf{v}\,|c\mathbf{k}\rangle$, $\mathbf{v}$ is the velocity operator and $\mathbf{e}$ is polarization of light.

1.3 Electron-phonon coupling

Electrons in condensed matter move in the potential field formed by ions. If a displacement of ions from the "perfect" sites exists in the lattice, a perturbation to the potential field occurs. The electron cloud moves with the ions, but at the same time experiences screening effects from other electrons. Electrons can also be scattered into other states. There are several approaches for the calculation of electron-phonon coupling. The rigid-ion approximation is one of the earliest methods, and assumes the potential field moves rigidly with ions. The main drawback of this method is that it does not include the electron screening effects and can lead to unphysical electron-phonon coupling strengths in the long-wavelength limit. To deal with this problem, ab-initio methods (DFT) have been used to recalculate the electron density self-consistently after the perturbation, and the development of density functional perturbation theory (DFPT) has greatly improved the efficiency of calculating perturbations at any phonon wavevector. The dielectric approach is another way to obtain the perturbed potential. The basic idea is to replace the external perturbation with a screened perturbation using the dielectric function. However, neither DFPT nor the dielectric method has fully solved the

problem due to their inherent Born-Oppenheimer approximation. Beyond the Born-Oppenheimer approximation, frequency-dependent screening and electron retardation effects should be taken into consideration. A comprehensive review on historic developments of the methods for electron-phonon coupling can be found in [38].

In this section, we first derive the electron-phonon coupling Hamiltonian, and then derive electron scattering rates from Fermi's golden rule.

1.3.1 Derivation of the electron-phonon coupling Hamiltonian

Corresponding to Eq. (1.1), the Kohn-Sham Hamiltonian is a function of distance between the electron at position $\mathbf{r}$ and the ion I at position $\mathbf{R}$. Assuming that the equilibrium position of the ion is $\mathbf{R}_I^0$, then the displacement from the equilibrium is $\mathbf{u}_I = \mathbf{R}_I - \mathbf{R}_I^0$.

$$\hat{H}_{KS} = \sum_{I,n,\mathbf{k},n',\mathbf{k}'} \int d\mathbf{r}\ \psi^{\dagger}_{n',\mathbf{k}'}(\mathbf{r}) v_{KS}(\mathbf{r}-\mathbf{R}_I)\psi_{n,\mathbf{k}}(\mathbf{r}) \tag{1.31}$$

Here, n is the band index, and $\mathbf{k}$ is the wavevector. By expanding the Hamiltonian to first order, we find:

$$\begin{aligned}\hat{H}_{KS} = &\sum_{I,n,\mathbf{k},n',\mathbf{k}'} \int d\mathbf{r}\ \psi^{\dagger}_{n',\mathbf{k}'}(\mathbf{r}) v_{KS}(\mathbf{r}-\mathbf{R}_I^0)\psi_{n,\mathbf{k}}(\mathbf{r}) \\ &+ \sum_{I,n,\mathbf{k},n',\mathbf{k}'} \int d\mathbf{r}\ \psi^{\dagger}_{n',\mathbf{k}'}(\mathbf{r})\ \mathbf{u}_I \cdot \frac{\partial v_{KS}(\mathbf{r}-\mathbf{R}_I)}{\partial \mathbf{R}_I}\psi_{n,\mathbf{k}}(\mathbf{r}) + \cdots\end{aligned} \tag{1.32}$$

where ψ is the Bloch wave $\psi_{n,k}(\mathbf{r}) = e^{i\mathbf{k}\cdot\mathbf{r}}\phi_{n,k}(\mathbf{r})$ and $\phi_{n,\mathbf{k}}(\mathbf{r})$ has the periodicity of lattice translations $\phi_{n,\mathbf{k}}(\mathbf{r}) = \phi_{n,\mathbf{k}}(\mathbf{r}+\mathbf{R})$, with $\mathbf{R}$ being a lattice vector:

$$\psi_{n,\mathbf{k}}(\mathbf{r}+\mathbf{R}_I^0) = e^{i\mathbf{k}\cdot\mathbf{R}_I^0}\psi_{n,\mathbf{k}}(\mathbf{r}) \tag{1.33}$$

The first-term in Eq. (1.32) is the interaction with the "perfect" lattice, and the second term is the electron-phonon coupling potential $\hat{H}_{e-ph}$. Using Eq. (1.33) in Eq. (1.32), we find:

$$\hat{H}_{e-ph} = \sum_{I,n,\mathbf{k},n',\mathbf{k}'} e^{i(\mathbf{k}-\mathbf{k}')\cdot\mathbf{R}_I^0}\ \mathbf{u}_I \cdot \underbrace{\int d(\mathbf{r}-\mathbf{R}_I^0)\ \psi^\dagger_{n',\mathbf{k}'}(\mathbf{r}-\mathbf{R}_I^0)\ \frac{\partial v_{KS}(\mathbf{r}-\mathbf{R}_I)}{\partial \mathbf{R}_I}\psi_{n,\mathbf{k}}(\mathbf{r}-\mathbf{R}_I^0)}_{\mathbf{S}_{n\mathbf{k},n'\mathbf{k}'}} \tag{1.34}$$

The electron-phonon coupling Hamiltonian is then expressed as:

$$\hat{H}_{e-ph} = \sum_{I,n,\mathbf{k},n',\mathbf{k}'} e^{i(\mathbf{k}-\mathbf{k}')\cdot\mathbf{R}_I^0}\ \mathbf{u}_I\ \cdot \mathbf{S}_{n\mathbf{k},n'\mathbf{k}'}\ a^\dagger_{n',\mathbf{k}'}\ a_{n,\mathbf{k}} \tag{1.35}$$

where $a^\dagger_{n',\mathbf{k}'}$ and $a_{n,\mathbf{k}}$ are electron creation and annihilation operators. Similarly, phonon displacement can be expressed as:

$$\mathbf{u}_I = \frac{1}{\sqrt{N}}\sum_{\mathbf{q},v}\sqrt{\frac{\hbar}{2M\omega_{\mathbf{q},v}}}\ e^{i\mathbf{q}\cdot\mathbf{R}_I^0}(b^\dagger_{-\mathbf{q},v}+b_{\mathbf{q},v})\ \mathbf{e}_{\mathbf{q},v} \tag{1.36}$$

where v denotes the index of phonon branches. Inserting Eq. (1.36) into Eq. (1.35) and considering the crystal momentrum conservation $\mathbf{k}' = \mathbf{k}+\mathbf{q}+\mathbf{G}$ with $\mathbf{G}$ being a reciprocal lattice vector, we obtain:

$$\hat{H}_{e-ph} = \frac{1}{\sqrt{N}}\sum_{n,n',v,\mathbf{k},\mathbf{q},\mathbf{G}} \underbrace{\sqrt{\frac{\hbar}{2M\omega_{\mathbf{q},v}}}\ \mathbf{e}_{\mathbf{q},v}\cdot\mathbf{S}_{n\mathbf{k},n'\mathbf{k}+\mathbf{q}+\mathbf{G}}}_{g_{n,n',v}(\mathbf{k},\mathbf{q},\mathbf{G})}\ a^\dagger_{n',\mathbf{k}+\mathbf{q}+\mathbf{G}}\ a_{n,\mathbf{k}}\ (b^\dagger_{-\mathbf{q},v}+b_{\mathbf{q},v}) \tag{1.37}$$

where $g_{n,n',v}(\mathbf{k},\mathbf{q},\mathbf{G})$ is the electron-phonon coupling matrix element. Since Normal processes often dominate over the Umklapp processes, we neglect Umklapp processes in the following derivations and enforce $\mathbf{G}$ to be $\mathbf{0}$. This assumption leads to:

$$\hat{H}_{e-ph} = \frac{1}{\sqrt{N}}\sum_{n,n',v,\mathbf{k},\mathbf{q}} \underbrace{\sqrt{\frac{\hbar}{2M\omega_{\mathbf{q},v}}}\ \mathbf{e}_{\mathbf{q},v}\cdot\mathbf{S}_{n\mathbf{k},n'\mathbf{k}+\mathbf{q}}}_{g_{n,n',v}(\mathbf{k},\mathbf{q})}\ a^\dagger_{n',\mathbf{k}+\mathbf{q}}\ a_{n,\mathbf{k}}\ (b^\dagger_{-\mathbf{q},v}+b_{\mathbf{q},v}) \tag{1.38}$$

1.3.2 Derivation of electron-phonon coupling scattering rates

We now derive electron scattering rates due to electron-phonon coupling using Fermi's golden rule. The transition probability from the initial state $|n,\mathbf{k}\rangle$ to the final state $|n',\mathbf{k}+\mathbf{q}\rangle$ is expressed as:

$$W^{\mathbf{q}v}_{n'\mathbf{k}+\mathbf{q},n\mathbf{k}} = \frac{2\pi}{\hbar}|M_{n'\mathbf{k}+\mathbf{q},n\mathbf{k}}|^2\delta(\varepsilon_{n'\mathbf{k}+\mathbf{q}}-\varepsilon_{n\mathbf{k}}) \tag{1.39}$$

where

$$\begin{aligned} M_{n'\mathbf{k}+\mathbf{q},n\mathbf{k}} &= \langle n',\mathbf{k}+\mathbf{q}|\,\hat{H}_{e-ph}\,|n,\mathbf{k}\rangle \\ &= \langle n_{\mathbf{q},v}+1;n',\mathbf{k}+\mathbf{q}|\,\hat{H}_{e-ph}\,|n,\mathbf{k};n_{\mathbf{q},v}\rangle \Longleftarrow \textbf{phonon emission} \\ \textbf{or } &= \langle n_{\mathbf{q},v}-1;n',\mathbf{k}+\mathbf{q}|\,\hat{H}_{e-ph}\,|n,\mathbf{k};n_{\mathbf{q},v}\rangle \Longleftarrow \textbf{phonon absorption} \end{aligned} \tag{1.40}$$

Here, $n_{\mathbf{q},v}$ is the Bose-Einstein distribution. Inserting Eq. (1.38) into Eq. (1.40), and applying the relation $b\,|n\rangle = \sqrt{n}\,|n-1\rangle$ and $b^\dagger\,|n\rangle = \sqrt{n+1}\,|n+1\rangle$, we find:

$$W^{\mathbf{q}v}_{n'\mathbf{k}+\mathbf{q},n\mathbf{k}} = \frac{2\pi}{\hbar N}|g_{n,n',v}(\mathbf{k},\mathbf{q})|^2\left[\underbrace{(n_{\mathbf{q},v}+1)\delta(\varepsilon_{n,\mathbf{k}}-\hbar\omega_{\mathbf{q},v}-\varepsilon_{n',\mathbf{k}+\mathbf{q}})}_{emission}+\underbrace{n_{\mathbf{q},v}\;\delta(\varepsilon_{n,\mathbf{k}}+\hbar\omega_{\mathbf{q},v}-\varepsilon_{n',\mathbf{k}+\mathbf{q}})}_{absorption}\right] \tag{1.41}$$

The electron scattering rate is the sum of the transition probabilities over all electron bands, phonon branches and phonon wavevectors:

$$\begin{aligned} \frac{1}{\tau_{n,\mathbf{k}}} &= \sum_{n',\mathbf{q},v} W^{\mathbf{q}v}_{n'\mathbf{k}+\mathbf{q},n\mathbf{k}} \\ &= \frac{2\pi}{\hbar N}\sum_{n',\mathbf{q},v}|g_{n,n',v}(\mathbf{k},\mathbf{q})|^2\left[\underbrace{(n_{\mathbf{q},v}+1)\delta(\varepsilon_{n,\mathbf{k}}-\hbar\omega_{\mathbf{q},v}-\varepsilon_{n',\mathbf{k}+\mathbf{q}})}_{emission}+\underbrace{n_{\mathbf{q},v}\;\delta(\varepsilon_{n,\mathbf{k}}+\hbar\omega_{\mathbf{q},v}-\varepsilon_{n',\mathbf{k}+\mathbf{q}})}_{absorption}\right] \end{aligned} \tag{1.42}$$

1.3.3 Photoconductivity

Upon photoexcitation, electron-hole pairs are generated and build up a large distribution of excited states. Within 10 to 150 fs, the electron subsystem rapidly thermalizes via carrier-carrier scattering

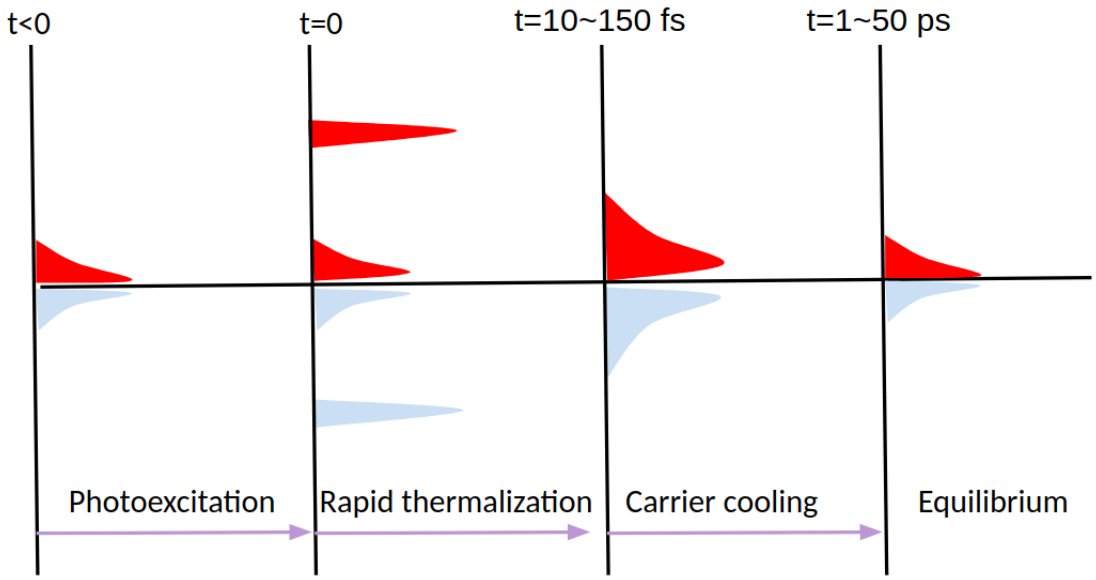

Figure 1.1: Hot carrier distribution

and can be described by an effective electron temperature T_e, which is higher than the phonon subsystem temperature T_{ph}. The system further relaxes through electron-phonon, phonon-phonon and defect scattering. This process takes tens of picoseconds, which is far longer compared with the relaxation among electrons. The corresponding carrier distributions at different time periods are shown in Fig. 1.1.

Photoconductivity describes the phenomenon in which electrical conductivity increases with photoexcitation. This can be explained as the excitation generates electron-hole pairs that both contribute to the conductivity $\Delta\sigma = \Delta n_e \mu_e + \Delta n_h \mu_h$. Here, we briefly derive the Drude model of conductivity.

The drift velocity equation is:

$$m\frac{d\mathbf{v}_d}{dt} + m\frac{\mathbf{v}_d}{\tau} = e\mathbf{E}e^{-i\omega t} \tag{1.43}$$

where ω is the frequency of the electric field. Assuming $\mathbf{v}_d = \mathbf{v}_0 e^{-i\omega t}$, we have:

$$m(-i\omega + \frac{1}{\tau})\mathbf{v}_0 = e\mathbf{E} \tag{1.44}$$

The current density is calculated by:

$$\mathbf{J} = ne\mathbf{v}_0 \tag{1.45}$$

and the conductivity is defined as:

$$\mathbf{J} = \sigma\mathbf{E} \tag{1.46}$$

Combing Eq. (1.44), (1.45) and (1.46), we find:

$$\sigma = \frac{ne^2}{m(-i\omega + \tau^{-1})} \tag{1.47}$$

1.4 Magnon-phonon interactions

1.4.1 Heisenberg model

The electronic wavefunction can be written as the product of two parts, the first part is spin-independent and contains only spatial information, and the second part contains information on spin polarization.

$$\Psi(\mathbf{r}_1, \sigma_1; \mathbf{r}_2, \sigma_2; \cdots) = \phi(\mathbf{r}_1, \mathbf{r}_2, \cdots)\chi(\sigma_1, \sigma_2, \cdots) \tag{1.48}$$

Because electrons are fermions, the wavefunction is antisymmetric. We consider a system of only two spin-1/2 particles. If $\phi(\mathbf{r}_1, \mathbf{r}_2, \cdots)$ is symmetric, then $\chi(\sigma_1, \sigma_2)$ must be antisymmetric; therefore the total spin S is 0. This is called a singlet state as there is only one alignment of two spins. Assuming the particles are non-interacting, the singlet wavefunction is written as:

$$\Psi_S(\mathbf{r}_1, \sigma_1; \mathbf{r}_2, \sigma_2) = \Big\{\phi_1(\mathbf{r}_1)\phi_2(\mathbf{r}_2) + \phi_1(\mathbf{r}_2)\phi_2(\mathbf{r}_1)\Big\}\chi_S \tag{1.49}$$

Similarly, If $\phi(\mathbf{r}_1, \mathbf{r}_2, \cdots)$ is antisymmetric, then $\chi(\sigma_1, \sigma_2)$ must be symmetric; therefore the total spin S is 1. This is called a triplet state as there are three combinations of alignments of two spins. The triplet wavefunction is written as:

$$\Psi_T(\mathbf{r}_1, \sigma_1; \mathbf{r}_2, \sigma_2) = \Big\{\phi_1(\mathbf{r}_1)\phi_2(\mathbf{r}_2) - \phi_1(\mathbf{r}_2)\phi_2(\mathbf{r}_1)\Big\}\chi_T \tag{1.50}$$

The energy is expressed as:

$$E_S = \int d\mathbf{r}_1 d\mathbf{r}_2 \Psi_S^\dagger \hat{H} \Psi_S \tag{1.51}$$

for the singlet state, and

$$E_T = \int d\mathbf{r}_1 d\mathbf{r}_2 \Psi_T^\dagger \hat{H} \Psi_T \tag{1.52}$$

for the triplet state. Using Eqn. (1.49) and (1.50), the singlet-triplet energy splitting is:

$$E_S - E_T = 2 \int d\mathbf{r}_1 d\mathbf{r}_2 \phi_1^\dagger(\mathbf{r}_1) \phi_2^\dagger(\mathbf{r}_2) \hat{H} \phi_1(\mathbf{r}_2) \phi_2(\mathbf{r}_1) \tag{1.53}$$

The associated Hamiltonian can be parametrized as:

$$\hat{H} = \frac{1}{4}(E_S + 3E_T) - J\vec{S}_1 \cdot \vec{S}_2 \tag{1.54}$$

where $\vec{S}_1 \cdot \vec{S}_2$ is $-\frac{3}{4}$ for the singlet and $\frac{1}{4}$ for the triplet, and $J = E_S - E_T$ describes the singlet-triplet energy splitting. Because the two states in Eq. (1.53) differ by exchanging two electrons, J is called exchange coupling constant. Because only the second term in Eq. (1.54) is spin-dependent, we define a spin Hamiltonian for a two-electron system as:

$$\hat{H}_{spin} = -J\vec{S}_1 \cdot \vec{S}_2 \tag{1.55}$$

if $J > 0$, the system favors the triplet state, and the spins are parallel with the total spin equal to 1; If $J < 0$, the system favors the singlet state, and the spins are antiparallel with the total spin equal to 0.

In many cases, the spin Hamiltonian for a many-electron system can be written as the sum over pairs of ions:

$$\hat{H}_{spin} = -\sum_{i,j} J_{ij} \vec{S}_i \cdot \vec{S}_j \tag{1.56}$$

This is called the Heisenberg model, and the spin Hamiltonian in Eq. (1.56) is called the Heisenberg Hamiltonian. Note the model is only applicable for systems of well-separated ions because interactions between two electrons on the same ion in Eq. (1.49) are neglected. A more detailed

explanation can be found in [39].

1.4.2 Spin-spiral method

Extracting the Heisenberg exchange constants is an essential step to study magnons and the interaction between magnons and other quantum particles. One of the most used methods is the so-called spin-spiral (frozen magnon) approach in which the energy difference between the ground state and the system with spin-spirals.

In real space, Eq. 1.56 becomes

$$H_{spin} = -\frac{1}{2}\sum_{n,m,\alpha,\beta} J(\boldsymbol{R}_{m\alpha}, \boldsymbol{R}_{n\beta})\boldsymbol{M}_{m\alpha}\cdot\boldsymbol{M}_{n\beta} \tag{1.57}$$

where $\boldsymbol{R}_{m\alpha(n\beta)} = \boldsymbol{R}_{m(n)} + \boldsymbol{\tau}_{\alpha(\beta)}$, $m(n)$ are the indexes of unit cells, $\boldsymbol{R}_{m(n)}$ are the lattice vectors, $\alpha(\beta)$ are basis vectors, and $\frac{1}{2}$ indicates that the spin energy is shared by the pair of atoms. By writing the magnetic moment vector $\boldsymbol{M}$ in terms of the cone angle θ and the phase angle ϕ

$$\boldsymbol{M}_{n\alpha} = M_\alpha \begin{pmatrix} sin\theta_\alpha\ cos(\boldsymbol{q}\cdot\boldsymbol{R}_{n\alpha} + \phi_\alpha) \\ sin\theta_\alpha\ sin(\boldsymbol{q}\cdot\boldsymbol{R}_{n\alpha} + \phi_\alpha) \\ cos\theta_\alpha \end{pmatrix} \tag{1.58}$$

where $\boldsymbol{q}$ is the spin spiral wave vector and applying a Fourier transform to the exchange constant J, Eq. 1.57 becomes

$$\begin{aligned} H_{spin}(\boldsymbol{q};\Theta;\Phi) = -\frac{1}{2}\sum_{\alpha\beta} M_\alpha M_\beta \Big\{ & sin\theta_\alpha\ sin\theta_\beta\ Re\Big[J_{\alpha\beta}(\boldsymbol{q})e^{i(\phi_\alpha-\phi_\beta)}\Big] \\ & + cos\theta_\alpha\ cos\theta_\beta\ J_{\alpha\beta}(\boldsymbol{0})\Big\} \end{aligned} \tag{1.59}$$

in the reciprocal space.

By defining $\tilde{J}_{\mu\nu}(\boldsymbol{q}) = J_{\mu\nu}(\boldsymbol{q}) - \delta_{\mu\nu}J_{\mu\nu}(\mathbf{0})$, it can be derived from Eq. 1.59 that

$$\tilde{J}_{\mu\mu}(\boldsymbol{q}) = -2\frac{H^{\mu}_{spin}(\boldsymbol{q}) - H^{\mu}_{spin}(\mathbf{0})}{M^2_{\mu} sin^2\theta} \tag{1.60}$$

in the case where only one atom's magnetic moment is tilted from the collinear ground state ($\theta_{\mu} \neq 0, \theta_{\lambda} = 0, \forall\lambda \neq \mu$). If there are more than two atoms in the unit cell and the magnetic moments of the two atoms of interest are tilted by θ_{μ} and θ_{nu} with the other atoms' magnetic moments being at the collinear states ($\theta_{\mu}, \theta_{\nu} \neq 0, \theta_{\lambda} = 0, \forall\lambda \neq \mu, \nu$), we find

$$Re[\tilde{J}_{\mu\nu}(\boldsymbol{q})] = \frac{H^{\mu\nu}_{spin}\left(\mathbf{0}, \frac{\pi}{2}\right) - H^{\mu\nu}_{spin}\left(\boldsymbol{q}, 0\right)}{M_{\mu}M_{\nu}\ sin^2\theta} - \frac{1}{2}\frac{M_{\mu}}{M_{\nu}}\tilde{J}_{\mu\mu} - \frac{1}{2}\frac{M_{\nu}}{M_{\mu}}\tilde{J}_{\nu\nu} \tag{1.61}$$

and

$$Im[\tilde{J}_{\mu\nu}(\boldsymbol{q})] = \frac{H^{\mu\nu}_{spin}(\boldsymbol{q}, \frac{\pi}{2}) - H^{\mu\nu}_{spin}(\boldsymbol{q}, 0)}{M_{\mu}M_{\nu}\ sin^2\theta} - Re[\tilde{J}_{\mu\nu}(\boldsymbol{q})] \tag{1.62}$$

where the first parameter in $H^{\mu\nu}_{spin}$ is the spin spiral's wave vector $\boldsymbol{q}$, and the second parameter in $H^{\mu\nu}_{spin}$ is the difference between the phase angles of the two tilted magnetic moments $\phi_{\mu} - \phi_{\nu}$. A back-Fourier transform gives the Heisenberg exchange constant in the real space

$$J(\boldsymbol{\tau}_{\mu}, \boldsymbol{\tau}_{\nu} - \boldsymbol{R}) = \frac{1}{V_{BZ}}\int_{V_{BZ}} \tilde{J}_{\mu\nu}(\boldsymbol{q}) e^{-i\boldsymbol{q}\cdot(\boldsymbol{\tau}_{\mu\nu} - \boldsymbol{R})} d^3q. \tag{1.63}$$

A detailed derivation of the spin-spiral method can be found in [40].

The spin-spiral method is used on the basis of static mean-field DFT methods in which the Kohn-Sham eigenvalue problem is solved. For each pair of magnetic atoms, the integral over the spin spiral wave vectors in the Brillouin zone needs to be calculated as shown in Eq. 1.63. Even though symmetry can be used to reduce the number of wave vectors $\boldsymbol{q}$ to be calculated, the amount of work is still enormous in a large system with many magnetic atoms. The size of the $\boldsymbol{q}$-grid depends on the distance between atoms; therefore a convergence test over the $\boldsymbol{q}$-grid is required. Because the magnitude of spin energy is small compared with the total ground state energy in the presence of a small magnetic perturbation, a dense $\boldsymbol{k}$-grid is needed to obtain accurate energy

differences between the ground state and the states with spin spirals. The computational cost for a large system including interfaces makes the spin-spiral method not practical. The method we adopt in this work for calculating the Heisenberg exchange constants is to use the formulation of Lichtenstein et al. [41]

$$J_{ij} = \frac{1}{4\pi} Im \int dE Tr(t_{i\uparrow}^{-1} - t_{i\downarrow}^{-1}) \tau_{\uparrow}^{ij} (t_{j\uparrow}^{-1} - t_{j\downarrow}^{-1}) \tau_{\downarrow}^{ji}. \tag{1.64}$$

where t is the single-site t-matrix and τ is the scattering path operator in the Korringa, Kohn and Rostoker (KKR) [42, 43] method incorporated into a Green's function formalism [44, 45, 44, 46, 47].

The KKR Green's function method calculates the Green's function and does not require solving the eigenvalue problem in the Kohn-Sham equation. Density of states, charge density, spin and orbital magnetic moments could be calculated directly from the Green's function. Electron density of states is the imaginary part of the integral of the Green's function over space:

$$n(E) = -\frac{1}{\pi} Im \int G(\mathbf{r}, \mathbf{r}'; E) d^3 r = -\frac{1}{\pi} Im Tr G(E). \tag{1.65}$$

Similarly, the charge density can be obtained by integrating the Green's function up to the Fermi level:

$$\rho(\mathbf{r}) = -\frac{1}{\pi} Im \int_{-\infty}^{E_F} G(\mathbf{r}, \mathbf{r}'; E) dE \tag{1.66}$$

The Dyson equation connects the Green's function of the unperturbed system to the perturbed system; therefore it can treat complex structures (e.g., surfaces, nano structures). The Green's function formalism also enables the study of spectroscopic properties and transport properties [48, 49, 50, 51, 52]. The KKR method incorporated with the coherent potential approximation (CPA) [53, 54, 55] can be used for disordered alloys.

The KKR Green's function method involves solving the single-site scattering problem and the multiple-scattering problem. Single-site scattering involves calculating the single-site t-matrix associated with one electron being scattered by a single potential and the multiple-scattering requires

that the incoming wave at one site is equal to the outgoing waves at all the other sites when the electron is scattered by multiple scattering potentials. In the following we introduce single-site scattering, multiple-scattering theory and the KKR Green's function method based on multiple-scattering theory.

1.4.3 Single-site scattering

The one-electron Schrödinger equation of a plane-wave in an external scattering potential V is

$$H_0 |\psi\rangle + V |\psi\rangle = E |\psi\rangle \tag{1.67}$$

where H_0 is the kinetic energy operator. Eq. 1.67 can be rearranged as

$$(E - H_0) |\psi\rangle = V |\psi\rangle \tag{1.68}$$

The homogeneous solution to Eq. 1.68 is

$$(E - H_0) |\phi\rangle = 0 \tag{1.69}$$

where ϕ represents the wave function of a free-electron without experiencing the external scattering potential. The general solution to Eq. 1.68 is the sum of a homogeneous solution and a particular solution

$$|\psi\rangle = |\phi\rangle + (E - H_0 + i\eta)^{-1} V |\psi\rangle = |\phi\rangle + G_0^+ V |\psi\rangle \tag{1.70}$$

where G_0^+ is the Green's function associated with an outgoing wave of a free-electron.

Eq. 1.70 is the Lippmann-Schwinger equation widely used in scattering theories. Rearranging Eq. 1.70 gives

$$(1 - G_0^+ V) |\psi\rangle = |\phi\rangle . \tag{1.71}$$

The term $(1-G_0^+)^{-1}$ can be expanded as

$$(1-G_0^+V)^{-1} = 1+G_0^+V+G_0^+VG_0^+V+\cdots = 1+G_0^+T \tag{1.72}$$

where T is the scattering matrix and defined as $T = V+VG_0^+V+VG_0^+VG_0^+V+\cdots$. Notice

$$T = V(1+G_0^+T). \tag{1.73}$$

Multiplying both sides of Eq. 1.71 by $(1-G_0^+V)^{-1}$ gives

$$|\psi\rangle = (1+G_0^+T)\,|\phi\rangle\,. \tag{1.74}$$

Eq. 1.74 connects the wave function of an electron in an external scattering potential to the wave function of a free electron.

The Green's function of an electron influenced by the external scattering potential is connected to the Green's function of a free electron via the Dyson equation:

$$G(E) = G_0^+(E)+G(E)VG_0^+ = G_0^+ + G_0^+T(E)G_0^+(E) \tag{1.75}$$

where G and G_0^+ are Green's functions with and without perturbation of the scattering potential V, respectively. Both G and G_0^+ are energy-dependent.

1.4.4 Multiple-scattering theory

So far we have assumed there is only one scattering potential V. In the presence of multiple scattering potentials that do not overlap in space, we can write

$$V = \sum_i v_i \tag{1.76}$$

where i is the index of the scattering site and v_i is the scattering potential at the scattering site i. By defining

$$T = \sum_i Q_i \tag{1.77}$$

and expanding T in terms of Q_i on the right side of Eq. 1.73, we have

$$T = \sum_i v_i (1 + G_0^+ \sum_j Q_j). \tag{1.78}$$

Rearranging Eq. 1.78 gives

$$T = \sum_i v_i G_0^+ Q_i + \sum_i v_i (1 + G_0^+ \sum_{j \neq i} Q_j). \tag{1.79}$$

By comparing Eq. 1.79 to Eq. 1.77, we have

$$Q_i = v_i G_0^+ Q_i + v_i (1 + G_0^+ \sum_{j \neq i} Q_j). \tag{1.80}$$

Rearranging Eq. 1.80 gives

$$(1 - v_i G_0^+) Q_i = v_i (1 + G_0^+ \sum_{j \neq i} Q_j). \tag{1.81}$$

Eq. 1.81 can be further reduced to

$$Q_i = (1 - v_i G_0^+)^{-1} v_i (1 + G_0^+ \sum_{j \neq i} Q_j) \tag{1.82}$$

We define

$$t^i = (1 - v_i G_0^+)^{-1} v_i \tag{1.83}$$

where t^i is the single-scattering t-matrix and describes the transition from an incoming wave to an outgoing wave in the presence of the scattering potential v_i at scattering site i, and Eq. 1.82

becomes

$$Q_i = t^i(1 + G_0^+ \sum_{j \neq i} Q_j) \tag{1.84}$$

t^i can be further expanded as

$$t^i = (1 + v_i G_0^+ + v_i G_0^+ v_i G_0^+ + \cdots)v_i = v_i(1 + G_0^+ t^i). \tag{1.85}$$

Combining Eq. 1.84 and Eq. 1.85 gives

$$T = \sum_i t^i + \sum_i t^i G_0^+ \sum_{j \neq i} t^j + \sum_i G_0^+ \sum_{j \neq i} t^j G_0^+ \sum_{k \neq j} t^k + \cdots \tag{1.86}$$

The first term in Eq. 1.86 represents the scattering from the site i to outside the cluster; the second term represents the scattering from site i to site j and then site j to outside the cluster; the third term represents the scattering from site i to site j, site j to site k and then site k to outside the cluster; and so on so forth.

Now we can rewrite Eq. 1.74 as

$$\begin{aligned} |\psi\rangle &= (1 + G_0^+ \sum_i Q_i)\,|\phi\rangle \\ &= |\phi\rangle + G_0^+ \sum_i Q_i\,|\phi\rangle \\ &= |\phi\rangle + G_0^+ \sum_i t_i\,|\phi_i^{in}\rangle \\ &= |\phi\rangle + \sum_i |\phi_i^{out}\rangle \end{aligned} \tag{1.87}$$

where $|\phi\rangle$ is the incident wave on the cluster with multiple scattering sites, t is the single-site t-matrix at site i, $|\phi_i^{in}\rangle$ is the incoming wave at site i, and $|\phi_i^{out}\rangle$ is the outgoing wave at site i. Eq. 1.87 is the Lippmann-Schwinger equation for a system with multiple scattering sites.

1.4.5 Korringa-Kohn-Rostoker Green's function method

The KKR representation of the Green's function method requires first solving the single-site scattering by calculating the single-site t-matrix which is later used in solving the multiple-scattering problem. The single-site scattering concerns the problem of the incident wave being scattered by one scattering potential as indicated by the Lippmann-Schwinger equation (Eq. 1.70).

The Green's function G_0^+ of a free-electron system (scattering potential $V = 0$) is expressed as

$$G_0^+(\mathbf{r},\mathbf{r}';E) = -\frac{1}{4\pi}\frac{e^{ik|\mathbf{r}-\mathbf{r}'|}}{|\mathbf{r}-\mathbf{r}'|} \tag{1.88}$$

in Cartesian coordinates and as

$$G_0^+(\mathbf{r},\mathbf{r}';E) = -i\sqrt{E}\sum_L Y_L j_l(\sqrt{E}r_<)h_l(\sqrt{E}r_>)Y_L(\mathbf{r}') \tag{1.89}$$

in the angular momentum representation where Y_L represents spherical harmonics, j_l are the Bessel functions and h_l are spherical Hankel functions.

The radial wave function (the solution to the radial Schrödinger equation) of an electron scattered by a single potential V in the angular momentum representation is

$$R_l(r;E) = j_l(\sqrt{E}r) + \int_0^S g_l(r,r';E)V(r')R_l(r';E)r'^2dr' \tag{1.90}$$

and the single-site t-matrix in the angular momentum representation is

$$t_l(E) = \int_0^S j_l(\sqrt{E}r)V(r)R_l(r;E)r^2dr. \tag{1.91}$$

The single-site Green's function under the single scattering potential perturbation is obtained via the Dyson equation (Eq. 1.75)

$$G_s(\mathbf{r},\mathbf{r}';E) = -i\sqrt{E}\sum_L R_l(r_<;E)H_l(r_>;E)Y_L(\mathbf{r})Y_L(\mathbf{r}') \tag{1.92}$$

where R_L and H_L are the regular and irregular solution to the radial Schrödinger equation, respectively.

In a periodic lattice, we assume the scattering potential at each atomic site is spherically symmetric within a muffin-tin radius r_{MT} and is a constant outside the muffin-tin radius; there is no overlapping of potentials in the interstitial region:

$$V(\mathbf{r}) = \begin{cases} V(r) & r \leq r_{MT} \\ 0 & r \geq r_{MT} \end{cases} \tag{1.93}$$

The multiple-scattering Green's function of a periodic lattice becomes

$$G(\mathbf{r}+\mathbf{R}^n, \mathbf{r}'+\mathbf{R}^{n'}; E) = -i\sqrt{E}\sum_L R_L^n(\mathbf{r}_<; E) H_L^n(\mathbf{r}_>; E)\delta_{n,n'} + \sum_{L,L'} R_L^n(\mathbf{r}; E) G_{LL'}^{nn'}(E) R_{L'}^{n'}(\mathbf{r}'; E) \tag{1.94}$$

where $\mathbf{R}$ represents lattice sites, n is the index of atomic cells and $G_{LL'}^{nn'}$ is the structural Green's functions is calculated using structure constants and the single-scattering t-matrix via the Dyson equation

$$G_{LL'}^{nn'}(E) = g_{LL'}^{nn'}(E) + \sum_{n'',L''} g_{LL''}^{nn''}(E) t_{l''}^{nn''}(E) G_{L''L'}^{n''n'}. \tag{1.95}$$

Eq. 1.95 can be expanded as

$$G_{LL'}^{nn'} = g_{LL'}^{nn'} + \sum_{n'',L''} g_{LL''}^{nn''} t_{l''}^{n''} g_{L''L'}^{n''n'} + \sum_{n'',L''}\sum_{n''',L'''} g_{LL''}^{nn''} t_{l''}^{n''} g_{L''L'''}^{n''n'''} t_{l'''}^{n'''} g_{L'''L'}^{n'''n'} + \cdots \tag{1.96}$$

where the first term on the right side represents the case that the incoming wave from n' goes directly to the outgoing wave at n, the second term represents the case that the incoming wave from n' is scattered once before it propagates to n and the third term represents the case that the incoming wave at n' is scattered twice. We can decompose the scattering matrix T and define a scattering path operator $\tau^{nn'}$ that describes the possible transitions from the incoming wave at n' to the outgoing wave at n

$$T(E) = \sum_{nn'} \tau^{nn'}(E) \tag{1.97}$$

where

$$\tau^{nn'}(E) = t^n \delta_{nn'} + t^n(E) \sum_{k \neq n} g^{nk} \tau^{kn'}(E). \tag{1.98}$$

By matrix inversion, Eq. 1.98 can be reduced to

$$\tau(E) = [t(E)^{-1} - g(E)]^{-1} \tag{1.99}$$

where $t(E)^{-1} - g(E)$ is the real-space KKR matrix $M(E)$. Eq. 1.99 indicates that the structure part g and the scattering part t are separated in KKR Green's function method. The algorithm of KKR Green's functions is summarized as follows:

1. Calculate the single-scattering free electron Green's function G_0^+.

2. Calculate wave functions R_l for each atomic cell with the single-scattering free electron Green's function via the Lippmann-Schwinger equation Eq. 1.90.

3. Calculate the single-site Green's function G_s via Eq. 1.92.

4. Calculate the single-scattering t-matrix via Eq. 1.91.

5. Calculate the structural Green's function $G_{LL'}^{nn'}$ via Eq. 1.95.

6. Calculate the multiple-scattering Green's function G via Eq. 1.94.

1.5 Experimental techniques

In this section, we introduce three experimental techniques widely used to study electron-electron, electron-phonon interactions, and carrier dynamics: angle-resolved photoemission spectroscopy (ARPES), electron energy loss spectroscopy (EELS) and the pump-probe experiment. We relate the experimentally measured quantities to first-principles calculations, and compare some of the simulation results with experiments later.

1.5.1 Angle-resolved photoemission spectroscopy (ARPES)

Angle-resolved photoemission spectroscopy (ARPES) provides a way of directly probing electron band structure and also helps to study electron-electron and electron-phonon interactions, which is reflected in the spectral broadening in ARPES intensity measurements. The schematic of an ARPES experiment is shown in Fig. 1.2. The sample is illuminated by monochromatic light. An electron absorbs the photon energy $h\nu$ and jumps from the initial state E_i to the final state E_f, leaving a hole behind. If the photon energy is large enough for electrons to overcome the work function ϕ, electrons can escape from the sample. These escaped electrons are collected, and their excessive kinetic energy E_{kin} and the polar(θ) and azimuthal(φ) emission angles are then analyzed. The band structure is obtained from the relationship between the parallel component of the momentum $k_{//}$ and the binding energy E_B. The binding energy is inferred by:

$$E_B = h\nu - E_{kin} - \phi \tag{1.100}$$

During the photoemission process, the momentum parallel to the surface is conserved while the momentum perpendicular to the surface is not. The momentum before photoemission is calculated by:

$$k_{//} = \frac{1}{\hbar}\sqrt{2m_e E_{kin}} sin\theta \tag{1.101}$$

We now introduce the widely-used three-step model to describe the photoemission process. The three steps are:

(i) Electrons absorb photon energies and electron-hole pairs are generated in the bulk material. Using Fermi's golden rule, the transition probability from the initial state to the final state is:

$$W_{fi} = \frac{2\pi}{\hbar} |\langle \Psi_f^N | - \frac{e}{mc}\mathbf{A}\cdot\mathbf{p}|\Psi_i^N\rangle|^2 \delta(E_f^N - E_i^N - h\nu) \tag{1.102}$$

Here, $\mathbf{p}$ is the electron momentum operator, $\mathbf{A}$ is associated with light polarization. In order to evaluate Eq. 1.102, we need to know Ψ_f^N and Ψ_i^N. Within the "sudden approximation", the photoexcitation and emission happen instantaneously so that the N-1 system is not relaxed, and the

photoelectron does not interact with the N-1 system; therefore the final state wave function can be written as:

$$\Psi_f^N = \phi_f^{\mathbf{k}} \Psi_f^{N-1} \tag{1.103}$$

The initial state wave function is expressed as:

$$\Psi_i^N = \phi_i^{\mathbf{k}} \Psi_i^{N-1} \tag{1.104}$$

Inserting Eq. (1.103) and (1.104) into (1.102), we obtain:

$$W_{fi} = \frac{2\pi}{\hbar} |\langle \phi_f^{\mathbf{k}} | - \frac{e}{mc} \mathbf{A} \cdot \mathbf{p} | \phi_i^{\mathbf{k}} \rangle|^2 \sum_m |\langle \Psi_m^{N-1} | \Psi_i^{N-1} \rangle|^2 \delta(E_{kin} + E_m^{N-1} - E_i^N - h\nu) \tag{1.105}$$

where m denotes excited N-1 state.

(ii) Electrons travel to the surface and experience scattering.

(iii) Photoelectrons escape to the vacuum, and those unscattered electrons are detected.

The ARPES intensity is expressed as:

$$I(\mathbf{k}, \omega) = I_0(\mathbf{k}, \nu, \mathbf{A}) f(\omega) A(\mathbf{k}, \omega) \tag{1.106}$$

where I_0 depends on the electron momentum $\mathbf{k}$, photon energy $h\nu$ and light polarization $\mathbf{A}$, $f(\omega)$ is the Fermi-Dirac distribution function, and $A(\mathbf{k}, \omega)$ is the single-particle spectral function which can be expressed in normal state in terms of electron self-energies as:

$$A(\mathbf{k}, \omega) = -\frac{2}{\pi} \frac{Im \sum(\mathbf{k}, \omega)}{(\omega - \varepsilon_{\mathbf{k}} - Re \sum(\mathbf{k}, \omega))^2 + (Im \sum(\mathbf{k}, \omega)^2} \tag{1.107}$$

Here $\varepsilon_{\mathbf{k}}$ is the bare band energy without electron-electron or electron-phonon interactions. The interactions with the lattice and other electrons are incorporated into the self-energy term $\sum(\mathbf{k}, \omega)$. The real part of self-energy is the renormalization of the bare band energy, and the imaginary part describes the electron quasi-particle lifetimes.

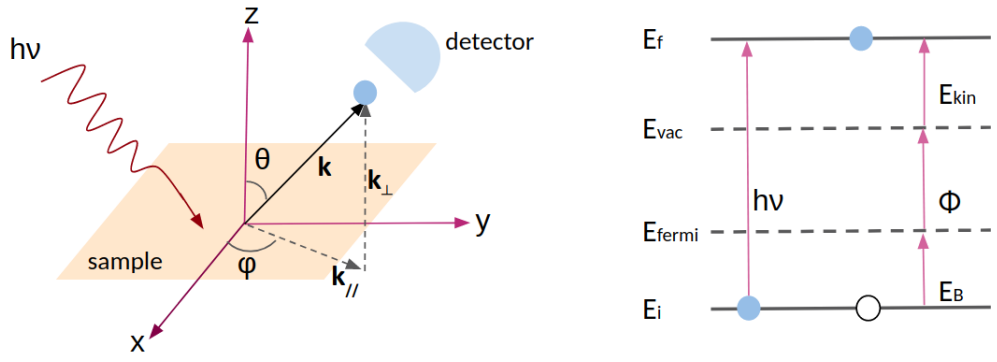

Figure 1.2: Schematic of an ARPES experiment

1.5.2 Electron energy loss spectroscopy (EELS)

Electron energy loss spectroscopy (EELS) is a powerful technique to probe plasmons. Fig. 1.3 shows a typical setup of EELS, which incorporates an energy loss spectrometer into either a transmission electron microscopy (TEM) or a scanning TEM (STEM). A beam of electrons accelerated by a high potential (60 kV to 300 kV) has a small wavelength and thus high spatial resolution (0.1 nm). This is one of the advantages of using electron beams over light beams, since light suffers from diffraction which results in a low spatial resolution. The intensity of the beam is controlled by the condenser lenses. The electrons impinging on the sample transfer energy to the sample electrons, and also induce collective oscillations (plasmons) in the sample. They then transmit through the sample and are focused by the objective lens to form an image. This image is further projected by the projection lens to the high angle annular dark field (HAADF) detector. The transmitted electrons are then dispersed by the magnetic prism. The E_0 peak represents the unscattered electrons while the $E_0 - \Delta E$ peak represents the inelastically scattered electrons.

The experimentally measured quantity is the double-differential cross section $\frac{d^2\sigma}{d\Omega d\omega}$, which is proportional to the number of scattered electrons into the solid angle $d\Omega$ with energy change $\hbar d\omega$. In this section, we derive the relationship between $\frac{d^2\sigma}{d\Omega d\omega}$ and the macroscopic dielectric function, which can be computed from first principles.

The differential cross section is expressed as the sum of the transition probability W_{fi} from the

initial state $|\Psi_i\rangle$ to the final state $|\Psi_f\rangle$:

$$d\sigma = \frac{m_e}{\hbar k_i} d\left(\sum_f W_{fi}\right) = \frac{m_e}{\hbar k_i}\frac{1}{(2\pi)^3} d\left(\int W_{fi} d\mathbf{k}_f\right) = \frac{m_e}{\hbar k_i}\frac{1}{(2\pi)^3} W_{fi} d\mathbf{k}_f \tag{1.108}$$

where m_e is the static electron mass, and k_i is the magnitude of the incident electron momentum. Using $d\omega = \frac{1}{\hbar} d\varepsilon = \frac{1}{\hbar} d\frac{\hbar^2(k_f^2 - k_i^2)}{2m_e} = \frac{\hbar k_f}{m_e} dk_f$, we find:

$$d\mathbf{k}_f = k_f^2 dk_f d\Omega = \frac{k_f m_e}{\hbar} d\omega d\Omega \tag{1.109}$$

From Fermi's golden rule, W_{fi} is calculated via:

$$W_{fi} = \frac{2\pi}{\hbar} |\langle \Psi_f | \hat{V} | \Psi_i \rangle|^2 \delta(\varepsilon_i - \varepsilon_f - \hbar\omega) \tag{1.110}$$

where $\hat{V}$ is the Coulomb interaction between the incident electron and the lattice,

$$\hat{V} = -\sum_I \frac{Ze^2}{|\mathbf{r} - \mathbf{R}_I|} + \sum_l \frac{e^2}{|\mathbf{r} - \mathbf{r}_l|} \tag{1.111}$$

and Ψ_i (Ψ_f) is the many-body wave function of the system before (after) the electron impact. We assume:

$$\begin{aligned} \Psi_i(\mathbf{r}, \{\mathbf{r}_l\}) &= e^{i\mathbf{k}_i \cdot \mathbf{r}} \Psi_i(\{\mathbf{r}_l\}) \\ \Psi_f(\mathbf{r}, \{\mathbf{r}_l\}) &= e^{i\mathbf{k}_f \cdot \mathbf{r}} \Psi_f(\{\mathbf{r}_l\}) \end{aligned} \tag{1.112}$$

where $\{\mathbf{r}_l\}$ is the set of lattice electron positions. Using Eq. (1.111) and (1.112), we have:

$$\begin{aligned} \langle \Psi_f | \hat{V} | \Psi_i \rangle &= \langle \Psi_f(\{\mathbf{r}_l\}) | e^{i(\mathbf{k}_i - \mathbf{k}_f)\cdot \mathbf{r}} \left[-\sum_I \frac{Ze^2}{|\mathbf{r} - \mathbf{R}_I|} + \sum_l \frac{e^2}{|\mathbf{r} - \mathbf{r}_l|} \right] | \Psi_i(\{\mathbf{r}_l\}) \rangle \\ &= \langle \Psi_f(\{\mathbf{r}_l\}) | \frac{4\pi e^2}{|\mathbf{k}_i - \mathbf{k}_f|^2} \sum_l e^{i(\mathbf{k}_i - \mathbf{k}_f)\cdot \mathbf{r}_l} | \Psi_i(\{\mathbf{r}_l\}) \rangle \end{aligned} \tag{1.113}$$

Inserting Eq. (1.109), (1.110) and (1.113) into (1.108), we obtain:

$$\frac{d\sigma}{d\omega d\Omega} \propto \left(\frac{4\pi e^2}{|\mathbf{q}|^2}\right)^2 \frac{k_f}{k_i} \sum_f |\langle \Psi_f | \sum_l e^{i\mathbf{q}\cdot\mathbf{r}_l} |\Psi_i\rangle|^2 \delta(\varepsilon_i - \varepsilon_f - \hbar\omega) \tag{1.114}$$

where $\mathbf{q} = \mathbf{k}_i - \mathbf{k}_f$ is the momentum change.

The density-density response function is expressed as:

$$\chi(\mathbf{q},\omega) = \sum_f |\langle \Psi_f | \sum_l e^{i\mathbf{q}\cdot\mathbf{r}_l} |\Psi_i\rangle|^2 \left(\frac{1}{\hbar\omega - (\varepsilon_f - \varepsilon_i) + i\eta} - \frac{1}{\hbar\omega + (\varepsilon_f - \varepsilon_i) + i\eta}\right) \tag{1.115}$$

Using Eq. (1.16), we find:

$$Im\ \varepsilon_{00}^{-1} \propto \frac{1}{|\mathbf{q}|^2} \sum_f |\langle \Psi_f | \sum_l e^{i\mathbf{q}\cdot\mathbf{r}_l} |\Psi_i\rangle|^2 \delta(\varepsilon_i - \varepsilon_f - \hbar\omega) \tag{1.116}$$

Comparing Eq. (1.114) with (1.116), we derive the relation:

$$\frac{d\sigma}{d\omega d\Omega} \propto Im\ \varepsilon_{00}^{-1} \tag{1.117}$$

Eq. (1.117) provides a way of directly comparing the experimentally measured scattered electron flux with the DFT calculations of the dielectric function.

1.5.3 Ultrafast pump-probe experiments

Pump-probe experiments with a femtosecond or terahertz laser are widely used to probe excited state carrier dynamics. The setup is shown in Fig. 1.4. A light beam is split by the beam splitter (BS) into two signals: pump pulse and probe pulse. The pump pulse is stronger than the probe pulse as indicated by the height of the peaks. The sample is excited by the pump pulse through the absorption of photons and generates electron-hole pairs. The delay path in the yellow box is used to generate a variable delay time Δt between two pulses. The two pulses combine at the sample and separate again due to frequency or polarization differences. The probe pulse is collected by the detector, and the transmission is measured. Photoexcitation builds up a carrier distribution at

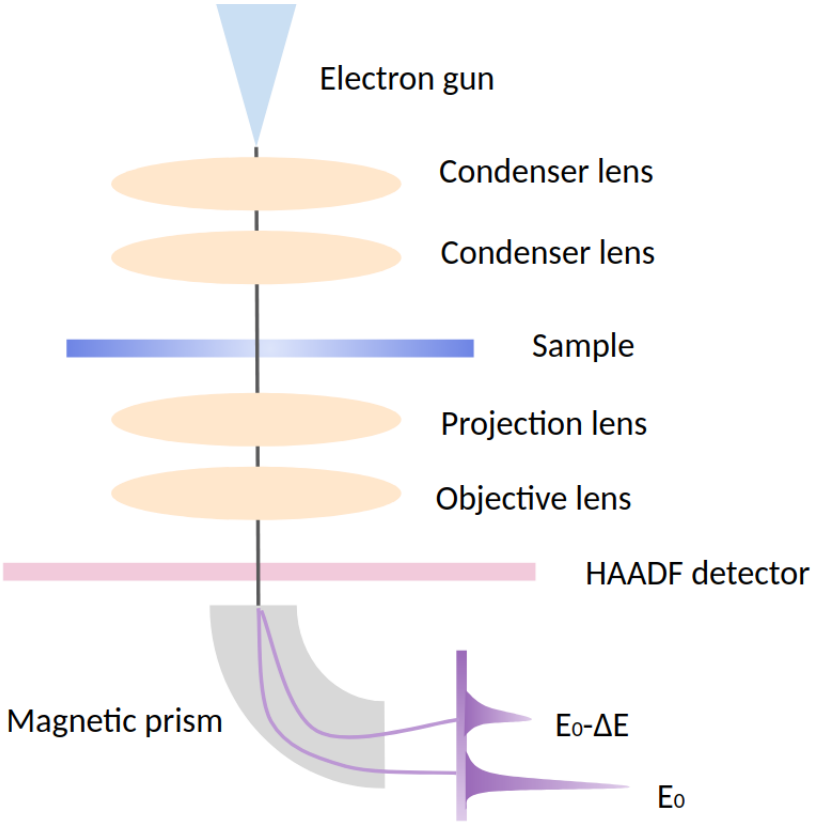

Figure 1.3: Schematic of an EELS experiment setup

excited states. This makes further absorption from the ground state difficult; therefore we expect an increase in the transmission T. Given enough time, the system will relax to the ground state via carrier-carrier scattering and electron-phonon scattering. By varying the delay time Δt, the time-dependent transmission and carrier dynamics are probed. The differential transmission is defined as the change in the transmitted probe beam intensity:

$$\frac{\Delta T(\Delta t)}{T_0} = \frac{I_{tr}(\Delta t) - I_0(t<0)}{I_0(t<0)} \tag{1.118}$$

where I_0 is the transmitted intensity before photoexcitation and can be expressed as:

$$I_0(t<0) = I_{in}e^{-\alpha_0 d} \tag{1.119}$$

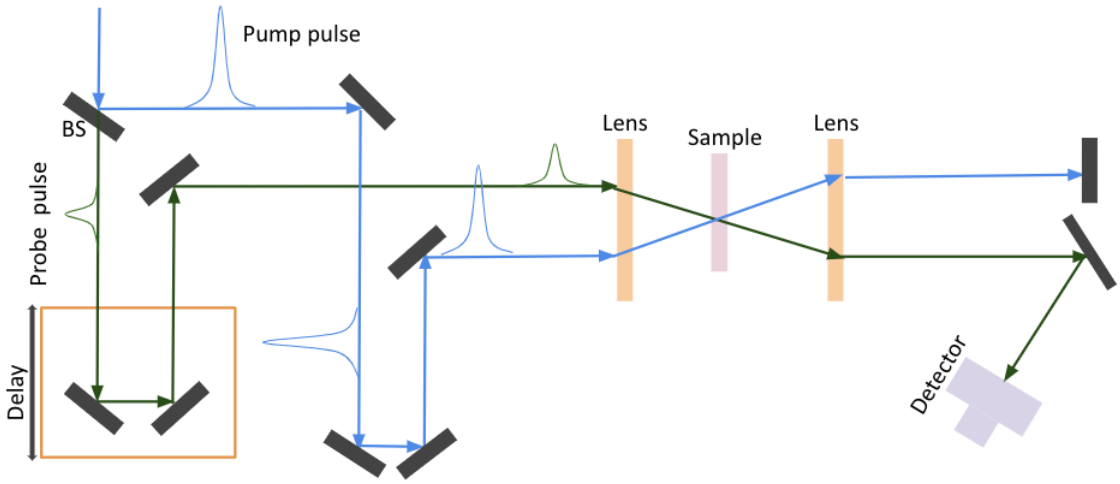

Figure 1.4: Pump-probe experiment setup

Here I_{in} is the incident probe beam intensity, α_0 is the absorption coefficient per unit length before the excitation, and d is the sample thickness. Assuming the absorption coefficient drops by $\Delta\alpha$ immediately after the excitation, and that the change of absorption decays in an exponential manner, I_{tr} can be expressed as:

$$I_{tr}(\Delta t) = I_{in} e^{-(\alpha_0 - \Delta\alpha e^{-\frac{\Delta t}{\tau}})d} \tag{1.120}$$

where τ is the relaxation time to the ground state. Inserting Eqn.1.119 and 1.120 into 1.118, we obtain:

$$\frac{T_0}{T} = \Delta\alpha e^{-\frac{\Delta t}{\tau}} d \tag{1.121}$$

1.6 Outline

Despite the extensive and intensive studies on electron-electron and electron-phonon interactions in bulk materials, their effects on surfaces and interfaces remain mysterious. Semiclassical methods such as molecular-dynamics and empirical relations have been used in the past, but first-principles calculations are rare due to the tremendous computational cost even with the development of supercomputers. Unlike electrons and phonons, the role of magnons in thermal transport has received attention only recently. Most of the related simulation work is on bulk materials such as iron, cobalt and yttrium iron garnet. Magnon-magnon and magnon-phonon interactions across the interface are

uncharted in spite of the intriguing phenomena they lead to.

The aim of this work is to predict multicarrier interactions from first principles and compare with experiments, and provide insights into their effects on electrical, optical and thermal properties in both bulk and interface structures.

This thesis is organized as follows. In Chapter 2, the coupling of electrons with different phonon modes in bilayer graphene is studied. The relaxation of energy from electrons to the lattice is calculated based on a two-temperature model. A Drude model is adopted to compute photoconductivity in bilayer graphene, and the effects of doping on photoconductivity are also discussed. In Chapter 3, we investigate the phonon-magnon interaction across the Co/Cu interface and its effect on the thermal boundary conductance by running equilibrium molecular dynamics using Heisenberg exchange constants extracted from first-principles calculations. Further, we compare the results obtained from the non-equilibrium Green's function method and the equilibrium molecular dynamics method incorporated with the fluctuation-dissipation theorem. In Chapter 4, we conduct first-principles calculations of optical response in single layer and bilayer armchair graphene nanoribbons. We use the GW method to predict the band structures of graphene nanoribbons and predict the optical absorption spectra considering the exciton effects by solving the Bethe-Salpeter equation. We compare the results for single layer armchair graphene nanoribbons from different families with different lengths. We also discuss the effects of nanoribbon layers and alignments on the optical absorption. In Chapter 5, we investigate the photo-thermal effect in methane decomposition by calculating the temperature rise after irradiation. We compute electronic transitions and absorption coefficient of several polycyclic aromatic hydrocarbons using TDDFT. Chapter 6 is a summary of this work.

CHAPTER 2

Photoconductivity Calculations of Bilayer Graphene from First Principles and Deformation-potential Approach

2.1 Introduction

Bernal stacked bilayer graphene exhibits a significantly different band structure compared to single-layer graphene. The conduction and valence bands split into two subbands with a separation of 0.4 eV between the two conduction subbands edges, and the linearity near the Dirac point is broken, accompanied by a reduction in the Fermi velocity. By breaking the inversion symmetry of the two layers, a band gap is induced and can be tuned through chemical doping [56] or gating [57], suggesting potential applications in transistors, optoelectronics and photonics [58, 59]. The performance of some of these devices depends strongly on the efficiency of carrier photoexcitation and subsequent hot carrier relaxation processes [60]. The purpose of this work is to develop a model for the coupling of electrons and phonons that can predict electron relaxation processes due to phonon interactions from first principles. A secondary objective is to compare these predictions to the commonly used deformation potential scattering approach.

Photoexcited carriers thermalize rapidly over a timescale of 100 to 200 fs and thus can be described by an effective electron temperature T_e. The hot carriers thereafter then scatter with phonons and transfer energy to the lattice. This process lasts for tens of picoseconds until the system returns to thermal equilibrium. Optical pump terahertz probe spectroscopy [61, 62] and angle-resolved photoelectron spectroscopy [63, 64] are the most often used methods for measuring electron-phonon coupling and carrier transport properties. The pump-probe method directly relates the measured optical transmission with and without photoexcitation to the photo-induced

conductivity change in the material under study. The transition from negative to positive differential transmission has been observed in graphene sheets by changing electrostatic gating and the Fermi level [65, 66]. The transition is explained as an interplay between Drude weight and scattering rates. Photoexcitation generates more electron-hole pairs in intrinsic graphene but only modifies the Fermi distribution in doped graphene and therefore increases absorption in the former case while inducing more scattering in the latter case. However, only phenomenological scattering rates have been used in prior studies, leaving details of the scattering processes unresolved [65, 66, 67].

Prior theoretical work on bilayer graphene's electrical conductivity has focused on short-range scattering from impurities using tight-binding Hamiltonians [68, 69]. Viljas et al. [70] calculated electron-phonon heat transport based on a two-temperature model, with scattering rates obtained from an empirical deformation potential approach. Park et al. [71] calculated electron-phonon coupling strengths from first principles; however, they focused on phonon lifetimes. Details of electron-phonon scattering mechanisms and their contributions to the electro-thermal transport properties of bilayer graphene are still not well understood.

In this work, we adopt a first-principles approach to obtain electron-phonon coupling constants and scattering rates from which effective acoustic and optical deformation potentials are extracted. A two-temperature heat transfer model is developed to predict the electron and lattice temperatures at different times, based on which we calculate photoconductivity using a Drude model. We explain the trends for real and imaginary parts of photoconductivity by analyzing the effects of doping levels and electron-phonon scattering, and further compare photoconductivity from DFT and the deformation-potential approach with previous experimental data.

2.2 Electron phonon interactions, deformation- potential and heat transfer

The development of density functional perturbation theory(DFPT) [72] has made first-principles calculations of electron-phonon coupling feasible in recent years. The temperature-independent electron-phonon coupling matrix g describes the coupling strength of the transition from an initial

electron state $|m,\mathbf{k}\rangle$ to a final state $|n,\mathbf{k}+\mathbf{q}\rangle$, and is calculated as [73]:

$$g_{mn\upsilon}(\mathbf{k},\mathbf{q}) = \sqrt{\frac{\hbar}{2M\omega_{\mathbf{q},\upsilon}}}\,\langle n,\mathbf{k}+\mathbf{q}|\,\Delta V_{\mathbf{q},\upsilon}\,|m,\mathbf{k}\rangle \tag{2.1}$$

Here, $|m,\mathbf{k}\rangle$ and $|n,\mathbf{k}+\mathbf{q}\rangle$ are wavefunctions for the initial and final Bloch states, $\Delta V_{\mathbf{q},\upsilon}$ is the self-consistent potential change experienced by electrons due to interaction with a phonon of wavevector $\mathbf{q}$ in branch υ, M is the mass of carbon atoms, and $\omega_{\mathbf{q},\upsilon}$ is the phonon frequency.

After obtaining the electron-phonon coupling matrix, electron scattering rates are calculated based on Fermi's golden rule and the relaxation time approximation [74]:

$$\begin{aligned}\tau_{m\mathbf{k}}^{-1}(T_e,T_{ph}) = {} & \frac{2\pi}{\hbar}\sum_{n,\mathbf{q},\upsilon}|g_{mn\upsilon}|^2 \\ & \{(f_{n,\mathbf{k}+\mathbf{q}}+n_{\mathbf{q},\upsilon})\delta(\varepsilon_{m,\mathbf{k}}+\hbar\omega_{\mathbf{q},\upsilon}-\varepsilon_{n,\mathbf{k}+\mathbf{q}}) \\ & +(1+n_{\mathbf{q},\upsilon}-f_{n,\mathbf{k}+\mathbf{q}})\delta(\varepsilon_{m,\mathbf{k}}-\hbar\omega_{\mathbf{q},\upsilon}-\varepsilon_{n,\mathbf{k}+\mathbf{q}})\}\end{aligned} \tag{2.2}$$

In Eq. 2.2, the first and second terms on the right side denote phonon absorption and emission. f is the Fermi-Dirac distribution at the electron temperature T_e, and n is the Bose-Einstein distribution at the phonon temperature T_{ph}. The summation extends over all electronic bands with a final state momentum $\mathbf{k}+\mathbf{q}$, phonon wavevectors and phonon branches.

Similarly, the heat transfer rate per unit area from electrons to the lattice is computed as [75, 76]:

$$\begin{aligned}Q_{e-ph} = {} & \frac{4\pi}{\hbar A}\sum_{\mathbf{k},\mathbf{q},m,n,\upsilon}\hbar\omega_{\mathbf{q},\upsilon}|g_{m,n,\upsilon}(\mathbf{k},\mathbf{q})|^2 \\ & \{f_{n,\mathbf{k}+\mathbf{q}}(1-f_{m,\mathbf{k}})(n_{\mathbf{q},\upsilon}+1)-(1-f_{n,\mathbf{k}+\mathbf{q}})f_{m,\mathbf{k}}n_{\mathbf{q},\upsilon}\} \\ & \delta(\varepsilon_{m,\mathbf{k}}+\hbar\omega_{\mathbf{q},\upsilon}-\varepsilon_{n,\mathbf{k}+\mathbf{q}})\end{aligned} \tag{2.3}$$

Here, A is the unit cell surface area. The dynamic temperature evolution is governed by energy

conservation as:

$$\begin{cases} C_e(T_e)\frac{dT_e}{dt} = -Q_{e-ph} \\ C_{ph}(T_{ph})\frac{dT_{ph}}{dt} = Q_{e-ph} \end{cases} \tag{2.4}$$

where C_e and C_{ph} are electron and phonon specific heats, respectively, and diffusive heat conduction has been neglected.

Even though first-principles calculations can be applied to any system in theory, the computations are extremely time-consuming. While Wannier function interpolation reduces computational cost greatly, the disentanglement procedure for complex material systems is quite involved, especially for interfaces consisting of dissimilar materials and having strong interactions.

For electron-phonon coupling calculations, the deformation-potential approach provides an alternative. Assuming that the perturbation of the potential felt by electrons is proportional to the change in unit cell volume, the deformation-potential approach is semiclassical and often obtained by fitting experimental mobility values. Here, we briefly discuss the derivation of the deformation potential for acoustic phonons. The development highlights the connection between the deformation potential and scattering rates, thus providing an explanation of how to extract the widely used deformation potential from our first-principles calculations.

The potential perturbation $\Delta V(\mathbf{r})$ is related to the relative volume change $\Delta(\mathbf{r})$ by [77]:

$$\Delta V(\mathbf{r}) = E_1 \Delta(\mathbf{r}) \tag{2.5}$$

where E_1 is the deformation potential, and $\mathbf{r}$ denotes lattice sites. $\Delta(\mathbf{r})$ is calculated in the long wavelength limit as:

$$\Delta(\mathbf{r}) = \frac{\partial \mathbf{u}(\mathbf{r})}{\partial \mathbf{r}} \tag{2.6}$$

Here, $\mathbf{u}(\mathbf{r})$ is the phonon displacement:

$$\mathbf{u}(\mathbf{r}) = \sum_{\mathbf{q}} \mathbf{e}_{\mathbf{q}} (A_{\mathbf{q}} e^{i\mathbf{q}\cdot\mathbf{r}} + A^*_{\mathbf{q}} e^{-i\mathbf{q}\cdot\mathbf{r}}) \tag{2.7}$$

where $\mathbf{e_q}$ is the normalized phonon eigenvector, and $2|A_\mathbf{q}|$ is the oscillation amplitude. Considering equipartition in which all phonons are excited and $\hbar\omega_\mathbf{q} \ll k_B T_L$, we can simplify the amplitude as $|A_\mathbf{q}^2| = \dfrac{k_B T}{2\rho A \omega_\mathbf{q}^2}$ (ρ is the mass density) by connecting the classical wave energy to the quantum harmonic oscillators' energy [78]. Combining Eqs. 2.5, 2.6 and 2.7, we find:

$$|\Delta V|^2 = \frac{{E_1}^2 k_B T_L}{2\rho A v_\mathbf{q}^2} \tag{2.8}$$

where $v_\mathbf{q}$ is the acoustic phonon group velocity. The transition probability $W_\mathbf{kk'}$, from state $|\mathbf{k}\rangle$ to state $|\mathbf{k}'\rangle$ is calculated as:

$$W_{\mathbf{k},\mathbf{k}'} = \frac{2\pi}{\hbar}|\Delta V|^2 \delta(\varepsilon_\mathbf{k} \pm \hbar\omega_\mathbf{q} - \varepsilon_{\mathbf{k}'})\delta(\mathbf{k} \pm \mathbf{q} - \mathbf{k}') \tag{2.9}$$

The momentum relaxation rate then becomes:

$$\tau_{ADP}^{-1}(\varepsilon_\mathbf{k}) = \sum_{\mathbf{k}'}(1 - \cos\theta(\mathbf{k},\mathbf{k}'))W_{\mathbf{k},\mathbf{k}'}\frac{1 - f(\varepsilon_{\mathbf{k}'})}{1 - f(\varepsilon_\mathbf{k})} \tag{2.10}$$

where $\cos\theta$ is the angle between $\mathbf{k}$ and $\mathbf{k}'$. We assume that acoustic deformation potential scattering is elastic and therefore use the momentum relaxation rate to approximate the scattering rate. The subscript in $\tau_{ADP}^{-1}(\varepsilon_\mathbf{k})$ indicates that the scattering rate is derived based on the acoustic deformation potential.

Inserting Eqs. 2.8 and 2.9 into Eq. 2.10 and considering valley and spin degeneracy, we obtain the scattering rate under the high-temperature and elastic-acoustic deformation approximations [79]:

$$\tau_{ADP}^{-1}(\varepsilon_\mathbf{k}) = \frac{1}{4\hbar^3}\frac{\varepsilon_\mathbf{k}}{V_F^2}\frac{{E_1}^2}{\rho v_\mathbf{q}^2} k_B T_L \tag{2.11}$$

where V_F is the Fermi velocity. We assume an isotropic Fermi velocity $V_F = 6 \times 10^5$ m/s in our calculations.

The average scattering rate is expressed as [79]:

$$\langle \tau_{ADP}^{-1} \rangle = \frac{\int d\varepsilon D(\varepsilon) \frac{1}{\tau(\varepsilon)} (-\frac{\partial f}{\partial \varepsilon})}{\int d\varepsilon D(\varepsilon) (-\frac{\partial f}{\partial \varepsilon})} \tag{2.12}$$

where $D(\varepsilon)$ is the density of states expressed as $\frac{2\varepsilon}{\pi\hbar^2 V_F^2}$. Eq. 2.12 can be further reduced using Eq. 2.10 as:

$$\langle \tau_{ADP}^{-1} \rangle = \frac{E_1^2}{4\rho v_{\mathbf{q}}^2} \frac{k_B T_L}{\hbar^3 V_F^2} \frac{\int d\varepsilon \varepsilon^2 (-\frac{\partial f}{\partial \varepsilon})}{\int d\varepsilon \varepsilon (-\frac{\partial f}{\partial \varepsilon})} \tag{2.13}$$

By equating the average scattering rates from DFT and the deformation-potential framework, effective deformation potentials can be extracted.

The optical deformation potential can be derived similarly with its scattering rate expressed as:

$$\tau_{ODP}^{-1}(\varepsilon_{\mathbf{k}}) = \frac{{D_o}^2}{4\rho\, \omega_o \hbar^2 {V_F}^2} [(\varepsilon_{\mathbf{k}} - \hbar\omega_o)(n_q + 1) + (\varepsilon_{\mathbf{k}} + \hbar\omega_o) n_q] \tag{2.14}$$

where $\hbar\omega_o$ is the optical phonon frequency and D_o is the optical deformation potential. The first term in the square bracket denotes the phonon emission, and only electrons with energies greater than $\hbar\omega_o$ are involved.

2.3 Photoconductivity and Drude Model

In pump-probe experiments, the variation of light transmission at a given frequency $\Delta T(\omega)$ is directly related to the photoconductivity $\Delta\sigma(\omega)$ via $\Delta\sigma(\omega) = -\frac{n_s + 1}{Z_0} \Delta T(\omega)/T(\omega)$, where $T(\omega)$ is the transmission without photoexcitation, ΔT is the difference in transmission with and without photoexcitation, n_s is the substrate's index of refraction, and Z_0 is the impedance of free space.

We use the Drude model for calculating photoconductivity. This model has proven to work well for bulk materials. Here, we consider bilayer graphene without defects throughout this work; therefore the Drude model is a reasonable choice. According to this model, conductivity is expressed as:

$$\sigma(\omega) = \frac{ne^2}{m^*} \frac{1}{\tau^{-1} - i\omega} = ne\mu \frac{\tau^{-1}}{\tau^{-1} - i\omega} \tag{2.15}$$

Here, n is the carrier density, e is the elementary charge, m^* is the effective mass, and τ is the

scattering rate. We compare our simulations to experiments in which bilayer graphene with low defects was placed above the SiO_2 substrate. Our current photoconductivity calculations do not consider surface optical phonon scattering as its contribution to the overall scattering rate is significantly smaller than intrinsic phonon scattering due to strong screening effects [62]. These terms are related to electron mobility via $\mu = \frac{e\tau}{m^*}$, and μ can be calculated from:

$$\mu = \frac{eV_F^2}{2n}\int_0^\infty D(\varepsilon)(-\frac{\partial f}{\partial \varepsilon})\tau(\varepsilon)d\varepsilon \tag{2.16}$$

where $D(\varepsilon)$ is the density of states. Inserting Eq. 2.16 into Eq. 2.15 gives:

$$\sigma(\omega) = \frac{e^2V_F^2}{2}\int_0^\infty D(\varepsilon)(-\frac{\partial f}{\partial \varepsilon})\frac{1}{\tau^{-1}-i\omega}d\varepsilon \tag{2.17}$$

Since photoexcitation is fast for electrons to establish a hot-carrier distribution, we assume an effective electrononic temperature T_e higher than the lattice temperature T_{ph} for the pump-on case and equal to the lattce temperature T_{ph} for the pump-off case. Photoconductivity is therefore the difference between the pump-on and pump-off conductivities $\Delta\sigma(\omega) = \sigma(T_e \neq T_{ph}, \omega) - \sigma(T_e = T_{ph}, \omega)$. By converting the integral over energy space to a summation over the k space, we find:

$$\begin{aligned}\frac{\Delta\sigma(\omega)}{G_0} = \frac{hV_F^2}{4N_kA}\Bigg\{&\sum_{\mathbf{k}}\frac{-\frac{\partial f(\mathbf{k},T_e\neq T_{ph})}{\partial\varepsilon(\mathbf{k})}}{\tau^{-1}(\mathbf{k},T_e\neq T_{ph},T_{ph})-i\omega}\\ &-\sum_{\mathbf{k}}\frac{-\frac{\partial f(\mathbf{k},T_e=T_{ph})}{\partial\varepsilon(\mathbf{k})}}{\tau^{-1}(\mathbf{k},T_e=T_{ph},T_{ph})-i\omega}\Bigg\}\end{aligned} \tag{2.18}$$

where $G_0 = \frac{2e^2}{h}$ is the conductance quantum.

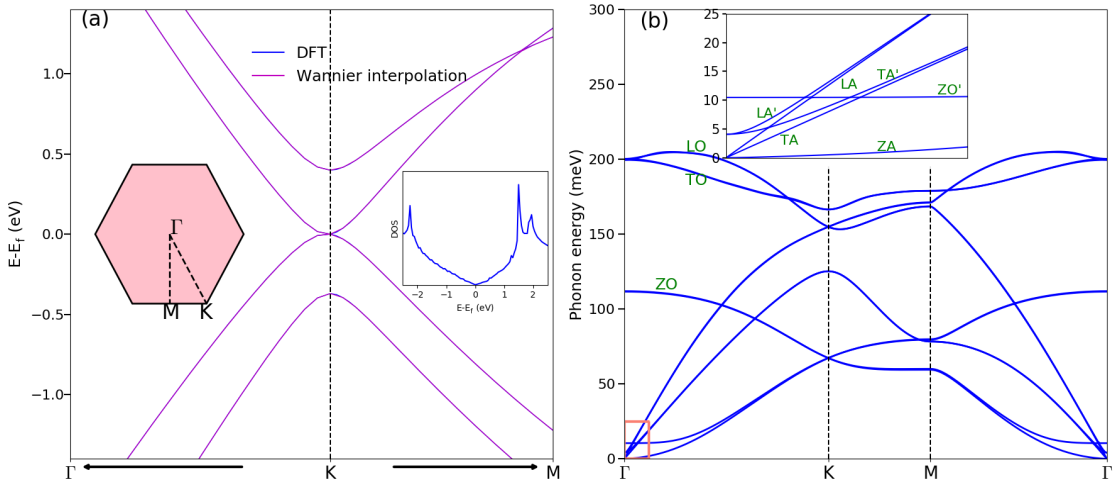

Figure 2.1: Electron band structure and phonon dispersion of bilayer graphene. (a) Bilayer graphene electron band structure. (b) Bilayer graphene phonon dispersion. The inset of (b) shows a magnified view of the box at the bottom left corner. Two low energy branches which are absent from single-layer graphene, LA′ and TA′, are lifted and separated from the LA and TA modes near the Γ point.

2.4 Results and discussion

In Bernal stacked bilayer graphene, half the atoms in the upper layer sit directly above the atoms in the lower layer while the other half lie at the centers of hexagons in the lower layer. The electronic structure was computed with the Quantum-Espresso package [80] using a norm-conserving pseudopotential in the local density approximation. A cutoff energy of 140 Ry and a Monkhorst-Pack $24 \times 24 \times 1$ k-space grid were chosen in the self-consistent calculations. The predicted interlayer distance is 3.3 Å. Phonon dispersion calculations were performed with DFPT and a $12 \times 12 \times 1$ q-space grid. Due to the high computational cost of calculating energies and coupling matrix elements, we use an interpolation scheme based on maximally localized Wannier functions on a dense $1000 \times 1000 \times 1$ k-mesh and q-mesh with the EPW package [81]. Our calculations for electronic band structure and phonon dispersion of bilayer graphene are shown in Fig. 2.1. Fig. 2.1(a) demonstrates that the Wannier-interpolated band structure completely overlaps the DFT calculated band structure within 1 eV of the Fermi level.

In single-layer graphene, the electron-phonon coupling matrix elements for TO and LO modes are significantly greater than those of acoustic modes in the low electron energy range, causing

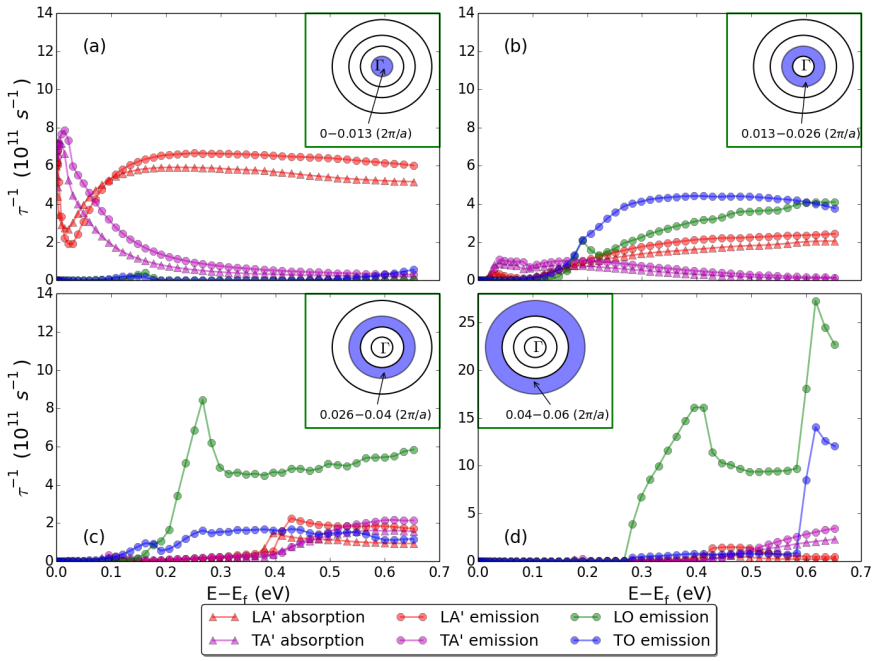

Figure 2.2: Intrinsic bilayer graphene electron scattering rates near the phonon Γ point at $T_e =$ 300 K and T_{ph} = 300 K. (a) Phonon wavevectors $0-0.013\ 2\pi/a$. LA$'$ and TA$'$ modes dominate for electron energies less than 200 meV. (b) Phonon wavectors $0.013-0.026\ 2\pi/a$. (c) Phonon wavevectors $0.026-0.04\ 2\pi/a$. (d) Phonon wavevectors $0.04-0.06\ 2\pi/a$. Optical modes only participate in phonon emission processes.

an order of magnitude larger scattering rates [76]. However, there are two major differences in the case of bilayer graphene. The first is that the electron-phonon coupling matrix elements are significantly smaller than single layer graphene, possibly due to the splitting of the two conduction bands and valence bands (see Fig. 2.1 (a)). The second is the emergence of LA$'$ and TA$'$ modes, as indicated by the inset of Fig. 2.1 (b).

Because of the constraints of energy and momentum conservation, electrons mainly interact with Γ-point and K-point phonons. To differentiate between different phonon branches and to understand how phonons of different wavevectors couple with electrons, we chose a small region of radius $0.06\times 2\pi/a$ (a is the lattice constant) near the phonon Γ and K points in reciprocal space and split it into four rings. The following calculations of scattering rates for a specific electronic state in the phase space are obtained by summing over all the phonon wavevectors within the corresponding rings on a dense 1000x1000x1 q-mesh. To highlight the effects of different phonon

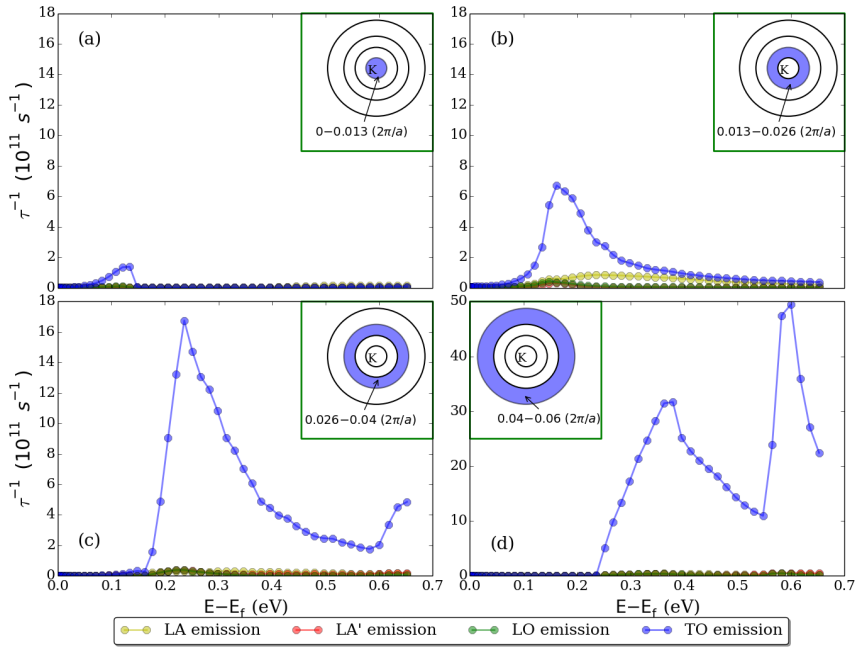

Figure 2.3: Intrinsic bilayer graphene electron scattering rates at the phonon K point at T_e = 300 K and T_{ph} = 300 K. (a) Phonon wavevectors $0-0.013\ 2\pi/a$ from the phonon K point. (b) Phonon wavectors $0.013-0.026\ 2\pi/a$ from the phonon K point. (c) Phonon wavevectors $0.026-0.04\ 2\pi/a$ from the phonon K point. (d) Phonon wavevectors $0.04-0.06\ 2\pi/a$ from the phonon K point. Acoustic phonons rarely participate in scattering events at the phonon K point. Optical modes, especially the TO mode, dominate over all energy ranges.

modes, the choices of the ring radii are based on the intersections of phonon branches near the phonon Γ point and K point as indicated by Fig. 2.1 (b), assuming isotropic dispersion. The shaded blue regions in the insets of Figs. 2.2, 2.3, 2.4, and 2.5 indicate the corresponding range of phonon wavevectors. The scattering rates were calculated for intrinsic bilayer graphene from first principles according to Eq. 2.2. The subscript $m\mathbf{k}$ is omitted because the scattering rates are plotted for electrons in the lower conduction band along the Dirac K - Γ path.

Fig. 2.2 shows that in the low electron energy range ($<$ 200 meV) near the phonon Γ point, LA$'$ and TA$'$ modes are dominant and confined to small phonon wavevectors ($< 0.026 \times 2\pi/a$). Unlike single-layer graphene, bilayer graphene scattering rates are not linearly proportional to the energies from the Dirac **K** point because LA$'$ and TA$'$ modes do not exhibit a linear dispersion near the phonon Γ point(see Fig. 2.1 (b)).

In Fig. 2.2 (a), the absorption process is slightly stronger than the emission process at $E - E_f <$

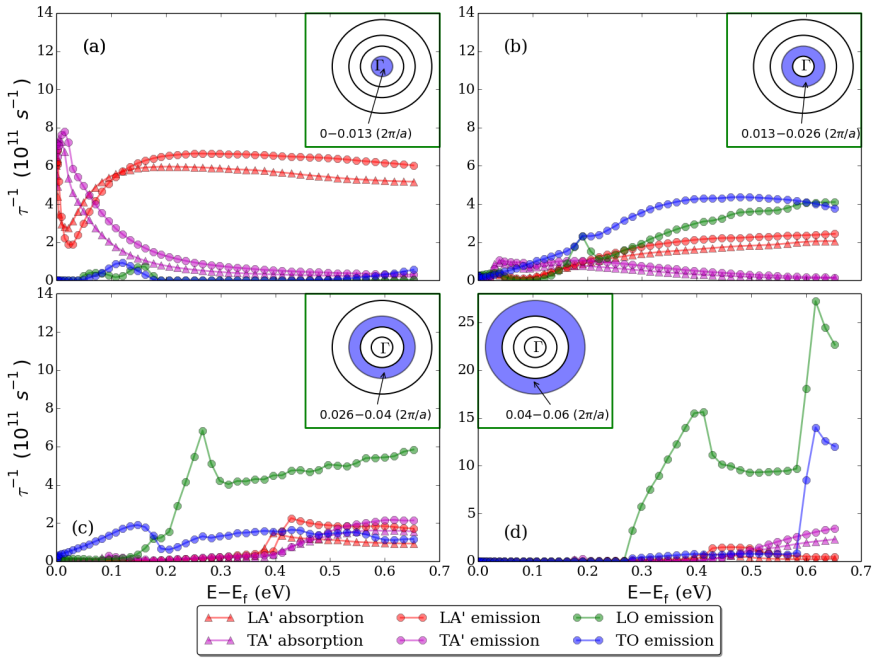

Figure 2.4: Intrinsic bilayer graphene electron scattering rates near the phonon Γ point at $T_e = 700$ K and $T_{ph} = 300$ K. (a) Phonon wavevectors $0-0.013\ 2\pi/a$. (b) Phonon wavectors $0.013-0.026\ 2\pi/a$. (c) Phonon wavevectors $0.026-0.04\ 2\pi/a$. (d) Phonon wavevectors $0.04-0.06\ 2\pi/a$. The increase of electron temperature does not change acoustic mode scattering rates, but does cause more optical mode scattering in the low energy range.

100 meV for the LA$'$ mode because final states have higher densities of states as shown in the inset of Fig. 2.1 (a). However, for high energy electrons the emission process is more active because the final states have higher occupations. This phenomenon is also observed in Fig. 2.4, where the transition happens at higher electron energy. As shown in Fig. 2.2 (b), (c) and (d), optical modes only participate in the emission process, because almost no phonons with energies higher than 200 meV are excited at 300 K.

Fig. 2.3 shows scattering rates due to interactions with K-point phonons at $T_e = 300$ K and $T_{ph} = 300$ K. Similar to results at phonon Γ point, significant LO and TO mode absorption does not occur. Electrons primarily interact with TO mode phonons at the K point due to large electron-phonon coupling strength.

We also investigate temperature effects on scattering rates by increasing the electron temperature T_e from 300 K to 700 K with the phonon temperature T_{ph} fixed at 300 K in Figs. 2.4 and

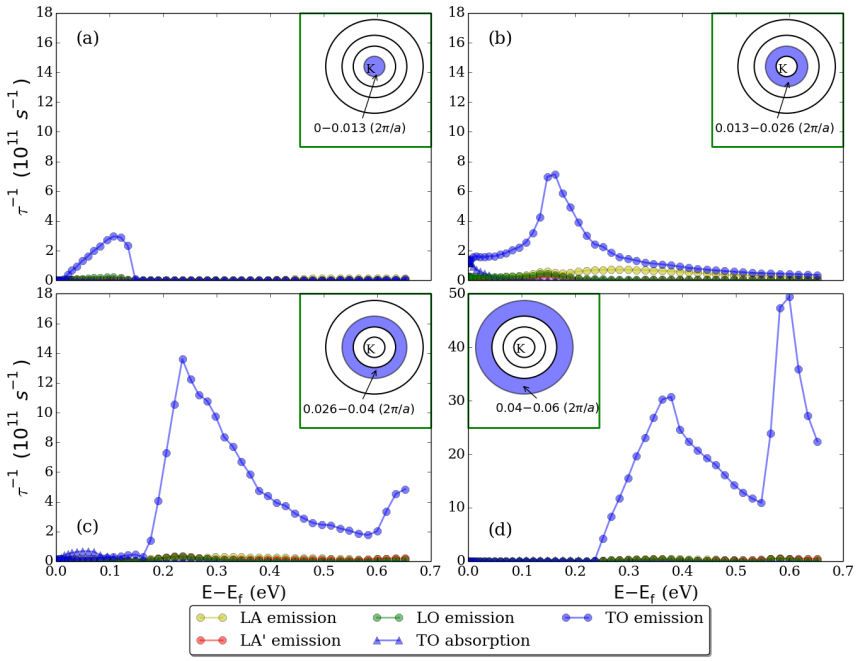

Figure 2.5: Intrinsic bilayer graphene electron scattering rates at the phonon K point at T_e = 700 K and T_{ph} = 300 K. More TO mode scattering occurs due to the expansion of the Fermi window. (a) Phonon wavevectors $0-0.013\ 2\pi/a$ from the phonon K point. (b) Phonon wavectors $0.013-0.026\ 2\pi/a$ from the phonon K point. (c) Phonon wavevectors $0.026-0.04\ 2\pi/a$ from the phonon K point. TO absorption emerges. (d) Phonon wavevectors $0.04-0.06\ 2\pi/a$ from the phonon K point.

2.5. Fig. 2.4 demonstrates that increasing the electron temperature does not influence the acoustic modes while causing more optical phonon emission at the phonon Γ point in the low energy range as a consequence of more available final states, but the increase compared with Fig. 2.2 is not very significant. The effects on K-point phonons are similar, as shown in Fig. 2.5. The scattering starts to involve the TO absorption process due to the expansion of the Fermi window. The total scattering rates from phonon Γ and K points are shown in Fig. 2.6. At low electron energies, the scattering rates increase with electron temperature, and the major contribution is from increased TO phonon scattering.

To explore the effects of doping levels on photoconductivity, we first calculate the temperature change with time and the corresponding heat flow into Γ-point and K-point acoustic and optical phonons based on Eqs. 2.3 and 2.4. We choose a starting electron temperature $T_e = 2000$ K and lattice temperature $T_{ph} = 300$ K, and allow the system to relax for bilayer graphene with Fermi

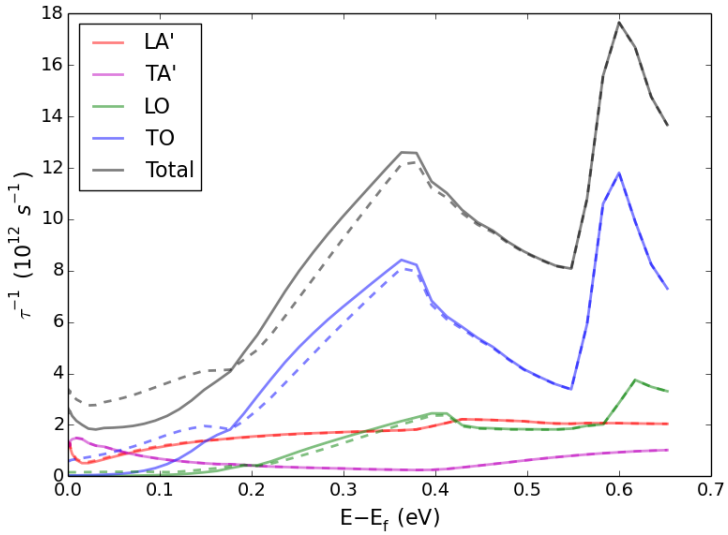

Figure 2.6: Bilayer graphene electron-phonon scattering rates from phonon Γ and K points at 300 K and 700 K. Solid lines denote scattering rates at T_e = 300 K and dashed lines denote scattering rates at T_e = 700 K.

levels 10 meV, 20 meV, 40 meV, and 60 meV respectively. Fig. 2.7 (a) shows that the thermalization process for bilayer graphene with $E_{fermi} = 10$ meV requires 60 ps to reach equilibrium, and the phonon temperature remains almost constant around 303 K because of the large phonon heat capacity. The electron temperature drops rapidly to 1200 K during the first 0.4 ps. Therefore even if the initial electron temperature may not be a precise estimate, further calculations are not severely affected. From Fig. 2.7 (b), at temperatures above room temperature, most energy loss by electrons flows to optical phonons near the phonon K point because of strong interactions with electrons indicated by Figs. 2.3 and 2.5 and because the population of these modes requires high energies. As the electron temperature approaches 303 K after around 42 ps, the energy diverted to Γ point optical modes is lower than acoustic modes because optical modes rarely interact with low energy electrons near the Γ point.

Using the electron and phonon temperatures obtained from the two-temperature model, we calculated photoconductivities at four specific times, t = 2.8 ps, t= 4.8 ps, t = 5.8 ps and t = 6.8 ps, and compared with prior experimental results. We plot only t = 2.8 ps and t = 5.8 ps in this work as shown in Fig. 2.8. The case E_{fermi} = 10 meV matches with experimental values best in terms of both trend and intersection of the real and imaginary parts at all four times. The negative imaginary

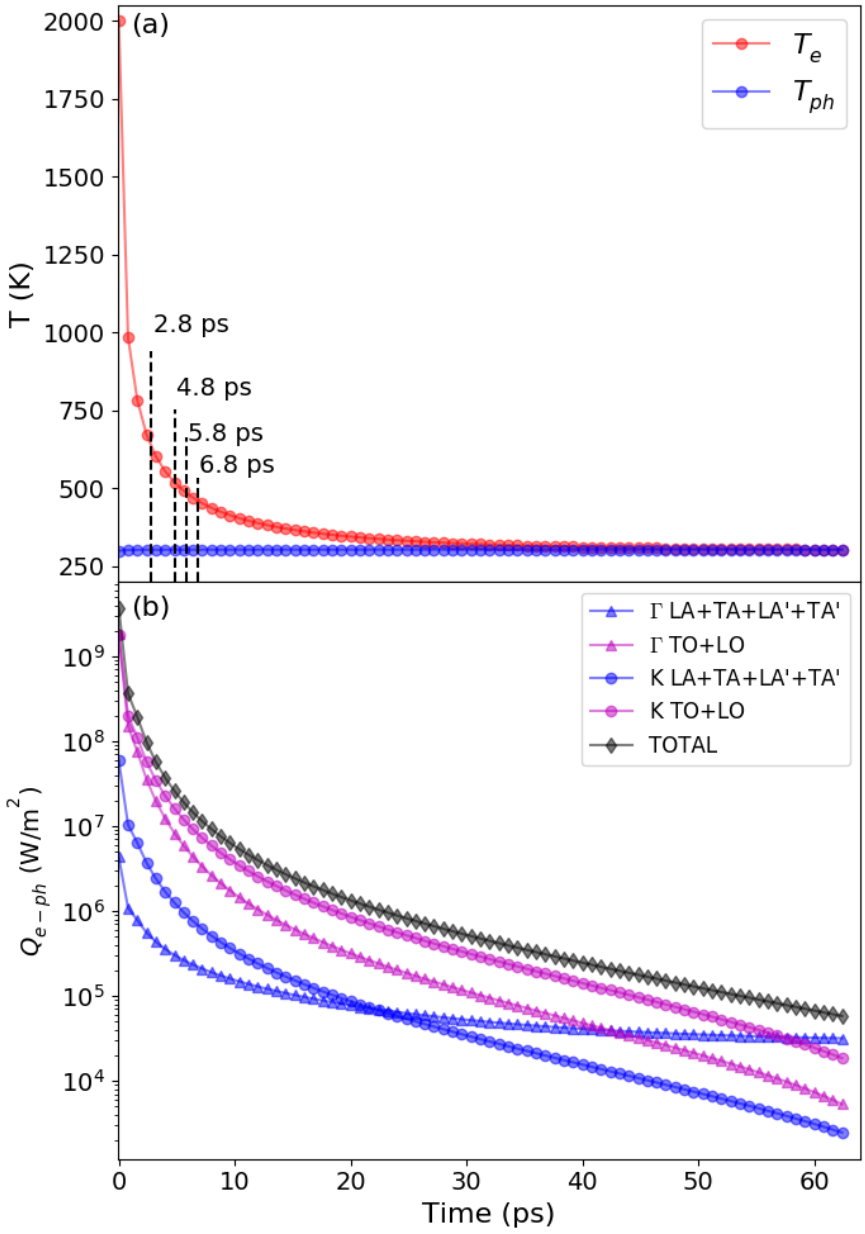

Figure 2.7: Two-temperature model for bilayer graphene with E_{fermi} = 10 meV. (a) Electron and lattice temperature changes as functions of time. The thermalization process takes 60 ps to reach equilibrium. The electron temperature drops drastically (by approx. 800 K) in the first 0.4 ps while the lattice temperature remains almost constant around 303 K. (b) Heat flux to the phonon Γ point and K point acoustic and optical modes. Most heat is diverted to K-point phonon optical modes. After 42 ps, heat transfer to Γ point acoustic modes exceeds that to Γ point optical modes.

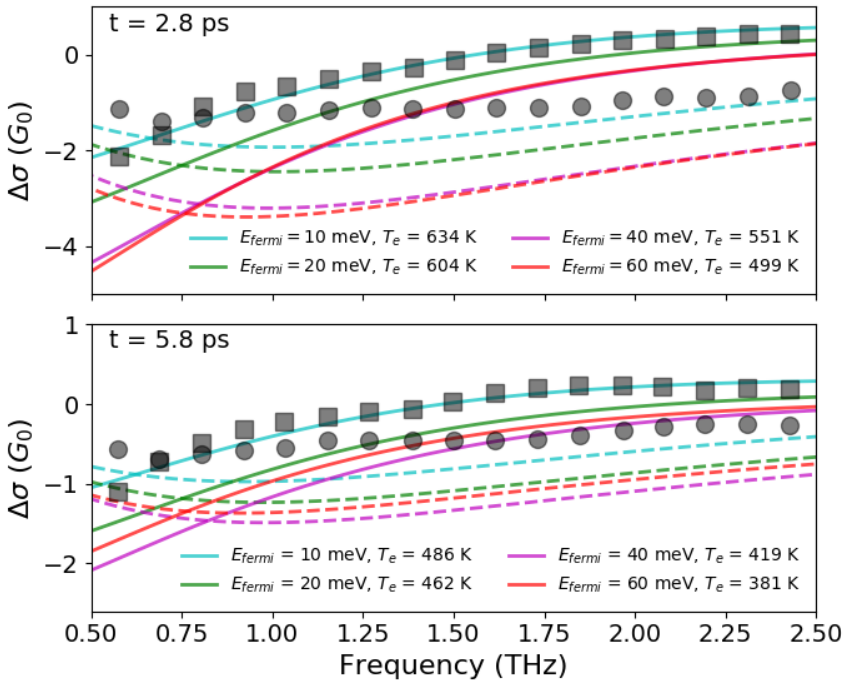

Figure 2.8: Photoconductivity evolution. Squares and circles are experimental data [62] for real and imaginary parts of photoconductivity, solid lines denote calculated real parts, and dashed lines denote calculated imaginary parts. The electron and lattice temperatures at each time step are obtained from our previous two-temperature calculations.

part can be qualitatively explained by an increase of temperature that amplifies overall scattering rates. The imaginary part goes to 0 as the probe frequency increases to values considerably larger than the overall scattering rates, because the effect of increased scattering become insubstantial and eventually diminishes. At t = 2.8 ps, the real part of photoconductivity decreases significantly with doping level at low probe frequencies due to enhanced electron-phonon scattering. Note that at t = 5.8 ps, the conductivity for E_{fermi} = 40 meV is higher than that for E_{fermi} = 60 meV because the heat loss to phonons is more severe for E_{fermi} = 60 meV. Thus the electron temperature is lower than that for E_{fermi} = 40 meV at the same time even though the former has higher density of states. As the relaxation proceeds, the real part of photoconductivity increases because the electron temperature decreases and weakens electron-phonon scattering. Fig. 2.9 shows that from t = 2.8 ps to t = 5.8 ps, electron-phonon scattering rates decrease and the major reason for this decrease is the reduction of TO phonon scattering. Scattering from acoustic phonons is insensitive to temperature but that from optical modes depends strongly on temperature. At temperatures higher than 1000

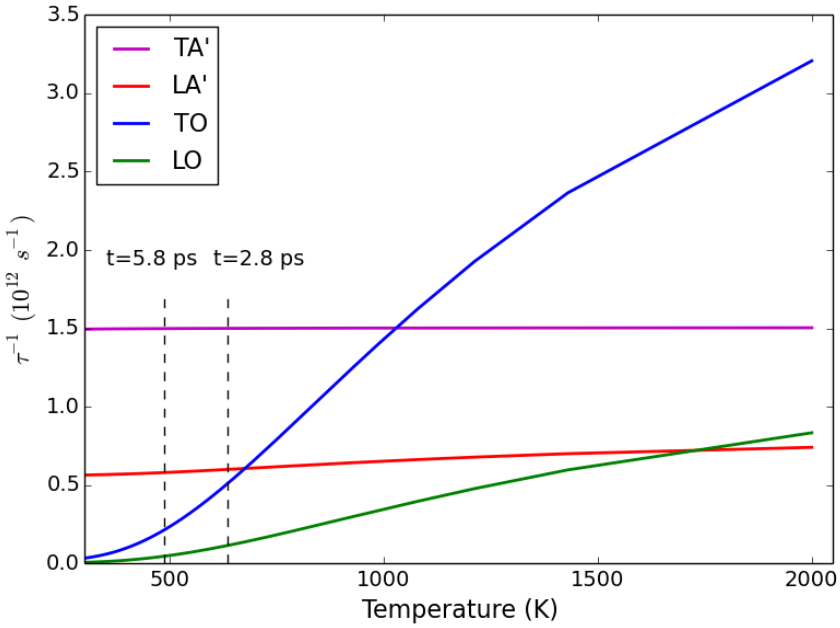

Figure 2.9: Electron scattering rates at Fermi level in bilayer graphene with E_{fermi} = 10 meV due to interactions with different phonon branches . Dashed lines denote scattering rates at t = 2.8 ps (T_e = 634 K) and t = 5.8 ps (T_e = 486 K).

K, TO mode phonon scattering dominates over other branches. At temperatures lower than 600 K, TA$'$ and LA$'$ mode scattering dominates over TO and LO mode phonons which does not contradict the result shown in Fig. 2.7 . Heat flux to acoustic phonons is significantly smaller than that to optical phonons from t = 2.8 ps to t = 6.8 ps because optical phonons require more energy to be populated. The real part also increases with probe frequency because the scattering time is comparably longer for carriers to react to electric field oscillations. Similarly, differences in conductivity between different doping levels are smaller at high frequencies where the scattering effects are less prominent.

Assuming $T_e = T_L$ = 300 K and following the approach in [82], we combine contributions from the deformation potential and gauge field, and then extract an effective deformation potential coupled to a single phonon mode. The extracted $E_{1,\text{eff}}$ is 22 eV calculated with Eq. 2.13 for an effective phonon group velocity of $v_{ph} = 2.0 \times 10^4$ m/s. Fig. 2.2 indicates that both LO and TO modes contribute to scattering, and we use a single phonon optical deformation potential to represent LO and TO modes at the phonon Γ point. The corresponding phonon frequency $\omega_{\text{o,LO/TO,}\Gamma}$ is 200 meV. At

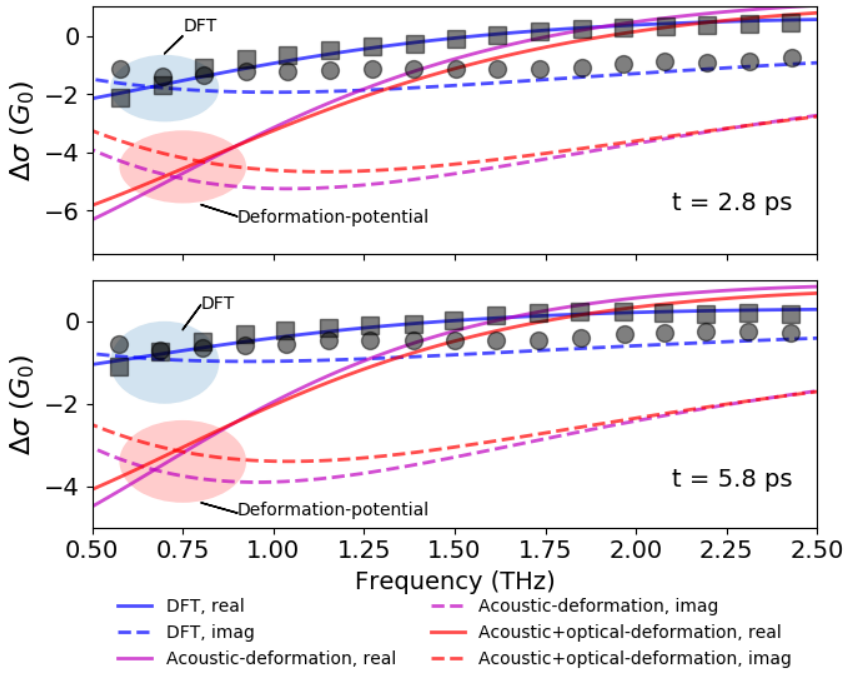

Figure 2.10: Comparison of photoconductivity calculations from DFT and the deformation-potential method. Squares and circles are experimental data [62] for real and imaginary parts of photoconductivity. Solid lines and dashed lines denote calculated real and imaginary components of photoconductivity, respectively. The conductivity predicted by the deformation-potential model deviates from the experimental data significantly in the low probe frequency regime.

the phonon K point, electrons mainly interact with the TO mode; therefore we use the K-point TO phonon frequency $\omega_{\mathrm{o,TO,K}} = 166$ meV in Eq. 2.14. The calculated $D_{\mathrm{o,LO/TO,\Gamma}}$ is 1.8 eV/Å, and $D_{\mathrm{o,TO,K}}$ is 2.5 eV/Å.

We further calculated deformation-potential scattering rates according to Eq. 2.11 with the derived deformation potentials and calculated photoconductivity for E_{fermi} = 10 meV at four different times. As shown in Fig. 2.10, the real part of photoconductivity calculated using the acoustic-deformation potential deviates significantly from the experimental data, as opposed to DFT predictions. The inclusion of an optical-deformation potential slightly improves the predictions for both real and imaginary parts; however the deviation from experiments and DFT results is still large. This indicates that momentum-dependent electron-phonon scattering potential and scattering rates are likely required to achieve accuracy in photoconductivity calculations.

Because defects indeed exist in the experimental bilayer graphene samples even though the

concentration may be low, we expect a discrepancy between our calculations and measurements. Apart from electron-phonon scattering, short-range scattering also occurs in reality. Another factor is the indeterminism of the electron temperature, without which the calculated photoconductivity is not accurate. The two-temperature model could also be a source of discrepancy, but its effects are likely not significant. Phonon temperatures could depend on branches and their positions in reciprocal space; however they should always be around 300 K because of their large heat capacities.

2.5 Conclusions

This work demonstrates first-principles methods for the calculation of eletron-phonon coupling, based on which an effective acoustic deformation potential $E_{1,\text{eff}} = 22$ eV is estimated for bilayer graphene. The Drude model with DFT-calculated scattering rates predicts the correct trend for real and imaginary parts of photoconductivity. By increasing the doping level, the electron-phonon scattering is enhanced especially for low probe frequencies. The comparison between our DFT and deformation-potential approach calculations indicates that first-principles methods result in less deviations from experiments. The small deviations from experimental values could derive from several causes such as defects in the sample, short-range scattering, and electron temperature inaccuracies. The initial electron temperature is related to the incident light frequencies, intensities and the sample area illuminated. A possible direction of the future work could be determining the initial electron temperature accounting for fast electron-electron scattering that involves many-body effects.

CHAPTER 3

Thermal Boundary Conductance across Co/Cu Interfaces with Spin-lattice Interactions

3.1 Introduction

The origin of spin caloritronics is the so-called spin Seebeck effect (SSE) related to the generation of spin voltage driven by a temperature gradient. Both conduction electrons and spin waves (magnons) carry spin currents, but the range of the former is only hundreds of nanometers while the latter can persist for millimeters. Experiments have observed SSE in magnetic insulators where conduction electrons are absent, and this phenomena highlights the role of spin waves in producing SSE [83, 84]. SSE has also been detected in a $Ni_{81}Fe_{19}$/Pt wire on an electrically and magnetically isolated sapphire substrate [85] to demonstrate that SSE originates from a non-equilibrium distribution of magnons in the ferromagnet that interact with phonons in the substrate. The phonon-driven redistribution of magnons has also been studied theoretically with a phenomenological phonon-magnon drag model [86].

In the area of heat transport, magnon-phonon interactions offer potential applications in engineering thermal devices with magnetic materials. In our previous work [87], the effect of magnon-magnon and magnon-phonon interactions on the thermal conductivity of BCC iron was modeled by combining molecular dynamics and spin dynamics. In this work, we present a method of calculating thermal boundary conductance between heterogeneous materials by integrating first-principles exchange constants and spin-lattice dynamics into the non-equilibrium Green's function (NEGF) method, and we apply the method to bulk Co and Co/Cu interface.

Fundamental understanding of carrier scattering and thermal transport is crucial in the design of

electronic devices and has long been of interest to researchers. However, theoretical work on interfacial heat transport involving spin-lattce interactions is rare. Zhang et al. [88] conducted thermal conductance calculations of a hypothetical 1D atomic chain within the framework of the NEGF method and self-consistent Born approximation (SCBA). The authors found that magnon-phonon interactions cause thermal rectification and negative differential thermal conductance in the presence of an external magnetic field at a ferromagnetic-normal insulator interface; these effects could be tuned by adjusting the external magnetic field. Despite the fact that SCBA is computationally intensive and a 1D model was used, the system was not representation of a real material because arbitrary force constants, exchange constants and magnon-phonon coupling strength constants were chosen.

The purpose of this work is to develop a method to predict thermal boundary conductance at 3D heterogeneous interfaces with spin-lattice interactions. To ensure that the problem is computationally tractable, we calculate magnetic properties of bulk Co and a Co/Cu (001) interface with small lattice mismatch from first-principles. The obtained Heisenberg exchange constants are then incorporated into spin-lattice dynamics. We further compute interfacial conductances at different temperatures by calculating autocorrelations of heat flux across the interface sampled at different time steps after the spin and lattice subsystems have reached equilibrium. We also compare the results from the EMD and the NEGF methods. Inelastic scattering is considered by attaching Büttiker probes to atoms in the device, and the probe scattering rates are obtained in each contact by fitting their bulk thermal conductivities. The remainder of this work details the various computational methods employed, their integration, and predictions for bulk and interfacial transport.

3.2 Methods

3.2.1 Spin-lattice dynamics

Spin-lattice dynamics calculations were conducted with the modified SPIN package [89] incorporated into LAMMPS [90]. The Hamiltonian for a spin-lattice coupled system is:

$$H_{sl} = \sum_i \frac{\boldsymbol{p}_i^2}{2m} + \sum_{i,j} U(R_{ij}) - \sum_{i \neq j} J(R_{ij}) \boldsymbol{S}_i \cdot \boldsymbol{S}_j + \sum_{i \neq j} J(R_{ij}) \tag{3.1}$$

Here, the second term is the inter-atomic potential; we use the Embedded-Atom Method (EAM) potential for the system. The third term considers the classical Heisenberg exchange interactions between atoms. The last term is the energy compensation for the spin system at 0 K.

The equation of motion for the spin degree of freedom is derived from a generalized Poisson bracket [91] as

$$\begin{aligned} \frac{d\boldsymbol{S}_i}{dt} &= \boldsymbol{S}_i \times \boldsymbol{H}_i \\ &= \boldsymbol{S}_i \times (-\frac{1}{\hbar} \frac{dH_{sl}}{d\boldsymbol{S}_i}) \end{aligned} \tag{3.2}$$

Eq. 3.2 describes the spin precession about the direction of the the local effective field $\boldsymbol{H}_i$. $\boldsymbol{S}_i$ is the spin angular momentum associated with atomic site i, and the magnitude of $\boldsymbol{S}_i$ is proportional to the magnetic moment $\boldsymbol{\mu}_i$ calculated from first principles. Similarly, the governing equations for updating the lattice degrees of freedom are:

$$\frac{d\boldsymbol{R}_i}{dt} = \frac{\boldsymbol{p}_i}{m_i} \tag{3.3}$$

$$\frac{d\boldsymbol{p}_i}{dt} = \sum_j \left[-\frac{dU}{d\boldsymbol{R}_i} + \frac{dJ}{d\boldsymbol{R}_i} (S_i \cdot \boldsymbol{S}_j - 1) \right] \tag{3.4}$$

3.2.2 Heat flux and thermal conductivity from equilibrium molecular dynamics (EMD)

The heat flux generated by lattice vibrations is defined as:

$$Q_l^x = \frac{1}{V}\left[\sum_i e_i v_i^x - \sum_i (\boldsymbol{\tau}_i \cdot \boldsymbol{v_i})^x\right] \tag{3.5}$$

where e_i, v_i^x, and $\boldsymbol{\tau}_i$ are sum of kinetic and potential energy, velocity in the x direction, and stress on atom i, respectively. If only two-body interactions are considered, the second term in Eq. 3.5 becomes $-\frac{1}{2}\sum_{i<j}(\boldsymbol{f}_{ij}\cdot(\boldsymbol{v}_i+\boldsymbol{v}_j))r_{ij}^x$ where $\boldsymbol{f}_{ij}$ is the force exerted on atomic site i by atomic site j. The generation of force is not only due to the variation of inter-atomic potentials but also to the variation of exchange interactions that depend on inter-atomic distance, as indicated in Eq. 3.4.

Heat flux generated by spin fluctuations is calculated following the approach used in our previous work [87]. With an imaginary interface separating the left and right sides of the system, interfacial heat flux is the rate of magnetic energy change on one side of the interface due to interactions with spins on the other side of the interface.

The rate of change in the magnetic potential energy is related to the change in the local magnetic field via:

$$\begin{aligned}\frac{dU_{mag,i}}{dt} &= \hbar \boldsymbol{S}_i \cdot \frac{d\boldsymbol{H}_i}{dt} \\ &= J(\boldsymbol{R}_{ij})\boldsymbol{S}_i \cdot \frac{d\boldsymbol{S}_j}{dt}\end{aligned} \tag{3.6}$$

The heat flux induced by spin fluctuations across the interface is then derived from Eq. 3.6 as:

$$Q_{mag} = -\frac{1}{2A}\sum_{i\in L, j\in R} J(R_{ij})\left[\boldsymbol{S}_i \cdot \frac{d\boldsymbol{S}_j}{dt} - \boldsymbol{S}_j \cdot \frac{d\boldsymbol{S}_i}{dt}\right] \tag{3.7}$$

where the $\frac{1}{2}$ prefactor indicates that the magnetic energy is pairwise and shared by two individual spins.

Thermal conductivity is proportional to the auto-correlation of heat flux at equilibrium and is

calculated based on the fluctuation-dissipation theorem [92]:

$$\begin{aligned}\kappa &= \frac{V}{k_B T^2}\int_0^\infty \langle Q(t)Q(0)\rangle dt \\ &= \frac{V}{k_B T^2}\int_0^\infty \Big[\langle Q_l^x(t)Q_l^x(0)\rangle + \langle Q_{mag}(t)Q_{mag}(0)\rangle \\ &+ 2\langle Q_l^x(t)Q_{mag}(0)\rangle\Big] dt\end{aligned} \tag{3.8}$$

3.2.3 Thermal boundary conductance calculations with Non-equilibrium Green's function (NEGF) approach

The general Green's function is written as:

$$G = (\omega^2 I - H_d - \Sigma_1 - \Sigma_2 - \Sigma_{BP})^{-1} \tag{3.9}$$

where H_d is the dynamical matrix in the device region, Σ_1 and Σ_2 are self energies in the two contacts, and Σ_{BP} is the Büttiker probe self energy that incorporates inelastic scattering and takes the form:

$$\Sigma_{BP}(\omega) = -i\frac{2\omega}{\tau(\omega)} \tag{3.10}$$

Energy conservation in each Büttiker probe must be satisfied:

$$Q_i = \sum_{q_{||}} \int_0^\infty \frac{\hbar\omega}{2\pi} Tr(\Sigma_i^{in} A - \Gamma_i G^n) d\omega = 0 \tag{3.11}$$

where Σ_i^{in} represents the in-scattering from Büttiker probe i, A is the spectral function, Γ_i is the imaginary part of the Büttiker probe self energy and G^n is the lesser Green's function. Σ_i^{in} and Γ_i are both block-diagonal; therefore only block-diagonal terms of A and G^n are needed, and the recursive Green's function (RGF) method can be used. The avoidance of direct inversions of Green's functions makes the computation feasible especially for large-scale devices. Because Σ_i^{in} and G^n depend on Büttiker probe temperatures, Eq. 3.11 is solved iteratively using the Newton-Raphson technique. Details of derivation and implementation related to the RGF formulation can

be found in [5, 93]. Similarly, phonon temperatures are computed by solving:

$$\sum_{q_{||}} \int_0^{\infty} \omega^2 G^n(\omega; q_{||}) d\omega = \sum_{q_{||}} \int_0^{\infty} \omega^2 A(\omega; q_{||}) f_{BE}(\omega, T_p) d\omega \tag{3.12}$$

where $f_{BE}(\omega, T_p)$ is the phonon distribution function at equilibrium phonon temperature T_p.

3.2.4 First-principles calculations

Electronic structure calculations were performed using the spin-polarized scalar relativistic Korringa-Kohn-Rostoker Green's function method (SPR-KKR)[94] and linear muffin-tin orbital method (LMTO) [95]. In both methods, spherically symmetric potentials inside muffin-tin spheres are matched by flat potentials in the interstitial regions at the boundary of muffin-tin spheres, corresponding to a certain energy level. The search of the energy values is simplified by using multiple-scattering theory in the former method and by linearizing basis functions in the latter.

The exchange-correlation was evaluated within the local density approximation (LDA) using the Vosko-Wilk-Nusair functional [96]. The angular momentum expansion cutoff $l_{max} = 2$ and a regular k-mesh of $20 \times 20 \times 2$ were chosen in the self-consistent calculations. The energy convergence threshold was set to be 10^{-5} Ry. The atomic sphere approximation (ASA) is used in our current calculations considering that the system under study is closely packed and muffin-tin potentials are close to full potentials.

Figure 3.1(a) shows the band structure of fcc cobalt with spin up and spin down contributions highlighted in different colors. Figure 3.1(b) shows a comparison of fcc cobalt band structures calculated from KKR-ASA and LMTO-ASA methods. The band structures produced by these two methods overlap within 1 eV of the Fermi level, confirming the validity of calculations from both methods.

The exchange constants are obtained with the Lichtenstein formula [97]:

$$J_{ij} = \frac{1}{4\pi} Im \int^{E_F} dE \; Trace(t_{i\uparrow}^{-1} - t_{i\downarrow}^{-1}) \tau_{\uparrow}^{ij} (t_{j\uparrow}^{-1} - t_{j\downarrow}^{-1}) \tau_{\downarrow}^{ij} \tag{3.13}$$

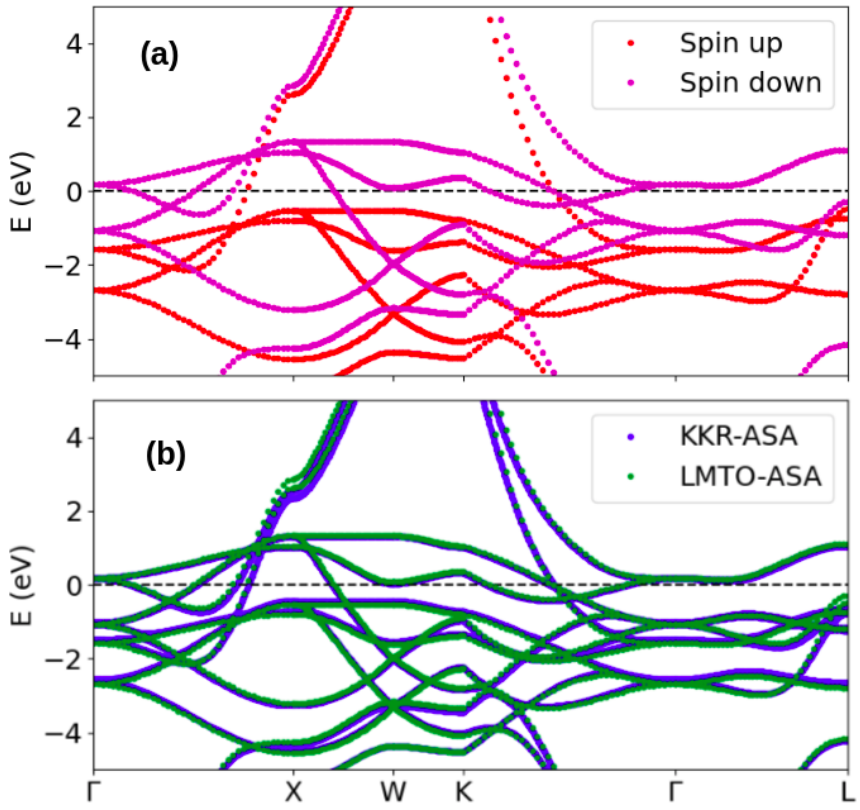

Figure 3.1: (a) Electron band structure of fcc cobalt showing spin up and spin down contributions. (b) Comparison of fcc cobalt electron band structures obtained from KKR-ASA and LMTO-ASA methods.

where t is single site t-matrix and τ is the scattering path matrix. The computed exchange constants are further fitted to a Bethe-Slater curve as:

$$J(R_{ij}) = 4\alpha\left(\frac{R_{ij}}{\delta}\right)^2\left(1-\gamma\left(\frac{R_{ij}}{\delta}\right)\right)^2 e^{-(\frac{R_{ij}}{\delta})^2}\Theta(R-R_{ij}) \tag{3.14}$$

3.2.5 Spin-lattice dynamics and thermal conductivity

Lattice dynamics was conducted in a NVT ensemble and the Langevin thermostat was applied to reach the targeted lattice temperature. The spin-lattice dynamics simulation was then run for 400 ps in order for the spin and lattice subsystems to equilibrate. The exchange interaction between spins was included as an interatomic distance dependent function, obtained by fitting first-principles data to Eq. 3.14. Heat flux was calculated within a period of 800 ps based on a NVE ensemble. A 0.2

fs timestep was chosen in all the molecular dynamics calculations. Depending on the system of interest and the temperature conditions, the autocorrelation time in Eq. 3.8 varies.

3.3 Results and discussion

3.3.1 Thermal conductivity

Figure 3.2 shows first-principles calculated exchange constant values for fcc cobalt at discrete lattice points, as well as the fitted continuous curve to Eq. 3.14. Here, $\alpha = 18.603$ meV, $\delta = 1.486$ Å, $\gamma = 1.7 \times 10^{-5}$, and $R = 6$ Å. The exchange interaction between first nearest neighbours is the strongest and the interaction decays exponentially with inter-atomic distances. The cutoff radius was chosen to be 6 Å, beyond which the exchange interaction is negligible.

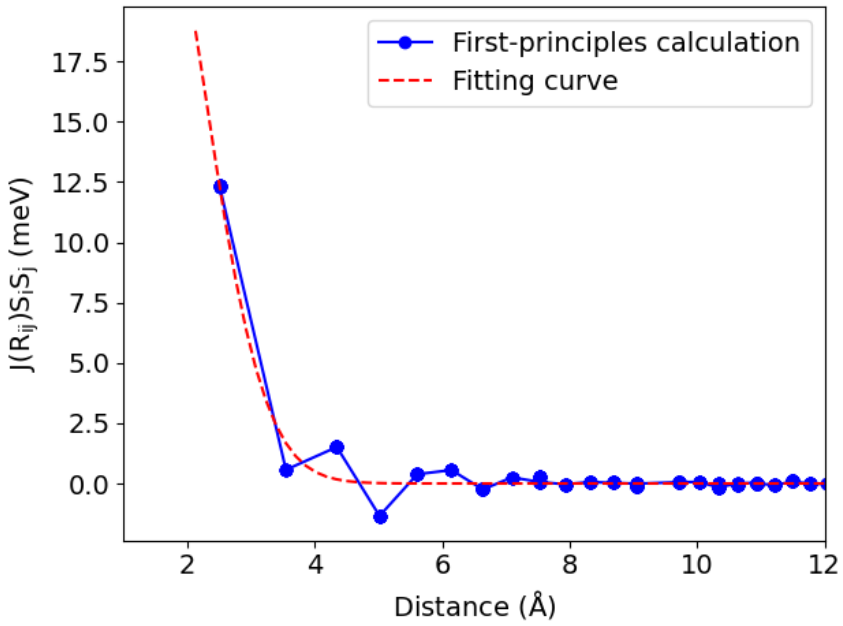

Figure 3.2: Exchange constants for fcc cobalt as a function of inter-atomic distance. The red dashed curve is the fitting result to continuous exchange constants.

To obtain a converged thermal conductivity, 30 independent runs for each individual temperature were performed and the results were averaged. Figure 3.3 shows that the thermal conductivity of bulk Co at 300 K reaches a plateau with a autocorrelation time longer than 10 ps. Magnon

thermal conductivity is comparable to phonon thermal conductivity in bulk Co. Magnon thermal conductivity decreases with temperature, as shown in Figure 3.4, due to the reduced effective total magnetization. The difference between phonon thermal conductivities calculated with and without spin-lattice interactions is insignificant, especially at high temperatures. The interatomic potential is dominant in determining the motion of cobalt atoms. At high temperatures, the effect of exchange interactions is less prominent because atoms are farther from each other than at low temperatures.

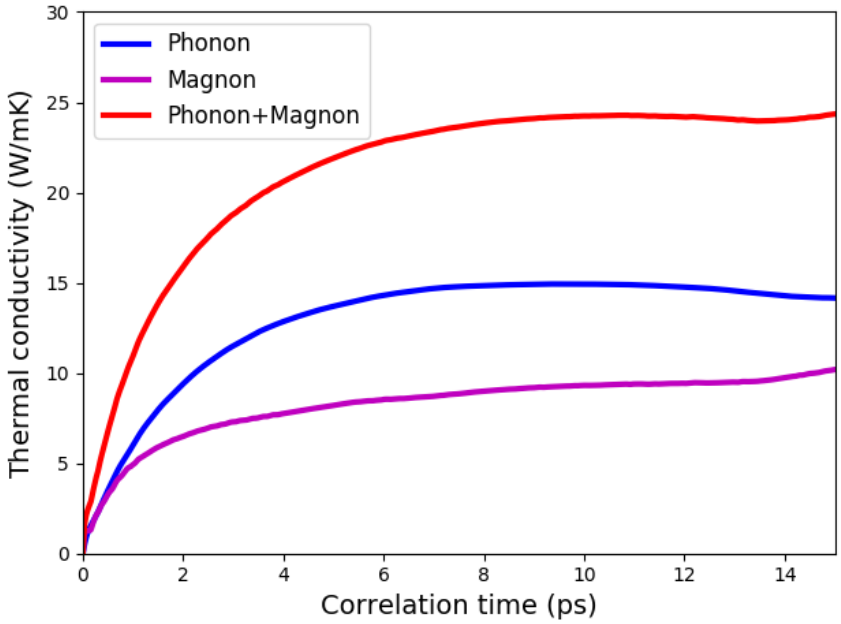

Figure 3.3: Thermal conductivity of Co calculated with EMD at 300 K

3.3.2 Thermal boundary conductance from EMD

To calculate interfacial phonon heat flux, Eq. 3.5 is modified as:

$$Q_l = -\frac{1}{2A}\sum_{i\in L}\sum_{j\in R}\boldsymbol{f}_{ij}\cdot(\boldsymbol{v}_i+\boldsymbol{v}_j) \tag{3.15}$$

where $\boldsymbol{f}_{ij} = \phi_{ij}d\boldsymbol{R}_j - \dfrac{dJ}{dR_{ij}}(S_i\cdot S_j - 1)\boldsymbol{e}_{ij}$ is the force acting on atom i by atom j and ϕ_{ij} is the second-order force constant between i and j.

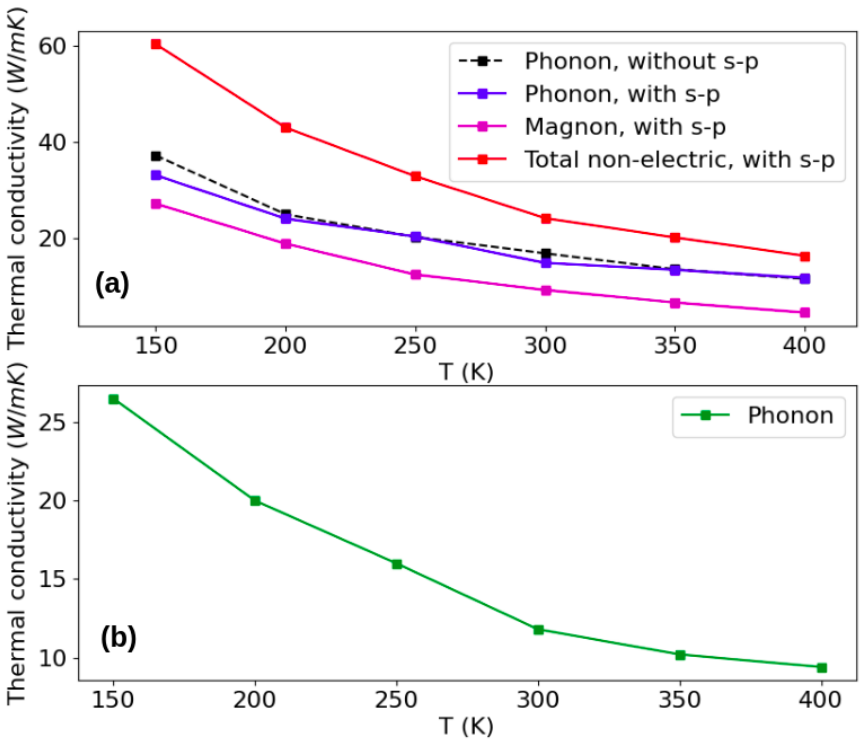

Figure 3.4: Thermal conductivities of bulk Co and Cu. (a) Thermal conductivity of Co with and without spin-phonon (sp) coupling. (b) Phonon thermal conductivity of Cu.

Interfacial thermal conductance is calculated using Puech's [98] formula:

$$G(T) = \frac{1}{Ak_BT^2}\int_0^\infty \langle Q(t)Q(0)\rangle dt \tag{3.16}$$

Thermal boundary conductance at the interface is then calculated by substracting the ballistic contact resistances from Eq. 3.16:

$$G_{interface} = \frac{G(T)}{1-\frac{1}{2}\left(\frac{G(T)}{G_{Co}(T)}+\frac{G(T)}{G_{Cu}(T)}\right)} \tag{3.17}$$

Similar to bulk Co, we calculated magnetic properties of the Co-Cu interface from first-principles. As shown in Figure 3.5(a), The interface structure is a supercell that consists of 8 layers of Co and 8 layers of Cu. Periodic boundary conditions are applied in all directions.

In contact with Cu, the magnetic properties of Co atoms next to the interface are modified.

As shown in Figure 3.5(b), the magnetic moment in Co atoms adjacent to the interface is reduced compared to that in bulk Co (indicated by the horizontal magenta line). Further, the Cu layer adjacent to the interface is magnetized and has a small magnetic moment of 0.00115 μ_B.

Figure 3.6(a) shows the exchange interaction constants between Co and Co atoms next to the interface. The nearest-neighbour exchange constants differ for inter-layer and intra-layer Co-Co interactions. The inter-layer Co-Co exchange constant is higher than that in bulk Co while the intra-layer Co-Co exchange constant remains unchanged. Figure 3.6(b) indicates that the exchange interaction between Co and Cu atoms next to the interface exists because the Cu layer connected to Co layer is magnetized, but the interaction is weak and two orders of magnitude smaller than the interaction between Co and Co atoms.

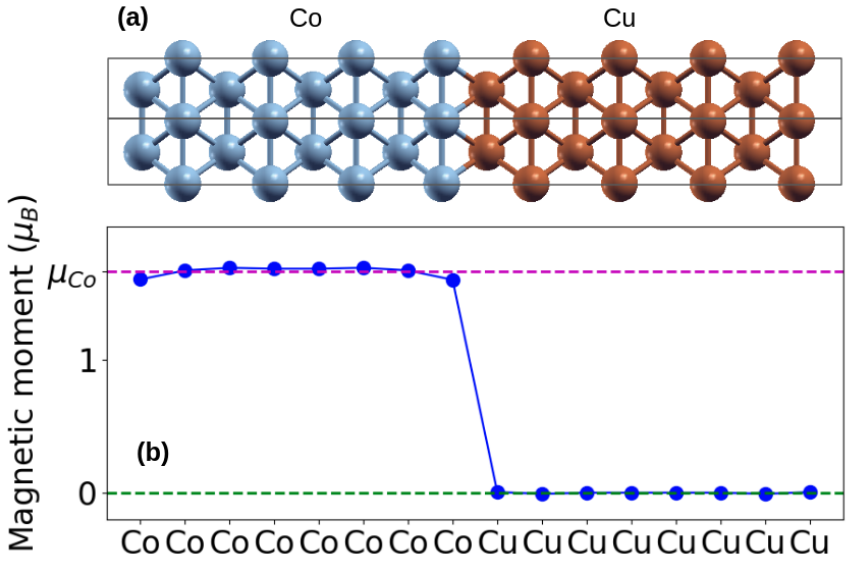

Figure 3.5: Co-Cu interface structure and magnetic moments on each layer. (a) Relaxed Co-Cu interface. Each box represents a unit cell in first-principles calculations. (b) Magnetic moments on each layer calculated from first-principles.

To clarity the effects of spin-lattice interactions, we calculated interfacial conductances with and without spins. Thermal boundary conductance decreases when magnon heat flux is considered, as indicated by Figure 3.7. Although the Cu layer at the interface is magnetized by Co, the magnetization and exchange interaction with Co layers are small. Within the Cu contact away from the interface, magnetic energy is not significantly transmitted. Magnon waves mainly interact with

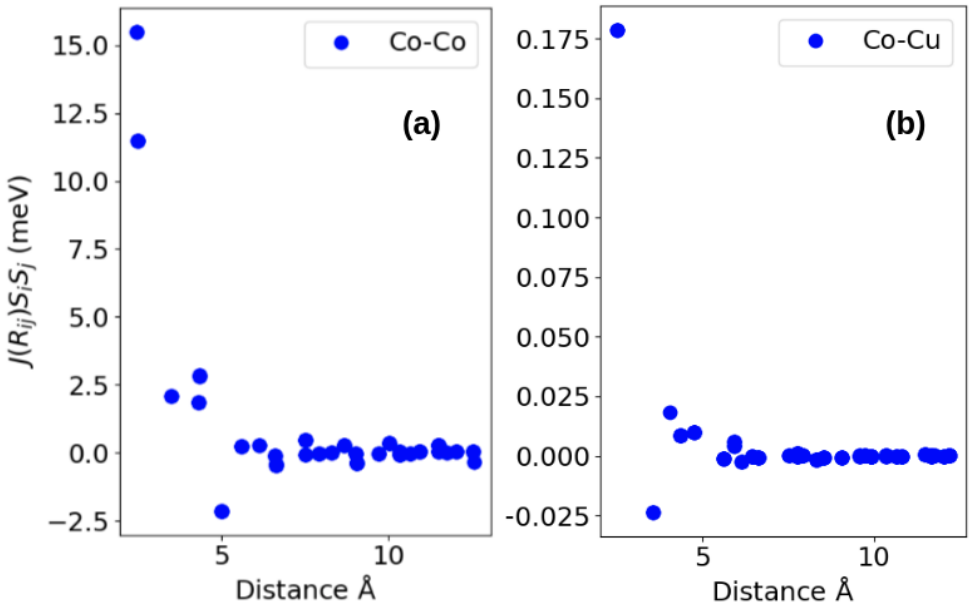

Figure 3.6: Exchange constants at the Co-Cu interface calculated from first principles. (a) Exchange constants between Co and Co atoms at the Co-Cu interface. (b) Exchange constants between Co and Cu atoms at the Co-Cu interface.

phonon waves on the Co side. The scattering between magnons and phonons on the Co side of the interface is responsible for the reduction of thermal boundary conductance when magnon waves are considered.

The weak effects of magnons on phonons are also observed in the small change of phonon density of states after including magnon effects. In Figure 3.8(a), we compare phonon density of states contributed by Co and Cu atoms at the interface with and without spin-lattice interactions. The densities of states were obtained from renormalized force constants at 300 K. In the presence of spin-lattice interactions, density of states slightly changes in the middle range of phonon frequencies, but the change is not significant. Figure 3.8(b) illustrates the heat flux oscillations with time for cases with and without spins, also showing that the effects of spin-lattice interactions on the motion of atoms are minimal.

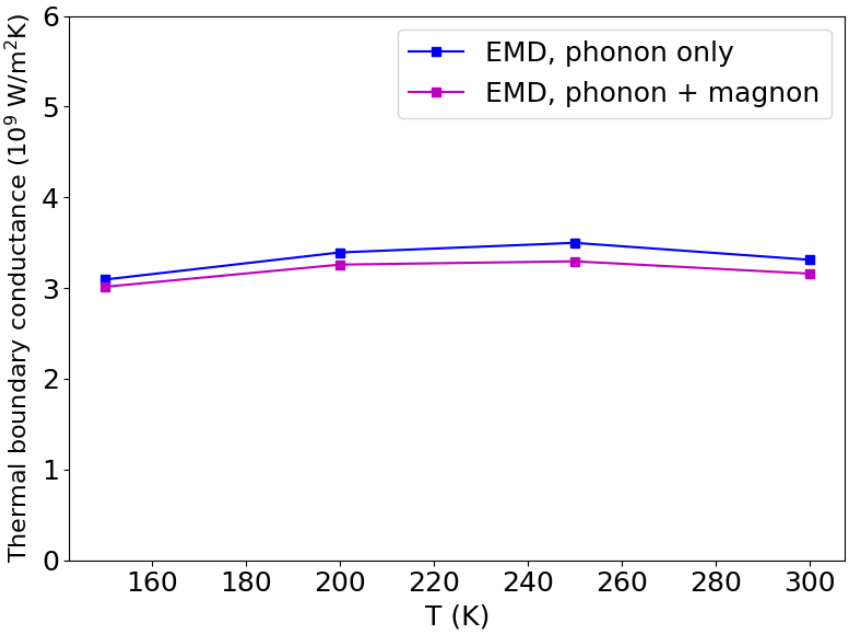

Figure 3.7: Thermal boundary conductance computed by EMD

3.3.3 Thermal boundary conductance from NEGF

The most essential part of solving the NEGF equations involves constructing the Green's function (Eq. 3.9). The dynamical matrix H_d in the device region (harmonic force constants) were obtained from spin-lattice dynamics with EAM potentials and were renormalized to finite temperatures. Büttiker probe scattering rates $\tau(\omega)$ in Eq. 3.10 on both sides of the interface were assumed to take the form $\tau(\omega) = A\omega^2$, where the temperature-dependent parameter A was obtained by fitting bulk thermal conductivities of Co and Cu obtained from molecular dynamics at corresponding temperatures.

Figure 3.9 illustrates two fitting processes using the NEGF method. Figure 3.9(a) calculates the length-dependent resistance while Figure 3.9(b) extrapolates the inverse of the thermal conductivity to infinite length. Both methods successfully fit the target phonon thermal conductivity of bulk Co at 300 K (15.1 W/mK) with the same Büttiker probe scattering rates.

By applying a small temperature gradient of 10 K across the device and iteratively solving Eq. 3.11 and Eq. 3.12, lattice temperatures in different layers of the device are calculated. Figure 3.10(a) shows the lattice temperatures in different regions of the device with a temperature gradient

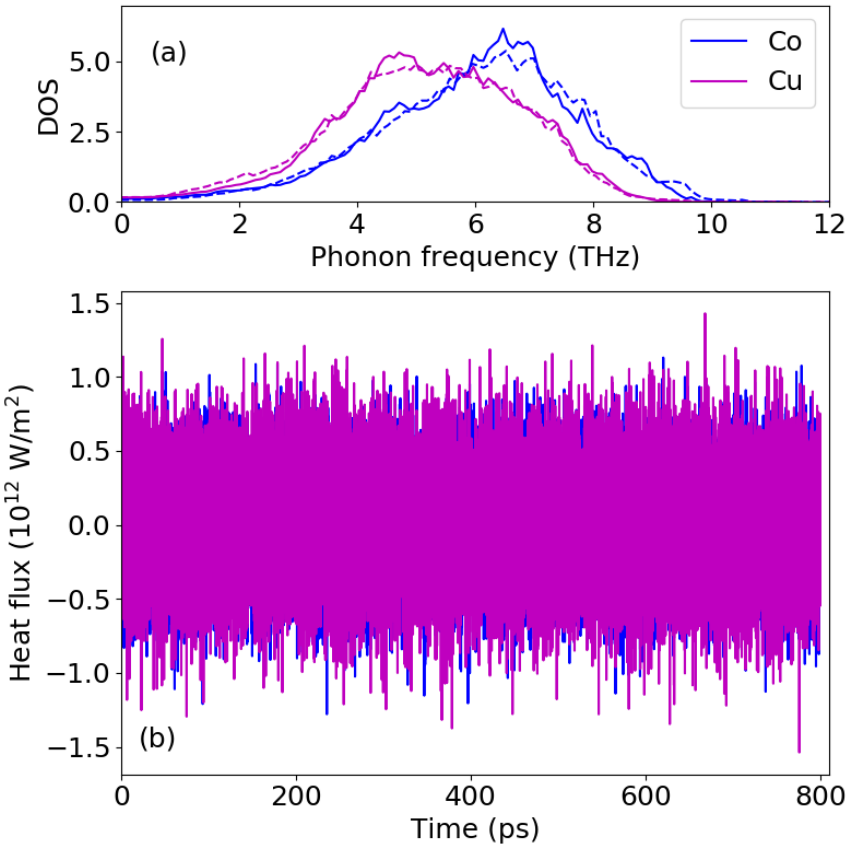

Figure 3.8: Interfacial density of states and heat flux across the interface. (a) Density of states at 300 K at the Co-Cu interface contributed by Co and Cu atoms, respectively. The solid lines indicate the case with spins and the dashed lines indicate the case without spins. (b) Heat flux across the interface at equilibrium. The magenta line represents the case with spins and the blue line represents the case without spins.

of 10 K applied across the Co and Cu contacts and the Co contact being at 300 K. The region on the left of the dashed line (0 Å from the center of the device) represents the Co contact, and the region on the right of the dashed line represents the Cu contact. The difference in bulk thermal conductivities of Co and Cu is larger when magnon effects are considered than when magnon effects are neglected; therefore the slope on the Cu side is steeper in the presence of magnons.

Spectral heat flux in both contacts has also increased in the middle range of phonon frequencies, as indicated in Figure 3.10(b). Even though the total heat flux has increased when magnon effects are included, the accumulated heat flux normalized by the total heat flux changes little in the entire frequency range as shown in Figure 3.10(c); therefore we observe a very small change in the

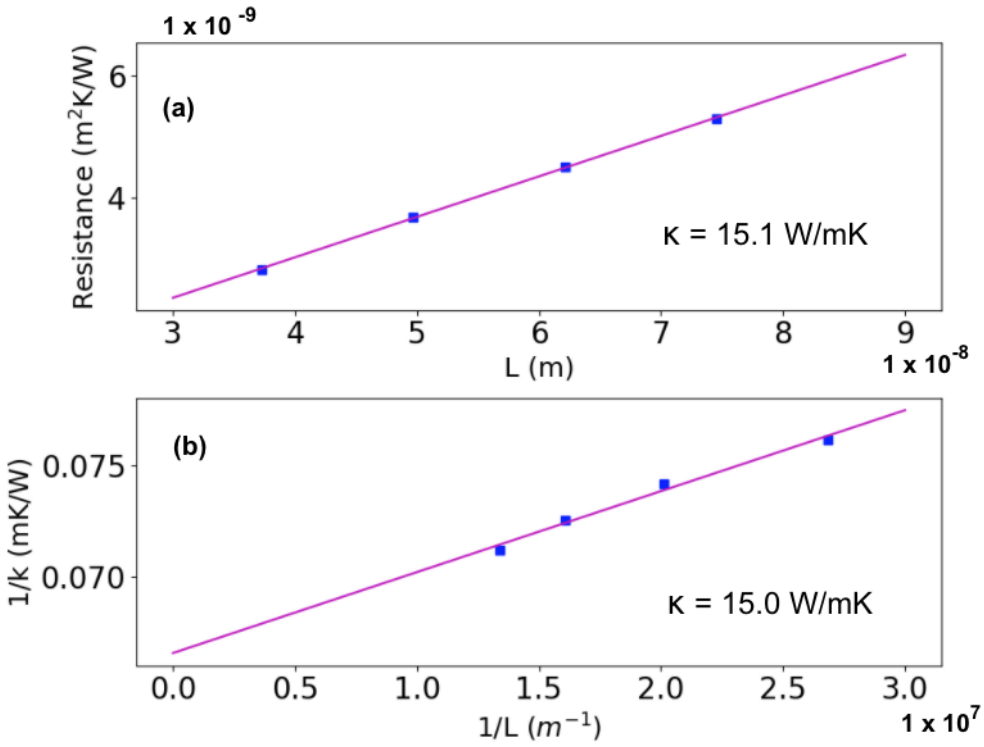

Figure 3.9: Fitting Co phonon thermal conductivity with spin-lattice interactions from linear fits to thermal resistance and from extrapolation of the inverse thermal conductivity. (a) Fitting process of calculating the length-dependent resistance. (b) Fitting process of extrapolating the inverse of the thermal conductivity to infinite length.

thermal boundary conductance with and without magnon effects as shown in Figure 3.11.

Figure 3.11 also displays similar trends of thermal boundary conductances predicted by the NEGF method and by the EMD method. With spins taken into account, thermal boundary conductance decreases because the interface acts as a barrier for the transmission of magnetic waves incident on the Co side. The handling of inelastic scattering is a major factor that contributes to discrepancies between thermal boundary conductances calculated by the EMD and the NEGF methods. While the EMD method incorporates inelastic scattering through the anharmonicity of the EAM potentials, the NEGF method uses empirical Büttiker probe scattering rates that were obtained by fitting the thermal conductivities of the two contacts (Co and Cu contacts). The domain size effect is another factor that could result in the difference in the EMD and the NEGF calculations. This effect is more significant in the EMD method because the size of the interface in the EMD calculations can not extend to infinity due to the infeasible computational cost, but the

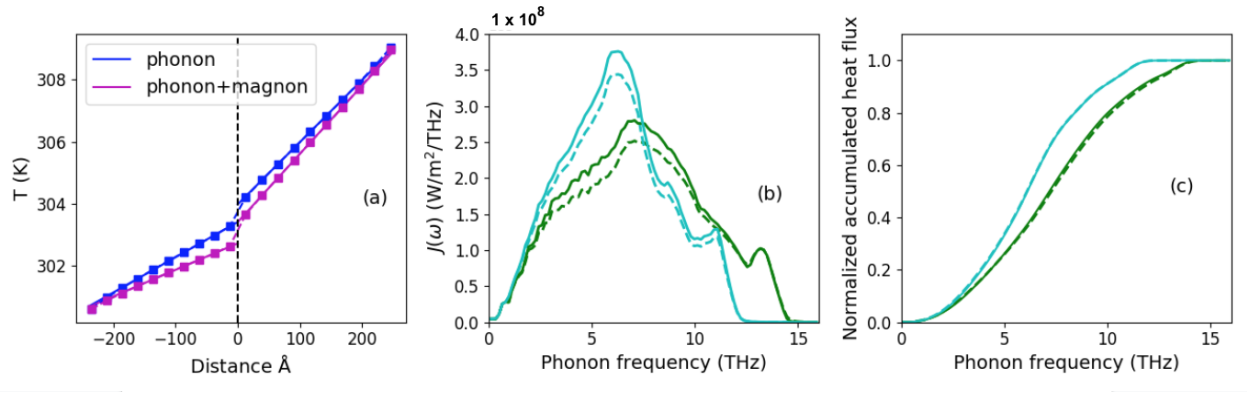

Figure 3.10: (a) Device temperature profile. The blue line represents the case with pure phonon scattering, and the magenta line represents the case with both phonon and magnon scattering. (b) Spectral heat flux from Co and Cu contacts. The dashed lines represents the case with pure phonon scattering and the solid lines represent the case with both phonon and magnon scatterings. The green color denotes the Cu contact and the cyan color denotes the Co contact. (c) Accumulation of heat flux normalized by the total heat flux.

NEGF method inherently treats the two contacts as infinite leads in the calculation of self energies.

3.4 Conclusion

In this work, we have developed a method that combines first-principles calculations, spin-lattice dynamics and the NEGF method to predict thermal boundary conductance with spin-lattice interactions across a heterogeneous Co-Cu interface. The magnetic moments and exchange constants in the Co layers next to the interface differ from those in bulk Co. The Cu layer adjacent to the interface is also slightly magnetized. However, the exchange interaction between Co and Cu layer is weak such that the magnetic wave incident from the Co side does not efficiently transmit across the interface. The magnons mainly interact with phonons inside the Co contact. The effects of spins on the movement of atoms are small. Both EMD and NEGF predicted a reduction of thermal boundary conductance in the presence of spins because the interface is a barrier to the transfer of magnetic energy.

The effect of spins at the Co-Cu interface is not significant, but the effect could be different for interfaces with stronger exchange interactions. Future work can be performed to find such heterogeneous structures in which spin-lattice interaction plays a more significant role.

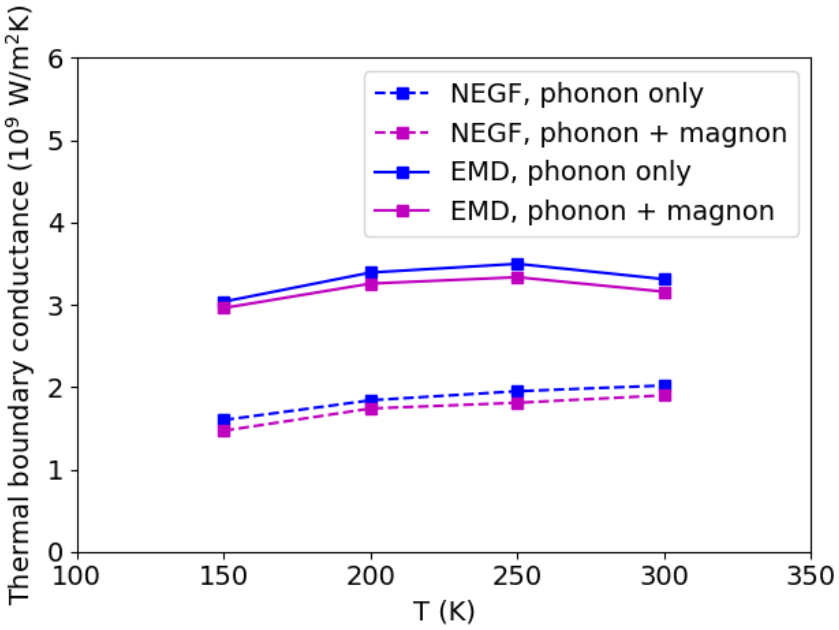

Figure 3.11: Comparison of thermal boundary conductance obtained from EMD and NEGF

CHAPTER 4

First-principles Calculations of the Optical Response of Single Layer and Bilayer Armchair Graphene Nanoribbons

4.1 Introduction

Electronic and optical properties of graphene nanoribbons depend on the precise atomic structures, and are tunable by varying widths and edges. Tunable bandgap and high mobility make graphene nanoribbons great candidates for a wide variety of optoelectronic applications.

Photodetectors made from graphene nanoribbon-based materials have shown ultra-high bandwidth and broadband light detection [99, 100, 101], and their photoresponsivity could be enhanced by utilizing the photogating effect [102] and introducing electron trapping centers to reduce the effect of carrier recombination [103]. Graphene nanoribbons have also been used in engineering photovoltaic devices. Xie et al. [104] reported a photoconversion efficiency of 1.47% by increasing the doping level in Schottky solar cells based on graphene nanoribbon/multiple silicon nanowires junctions, suggesting that graphene-based devices are promising candidates in fabricating solar cells due to their higher efficiency and easier production than devices based on silicon nanowires or silicon nanoribbons. Yang et al. [105] used graphene as 2D bridges in nanocrystalline electrodes of dye-sensitized solar cells and observed a 39% increase in photoconversion efficiency due to faster electron transport and lower recombination caused by the introduction of graphene. In the field of photocatalysis, graphene/semiconductor composites have received a lot of attention in recent years as the energy conversion and clean energy production are becoming more and more appealing to researchers. Chemically bonded P25-graphene nanocomposite photocatalyst was reported to increase the reaction rate significantly in the photodegradation process of methylene blue when

compared with bare P25 and P25-CNTs photocatalysts [106]. Li et al. [107] reported observing a highly efficient H_2 production from water with the CdS-cluster-decorated graphene nanosheets photocatalyst under visible light illumination. The high efficiency of H_2 production was attributed to graphene nanosheets that help collect and transport electrons generated by photoexcitation in the Cds clusters and therefore suppress the recombination of electron-hole pairs.

To better design graphene nanoribbon-based optoelectronics, an in-depth understanding of the electronic and optical properties of graphene nanoribbons is required. The recent development of bottom-up synthesis of structurally well-defined graphene nanoribbons [108] has advanced experimental investigations of optoelectronic properties of graphene nanoribbons. Experiments using different spectroscopy methods, including optical imaging and absorption spectroscopy, reflectance difference spectroscopy and energy- and angle-resolved two-photon photoemission spectroscopy [109, 110, 111], have shown that optical response of armchair graphene nanoribbons is dominated by excitons, the strongly correlated electron-hole pairs. The importance of excitonic effects in optical response of graphene nanoribbons is also confirmed by theoretic studies incorporating many-body effects [112, 113].

Previous studies are focused on single layer graphene nanoribbons and the optical properties of bilayer graphene nanoribbons are not well understood. It was reported that the interplay of nanoribbon's chirality and the inter-ribbon coupling could enhance terahertz and far infrared optical response in bilayer graphene nanoribbons with a 1D massless Dirac fermion energy dispersion near the Γ point [114]. The effect of π-stacking was investigated and found to widen the optical absorption range in bilayer graphene nanoflakes with homogeneous stacking and heterogeneous stacking [115].

Semiempirical models including tight-binding models [114, 116, 117] were mostly used in previous calculations of optical properties. In this work, we use first-principles methods to study the electronic and optical properties of single layer graphene nanoribbons and bilayer graphene nanoribbons with the α and β alignments. We also compare the optical properties of graphene nanoribbons from three different families.

4.2 Methods

Ground-state electronic properties are obtained by solving the mean-field Kohn-Sham equations within the mean-field density functional theory (DFT):

$$\left[-\frac{1}{2}\nabla^2 + V_{ext} + V_H + V_{xc}\right]\psi^{MF} = E^{MF}_{n\mathbf{k}}\,\psi^{MF}_{n\mathbf{k}} \tag{4.1}$$

where V_{ion} is the external potential associated with the nuclei, V_H is the Hartree potential, V_{xc} is the exchange-correlation potential that takes care of the anti-symmetric nature of electron wave functions and electron correlations, and $E^{MF}_{n\mathbf{k}}$ and $\psi^{MF}_{n\mathbf{k}}$ are the mean-field energies and mean-field wave functions respectively.

The Dyson equation is solved to compute quasi-particle eigenvalues and wave functions within the GW approximation:

$$\left[-\frac{1}{2}\nabla^2 + V_{ext} + V_H + \Sigma(E^{QP}_{nk})\right]\psi^{QP} = E^{QP}_{n\mathbf{k}}\,\psi^{QP}_{n\mathbf{k}} \tag{4.2}$$

where $\Sigma(E^{QP}_{n\mathbf{k}}) = iG_0W_0$ is the electron self-energy operator and the convolution of one-particle Green's function G_0 and screened Coulomb interaction W_0, $E^{QP}_{n\mathbf{k}}$ is the quasi-particle energies, and $\psi^{QP}_{n\mathbf{k}}$ is the quasi-particle wave functions.

Optical properties and excited states are calculated by solving the Bethe-Salpeter equation (BSE):

$$\left(E^{QP}_{c\mathbf{k}} - E^{QP}_{v\mathbf{k}}\right)A^S_{vc\mathbf{k}} + \sum_{v'c'\mathbf{k}'}\langle vc\mathbf{k}|\,K^{eh}\,|v'c'\mathbf{k}'\rangle = \Omega^S A^S_{vc\mathbf{k}} \tag{4.3}$$

where $E^{QP}_{c\mathbf{k}}$ and $E^{QP}_{v\mathbf{k}}$ are quasi-particle energies of the conduction and valence band states respectively, K^{eh} is the electron-hole interaction kernel, Ω^S is the excitation energy and $A^S_{vc\mathbf{k}}$ is the exciton amplitude.

The absorption spectra is proportional to the imaginary part of the macroscopic dielectric function. Within the independent-particle approximation which neglects the interaction between the

quasi-electron and quasi-hole, the imaginary part of the dielectric function is:

$$\varepsilon_2(\omega) \propto \sum_{vc\mathbf{k}} |\mathbf{e} \cdot \langle v\mathbf{k}| \mathbf{v} |c\mathbf{k}\rangle|^2 \delta\left(\omega - (E^{QP}_{c\mathbf{k}} - E^{QP}_{v\mathbf{k}})\right) \tag{4.4}$$

while with electron-hole interaction, the imaginary part of the dielectric function becomes:

$$\varepsilon_2(\omega) \propto \sum_{S} |\mathbf{e} \cdot \langle 0| \mathbf{v} |S\rangle|^2 \delta(\omega - \Omega_S) \tag{4.5}$$

where $\langle 0| \mathbf{v} |S\rangle = \sum_{vc\mathbf{k}} A^S_{vc\mathbf{k}} \langle v\mathbf{k}| \mathbf{v} |c\mathbf{k}\rangle$, $\mathbf{v}$ is the velocity operator and $\mathbf{e}$ is polarization of light.

The absorptivity is calculated as:

$$\alpha = \frac{4\pi k}{hc/E} \tag{4.6}$$

where k is the extinction index:

$$k(\omega) = \frac{1}{\sqrt{2}} \sqrt{-\varepsilon_1(\omega) + \sqrt{\varepsilon_1^2(\omega) + \varepsilon_2^2(\omega)}} \tag{4.7}$$

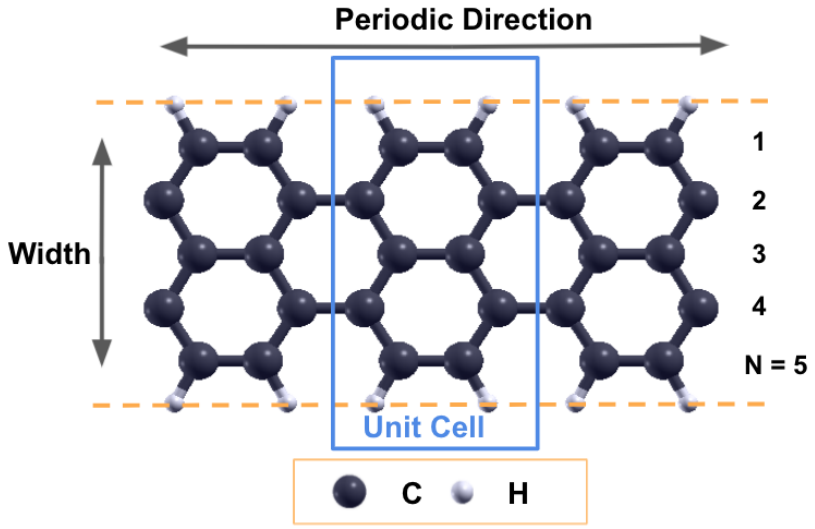

Figure 4.1: Schematic of 5-AGNR. Dashed lines represent the edges of graphene nanoribbons and the blue rectangle represents the unit cell used in simulations.

4.3 Results and discussion

4.3.1 Single layer graphene nanoribbons DFT and quasi-particle band structures

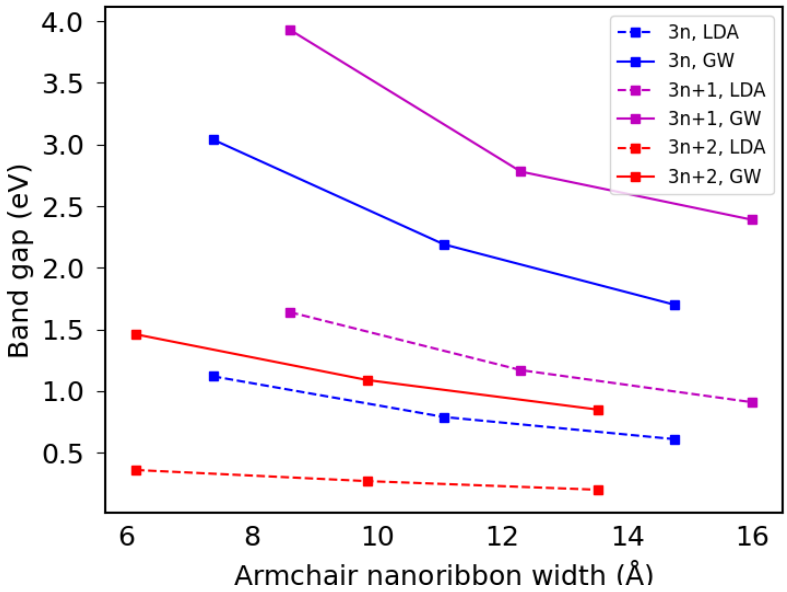

Figure 4.2: Comparison of band gaps of armchair graphene nanoribbons calculated from DFT-LDA and GW approximations. Dashed lines represent LDA calculations and solid lines represent GW calculations.

In this work, N-AGNR denotes the armchair graphene nanoribbon with N dimer lines along the width direction. The edges of the armchair graphene nanoribbons are passivated with hydrogen atoms. Figure 4.1 shows a schematic of the graphene nanoribbon with armchair edges and 5 dimer lines along the width (5-AGNR). The blue box demonstrates a unit cell used in DFT simulations and a 15 Å vacuum was placed in both the width direction and the out-of-plane direction to avoid interactions between repeated images.

The mean-field ground-state electronic structures were calculated using the Quantum Espresso [80] package. Full potentials were replaced by norm-conserving pseudopotentials with a 110 *Ry* cutoff to reduce the oscillation of wave functions and therefore the number of plane waves near the core. Exchange-correlation potentials were accounted for within the local density approximation (LDA) [118]. The atomic structures were fully relaxed using a $1 \times 1 \times 30$ k-grid until the energy

error between two consecutive self-consistent calculations is smaller than 10^{-12} *Ry*.

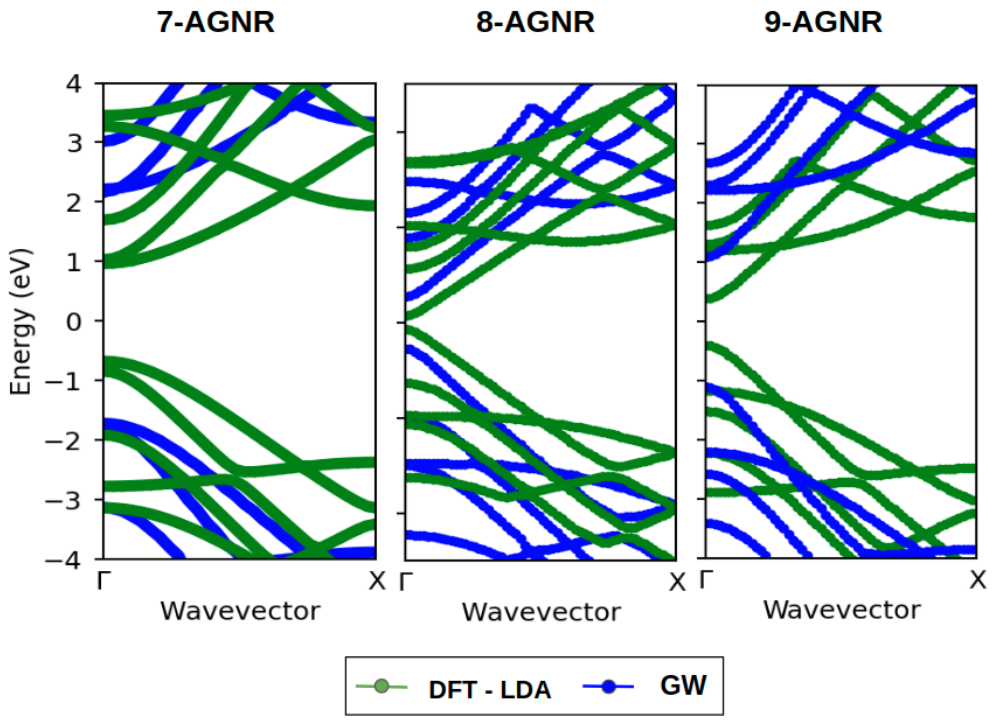

Figure 4.3: Band structures of 7-AGNR ($3n+1$), 8-AGNR ($3n+2$) and 9-AGNR ($3n$). Green lines represent band structures calculated within the LDA approximation and blue lines represents band structures calculated within the GW approximation.

GW calculations were conducted using the BerkeleyGW [119] package. The dielectric matrix and self-energy $\Sigma(E^{QP}_{n\mathbf{k}})$ were calculated with a 10 *Ry* energy cutoff and a summation over 200 bands on a $1 \times 1 \times 30$ k-grid. The 1D cell-wire truncation scheme was used to reduce the long-range Coulomb interactions and to accelerate convergence with respect to the k-mesh.

Three families of armchair graphene nanoribbons were investigated in current work: $3n$, $3n+1$ and $3n+2$ where n is an integer number. Fig. 4.2 shows the band gaps of armchair graphene nanoribbons of widths within the range of 6 Å to 16 Å calculated within the DFT-LDA approximation and within the GW approximation, respectively. While the GW approximation increases the band gaps for all 3 families considered, the inclusion of many-body interactions has a more significant effect on $3n$ and $3n+1$ families graphene nanoribbons. As the width increases, the band gap decreases and the difference between DFT-LDA and GW calculations also decreases. The band gap will eventually go to zero when the width of the graphene nanoribbon becomes infinite. For

a fixed n number, e.g., when $n = 2$, the band gap of the $3n+2$ family (8-AGNR, middle points on the red curves) is the smallest, and that of the $3n+1$ family (7-AGNR, left-most points on the magenta curves) is the largest.

Fig. 4.3 demonstrates a comparison of band structures along the high symmetry line $\Gamma - X$ calculated from DFT and GW approches for 7-AGNR, 8-AGNR and 9-AGNR. The shapes of the band structures obtained within the DFT approximation and GW approximation are similar but GW approximation enlarges the band gaps for all 3 families and the increase is the most significant for 7-AGNR.

4.3.2 Single layer graphene nanoribbons optical response calculations

Optical response was obtained by solving the Bethe-Salpeter equation (BSE) on a dense k-grid but the computation of the interaction kernel (the second term in Eq. 4.3) is very expensive; therefore an interpolation technique was used to get converged results of the absorption spectra with feasible computational cost. The interaction kernel and quasi-particle electron energy were first computed on a coarse k-grid ($1 \times 1 \times 30$). By expanding the fine k-grid ($1 \times 1 \times 60$) wave functions in terms of the coarse k-grid wave functions, both the quasi-particle energy and kernel matrix elements were interpolated onto the fine k-grid. After constructing the effective Hamiltonian, Eq. 4.3 was then diagonalized to obtain the excitation energy and the exciton amplitude.

Figure 4.4 plots the imaginary and the real part of the dielectric function of armchair single layer graphene nanoribbons from three families: the $3n+1$ family (Fig. 4.4(a)-(b)), the $3n$ family (Fig. 4.4(c)-(d)) and the $3n+2$ family (Fig. 4.4(e)-(f)). The increase of width makes the ε_1 and ε_2 peaks shift to lower photon energies. For a fixed n number, the $3n+2$ family has the smallest incident energies for the peaks in the dielectric functions and the $3n+1$ family has the largest incident energies for the peaks, consistent with the band gaps observed in Fig. 4.2.

In the energy range of 0 to 4 eV, the most dominant peak in the optical absorption spectra (the imaginary part of the dielectric function ε_2) is $E_{1,1}$ for the $3n$ and $3n+2$ families. For the $3n+1$ family, two prominent absorption peaks exist within the energy range of interest: $E_{1,1}$ and $E_{2,2}$. $E_{1,1}$ represents an excitation from the highest valence band to the lowest conduction

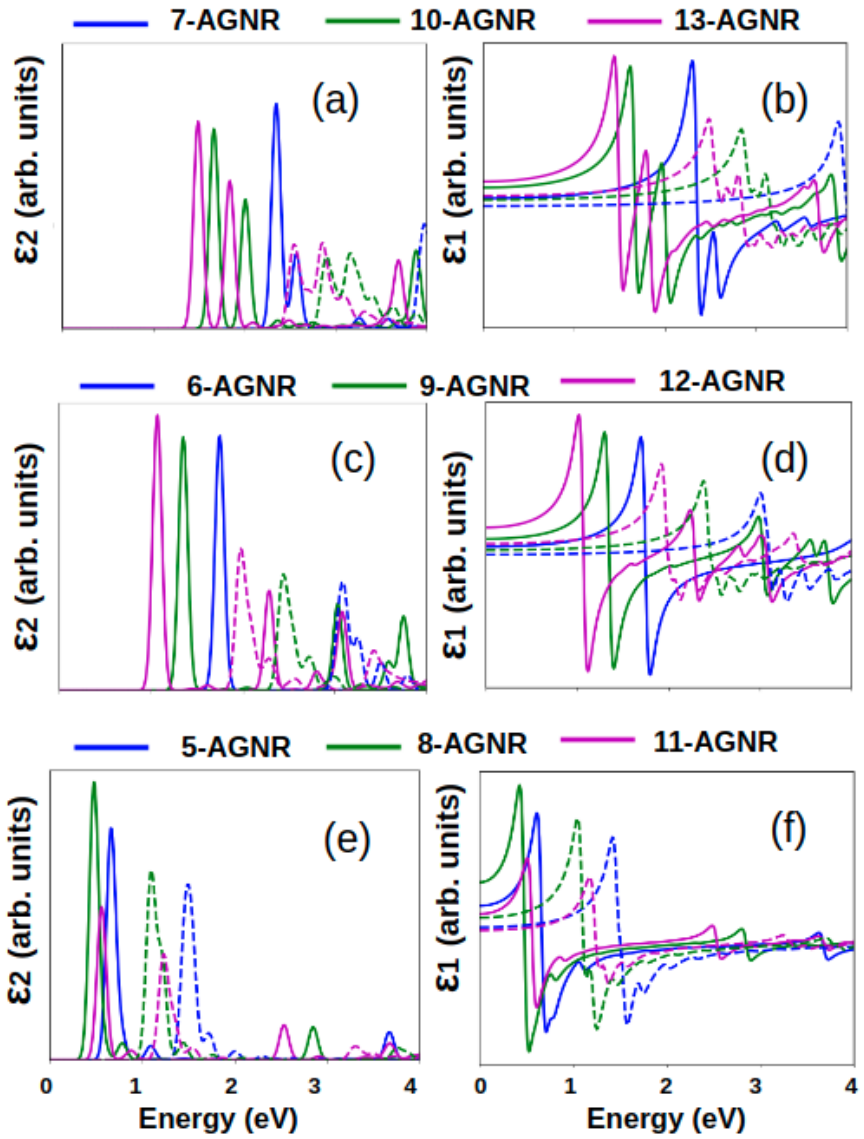

Figure 4.4: Imaginary and real part of dielectric function of armchair graphene nanoribbons calculated within the GW-BSE and GW-RPA approximations. Imaginary and real part of dielectric function for (a)-(b) $3n+1$ family, (c)-(d) $3n$ family and (e)-(f) $3n+2$ family. Solid lines represent absorption spectra obtained from GW+BSE calculations and dashed lines represent absorption spectra obtained from GW+RPA calculations.

band and $E_{2,2}$ represents an excitation from the second highest valence band to the second lowest conduction band. The inclusion of the electron-hole interaction in the calculation of the dielectric function significantly shifts the peaks to the low energy range. The $3n+1$ family experiences the largest effect of the electron-hole interaction while the $3n+2$ family experiences the smallest effect, displaying a similar trend as the band gaps and the incident energies.

Fig. 4.5 shows the relationship between absorption peaks in the absorption spectra and the corresponding vertical interband transitions in the quasi-particle band structure for 7-AGNR, a representative of the $3n+1$ family. The energy of the electron-hole quasi-particle is smaller than an unbound electron-hole pair due to the interaction between the electron and the hole which is essentially the Coulomb force; therefore the incident energy required in the optical absorption spectra is smaller than the electronic band gap. In Fig. 4.5, the $E_{1,1}$ exciton forms at the incident photon energy of 2.35 eV while the electronic band gap is 3.93 eV. The difference between the electronic band gap and the optical band gap, also known as the exciton binding energy, is listed in Table 4.1. $E_{b,1}$ is the binding energy corresponding to the $E_{1,1}$ excitation and $E_{b,2}$ is the binding energy corresponding to the $E_{2,2}$ excitation.

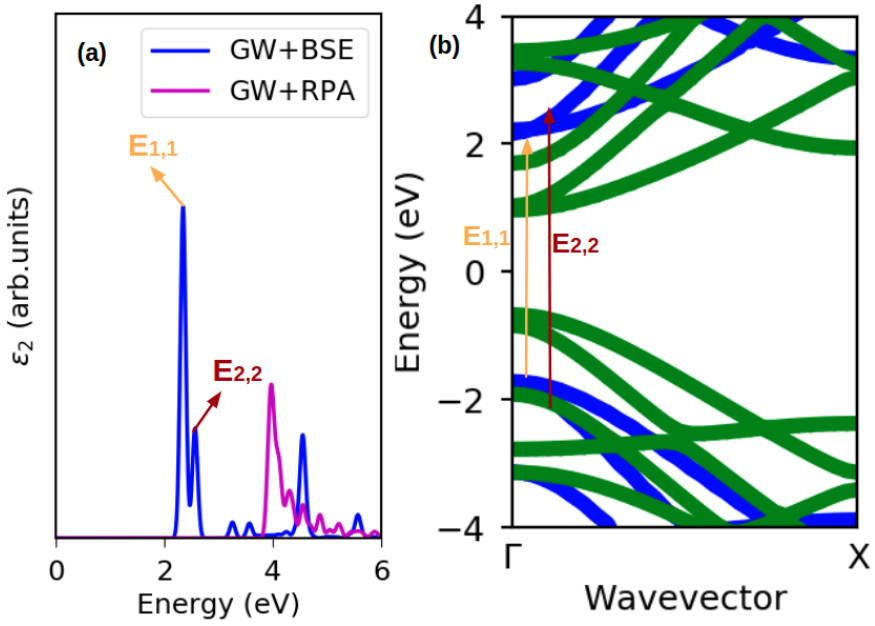

Figure 4.5: Excitations in 7-AGNR. (a) Absorption spectra of 7-AGNR. (b) GW band structure of 7-AGNR. $E_{1,1}$ is the excitation from highest valence band to lowest conduction band and $E_{2,2}$ is the excitation from second highest valence band to second lowest conduction band.

The $E_{1,1}$ exciton wavefunctions in the $3n+1$ (7-AGNR), $3n+2$ (8-AGNR) and $3n$ (9-AGNR) families are shown in Fig. 4.6 with the blue dots denoting positions of holes. The excition wavefunctions are Wannier-like and extend fully in the width direction. The exciton wavefunction for the $3n+2$ family is the most delocalized. Because of the most π-conjugation, the band gap (Fig. 4.2), onset energy in the absorption spectra (Fig. 4.4) and the binding energy (Table 4.1) of the $3n+2$ family armchair graphene nanoribbons are the smallest.

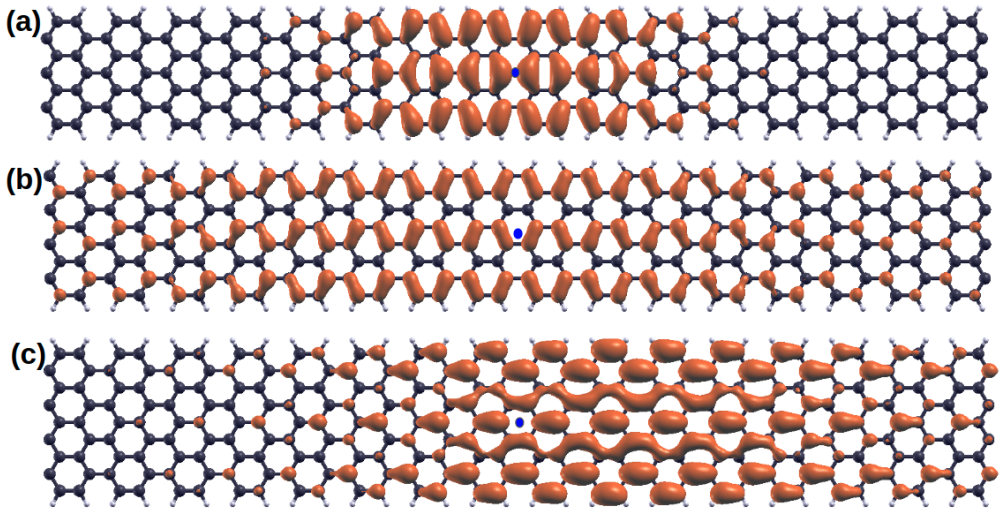

Figure 4.6: Exciton wavefunctions. (a) $E_{1,1}$ exciton wavefunctions for 7-AGNR. (b) $E_{1,1}$ exciton wavefunctions for 8-AGNR. (c) $E_{1,1}$ exciton wavefunctions for 9-AGNR.

	5-AGNR	6-AGNR	7-AGNR
$E_{b,1}$ (eV)	1.06	1.29	1.58
$E_{b,2}$ (eV)	1.01	1.98	1.36
	8-AGNR	9-AGNR	10-AGNR
$E_{b,1}$ (eV)	0.61	1.12	1.23
$E_{b,2}$ (eV)	0.88	1.41	1.18
	11-AGNR	12-AGNR	13-AGNR
$E_{b,1}$ (eV)	0.73	0.95	1.06
$E_{b,2}$ (eV)	0.78	1.18	1.05

Table 4.1: Exciton binding energy

Figure 4.7 plots the absorptivity of single layer armchair graphene nanoribbons along the ribbon axis for the $3n$, $3n+1$ and $3n+2$ families. Increasing the nanoribbon width causes a red shift in incident photon energies and the shift due to the width increase is the most significant for the

$3n$ family. The absorptivity spectrum has a similar shape as the imaginary part of the dielectric function as indicated by Fig. 4.4.

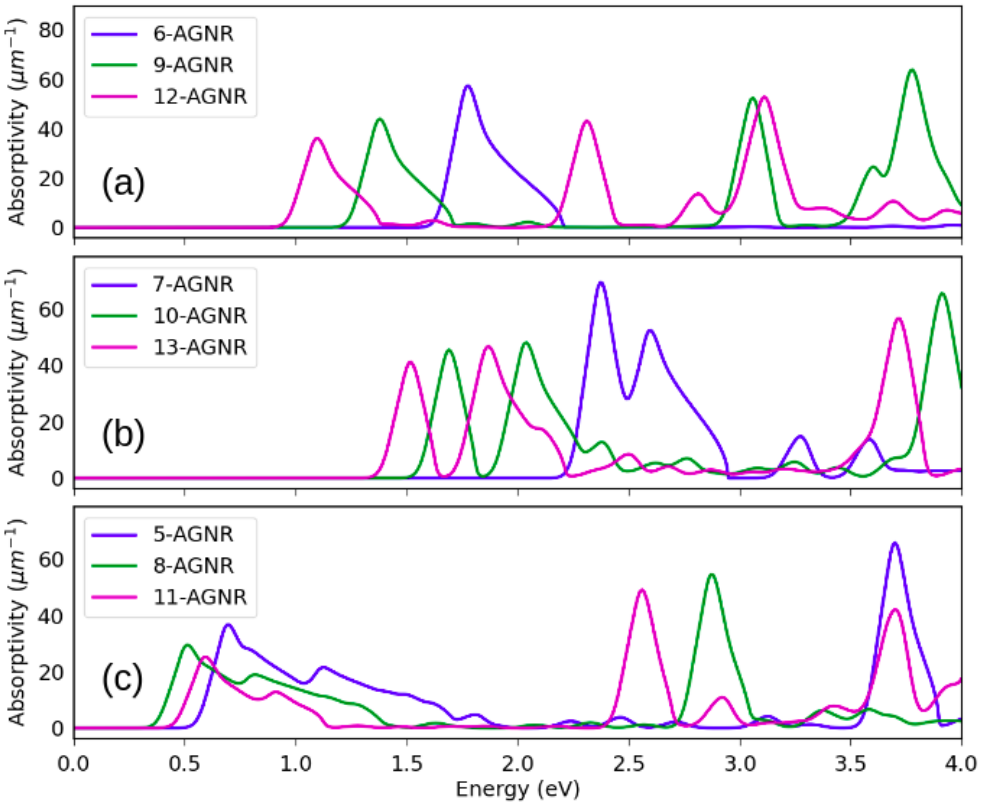

Figure 4.7: Absorptivity of single layer armchair graphene nanoribbons. (a) Absorptivity of the $3n$ family nanoribbons. (b) Absorptivity of the $3n+1$ family nanoribbons. (c) Absorptivity of the $3n+2$ family nanoribbons.

4.3.3 Bilayer graphene nanoribbons bandstructure calculations

In this work, we consider two different alignments of Bernal stacked bilayer graphene: the α alignment and the β alignment as shown in Fig. 4.8. In the α alignment, one layer of graphene nanoribbon is shifted along the ribbon axis (periodic direction) with the edges aligned with the other layer while in the β alignment one layer of graphene nanoribbon is shifted along both the ribbon axis and the width direction.

We have calcuated the electronic structures of bilayer 5-AGNR, 6-AGNR and 7-AGNR for both the α and β alignments, within the GW approximation. Figure 4.9 shows the comparison

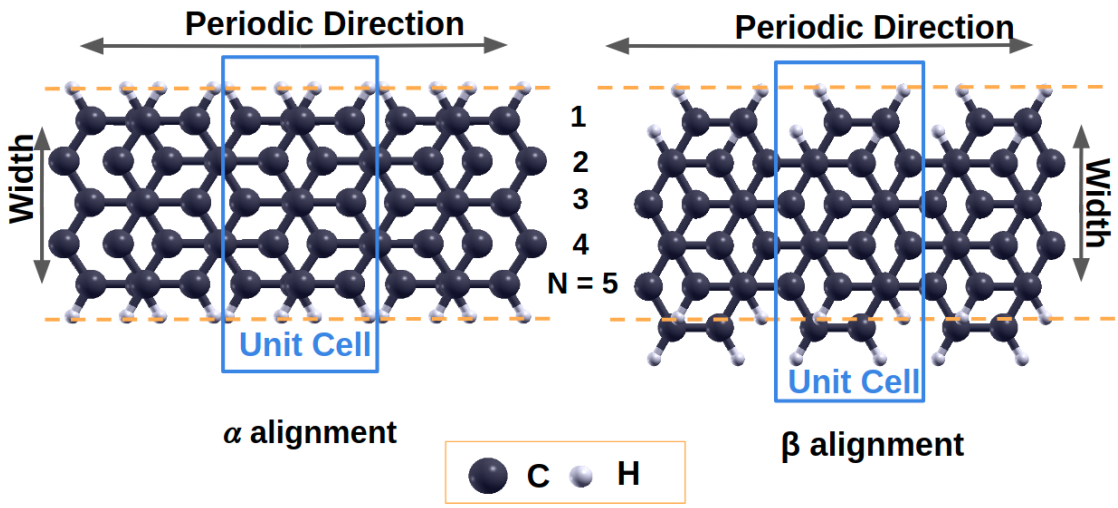

Figure 4.8: Bilayer armchair graphene nanoribbons α and β alignments

of band gaps of single layer and bilayer graphene nanoribbons. Single layer armchair graphene nanoribbons have the largest band gaps compared with its bilayer conterparts and the bilayer α alignment nanoribbons have the smallest band gaps for all three families. The difference in band gaps for the bilayer α and β alignments decreases with width and the difference becomes negligible as the width goes into infinity because the nanoribbons in both alignments become Bernal-stacked bilayer graphene.

4.3.4 Bilayer graphene nanoribbons optical response calculations

The dielectric functions within the GW+BSE approximation for the single layer, the bilayer α alignment and the bilayer β alignment configurations are shown in Fig. 4.10. For all three families considered, the single layer armchair graphene nanoribbons have the highest onset absorption energy. Adding an extra layer of graphene nanoribbon shifts the absorption peaks to lower photon energies.

Not only the energy peaks shift to lower energies, the shapes of the absorption curves also differ from those of the single layer graphene nanoribbons. More oscillations and peaks occur in the dielectric functions of bilayer graphene nanoribbons than single layer nanoribbons. The bilayer α alignment nanoribbons have lower onset absorption energies than the β alignment nanoribbons.

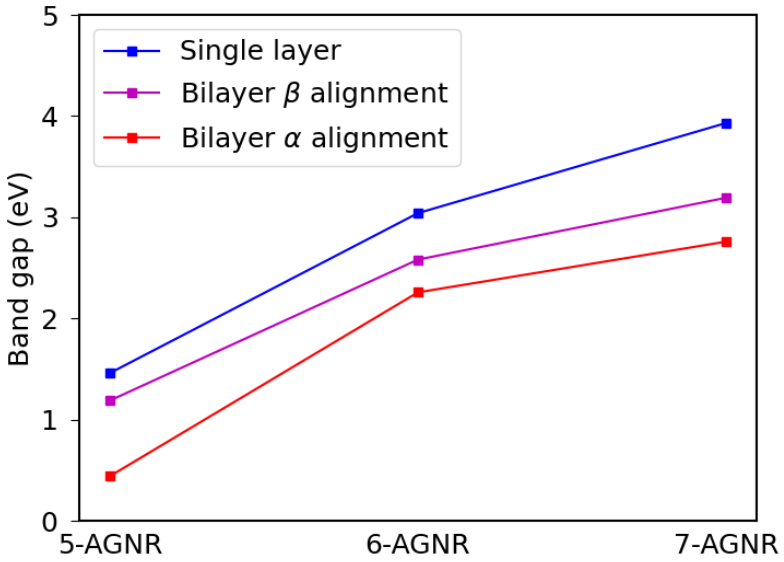

Figure 4.9: Comparison of band gaps of single layer, bilayer α and bilayer β armchair graphene nanoribbons

The difference in the dielectric functions between the α alignment and the β alignment nanoribbons is larger for 5-AGNR (Fig. 4.10(a)-(b)) than for 6-AGNR (Fig. 4.10(c)-(d)) and 7-AGNR (Fig. 4.10 (e)-(f)), agreeing with the trend of band gaps shown in Fig. 4.9. For 5-AGNR, the onset energy of the bilayer β alignment is closer to the onset energy of the single layer configuration instead of the α alignment, as shown in Fig. 4.10(a) and Fig. 4.10(b).

The calculated absorptivities of the single layer, the bilayer α and the bilayer β armchair graphene nanoribbons (Fig. 4.11) display a similar trend as the band gaps and dielectric functions predicted in Fig. 4.9 and Fig. 4.10. The bilayer α alignment has the lowest photon incident energy and the single layer configuration has the highest photon incident energy. The trend observed in the single layer armchair graphene nanoribbons that the $3n+2$ family nanoribbons have the lowest band gaps and onset absorption energies while the $3n+1$ family nanoribbons have the highest band gaps and onset absorption energies is preserved in bilayer graphene nanoribbons and is not affected by the number of layers or the way of alignments between layers.

The $E_{1,1}$ exciton wavefunctions for the single layer, the bilayer α alignment and the bilayer β alignment 7-AGNR are shown in Fig. 4.12. The exciton wavefunction in the single layer configu-

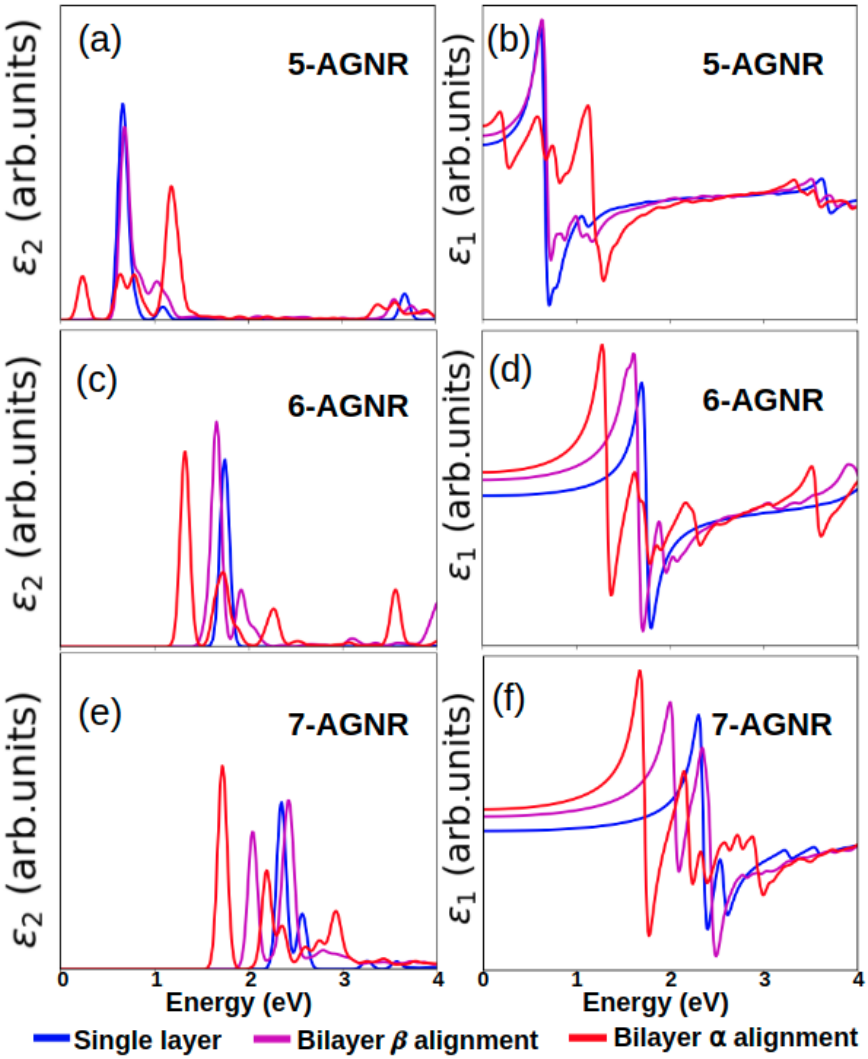

Figure 4.10: Comparison of the imaginary and the real parts of dielectric functions of single layer, bilayer α alignment and bilayer β alignment armchair graphene nanoribbons. Imaginary and real part of the dielectric function for (a)-(b) 5-AGNR, (c)-(d) 6-AGNR and (e)-(f) 7-AGNR. Blue lines denote single layer nanoribbons, magenta lines denote bilayer β alignment nanoribbons, and red lines denote bilayer α alignment nanoribbons.

ration is the most localized and the electrons are distributed around the atoms near the hole region, as is shown in Fig. 4.12(a). The exciton wavefuntion in the bilayer α alignment 7-AGNR extends the most along the ribbon axis as shown in Fig. 4.12(b), resulting in the smallest band gaps and onset photon energies compared with the single layer configuration and the bilayer β alignment.

4.4 Conclusions

In this work, we have conducted optical response calculations on single layer armchair graphene nanoribbons of different widths from three families: the $3n$, $3n+1$ and $3n+2$ families. Increasing the width of nanoribbons from any family decreases band gaps and causes a redshift in the dielectric functions and the absorptivity spectra. A comparison of exciton wavefunctions in the representatives (7-AGNR, 8-AGNR and 9-AGNR) of graphene nanoribbons from three families has shown that the $3n+2$ family has the most delocalized electron distributions with fixed hole positions and the most π-conjugation has resulted in the smallest band gaps and lowest onset photon absorption energies among the three families.

We have also compared the optical response of the single layer armchair graphene nanoribbons to bilayer armchair graphene nanoribbons of α and β alignments. Band gaps and onset photon absorption energies are reduced in the bilayer configuration and the reduction is more significant for the α alignment nanoribbons. The difference between the α and β alignment gets smaller as the nanoribbon width increases.

The optical response in graphene nanoribbons greatly depends on the details of the nanoribbons structures. By varying the width, number of layers and the edge alignment, the absorption spectra could be tuned.

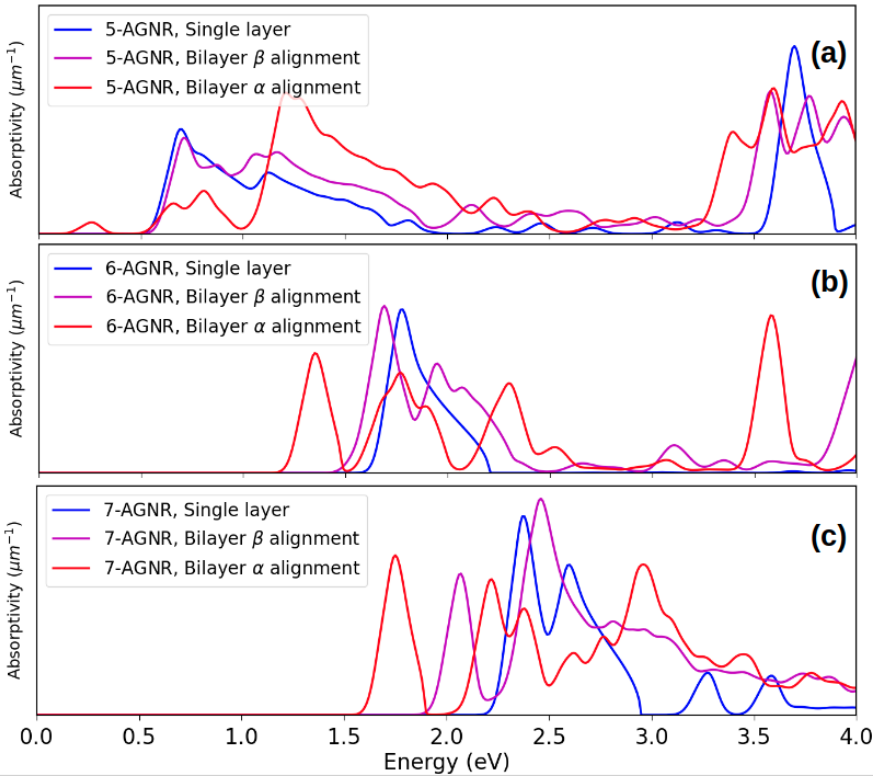

Figure 4.11: Comparison of absorptivities of single layer, bilayer α and bilayer β armchair graphene nanoribbons. (a) Absorptivities of 5-AGNR. (b) Absorptivities of 6-AGNR. (c) Absorptivities of 7-AGNR.

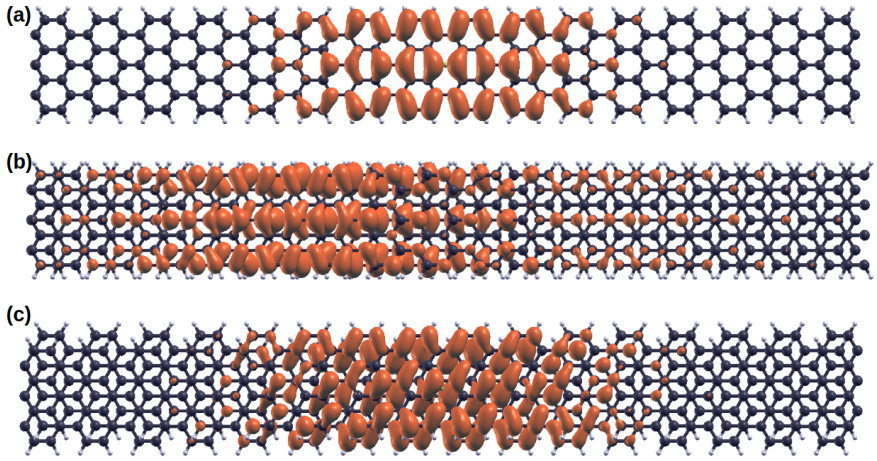

Figure 4.12: Comparison of $E_{1,1}$ exciton wavefunctions in single layer, bilayer α and bilayer β 7-AGNR. (a) $E_{1,1}$ exciton wavefunction in single layer 7-AGNR. (b) $E_{1,1}$ exciton wavefunction in bilayer α 7-AGNR. (c) $E_{1,1}$ exciton wavefunction in bilayer β 7-AGNR.

CHAPTER 5

Photo-thermal Effect in Methane Decomposition

5.1 Introduction

Photocatalysts utilize light to drive chemical reactions. Among photocatalysts, plasmonic nanoparticles are able to harvest visible and near-infrared energies due to the localized surface plasmon resonance induced by incident light. Electron-hole pairs are generated from plasmon decay and the hot electrons are injected into the anti-bonding electronic state of reactant molecules, creating transient negative ions which move on the potential energy surface of the excited states and facilitate further chemical reactions. Plasmon-mediated enhancement of photocatalytic rate was reported in a H_2 dissociation reaction on gold nanoparticles supported on a TiO_2 substrate [120]. The authors found that the photocatalytic rate strongly depends on the concentration and size of gold nanoparticles, and attributed the negligible reactivity rate for gold nanoparticles of diameters greater than 21 nm to less plasmon confinement and more electron-electron scattering. It was also reported that the photocatalytic effect induces a 5-fold increase of reactivity rate at low temperatures compared to thermal effect only. While plasmonic metals can harvest a wider range of solar energy than semiconductors which require higher energy excitations to overcome the band gap and generate electron-hole pairs, the lifetime of hot carriers are short compared to the time scale of chemical reactions. The metal-semiconductor heterostructure has gained a lot of interest in the field of photocatalysis due to its ability to separate and retain electrons. The Schottky barrier at the metal and semiconductor interface prevents electrons in the semiconductor conduction band to transfer back to the metal, thus reducing carrier recombination and increasing carrier lifetime. Costi et al. [121] reported charge retention in hybrid gold-tipped CdSe nanorods under visible light radiation. The solution of gold-tipped CdSe nanorods was pre-irradiated and then mixed with

methylene blue. The authors observed a diminishment of the double peak absorbance feature as methylene blue was transformed to leucomethylene blue, and the decrease in the peaks was more significant for longer pre-irradiation times. A comparison experiment using a pre-irradiated mixture solution of CdSe nanorods and gold nanoparticles showed 13% reduction of methylene blue while the hybrid gold-tipped CdSe nanorods showed 64% reduction of methylene blue under same conditions, proving that the hybrid gold-tipped CdSe nanorods are efficient in retaining electrons.

Hot carriers are generated by photoexcitation at the time scale of less than 100 fs and relaxed through inelastic electron-electron scattering within 100 fs to 1 ps. Electrons in the metal further interact with phonons and transfer energy to the lattice within 1 ps to 10 ps, causing a local thermal effect called photo-thermal effect. It is of great importance to untangle the contribution from the thermal effect and the hot-carrier effect in photocatalysis. Robatjazi et al. [122] investigated photocatalytic CO_2 conversion on $Al-CuO_2$ antenna-reactor nanoparticles and observed a significant temperature increase of 110 K at steady state in the presence of $Al-CuO_2$, confirming photothermal heating. A comparison between the light-induced and thermally driven CO_2 conversion showed that the products in the light-driven reactions are more selective. Additionally, the steady-state temperature in light-driven reactions is lower than the onset temperature in thermal-driven reactions, suggesting a dominant hot-carrier effect over the thermal effect. By measuring the top and bottom surface temperatures on the catalyst bed, Zhang et al. [123] extracted the effective thermal and nonthermal reaction rates in the CO_2 methanation reaction catalyzed by Rh nanoparticles supported on TiO_2. The non-thermal effect was found to contribute to the total reaction rate superlinearly with the light intensity and became more pronounced at high temperatures.

In this work, we investigate the photo-thermal effects in the methane decomposition that produces high-value graphitic carbon and hydrogen gas under irradiation from a solar reactor and simulator. The experimental setup is shown in Fig. 5.1

We model the electronic transitions and absorption of possible intermediate polycyclic aromatic hydrocarbon (PAH) products. Further, we calculate the heat capacity of PAH and evaluate the temperature rise.

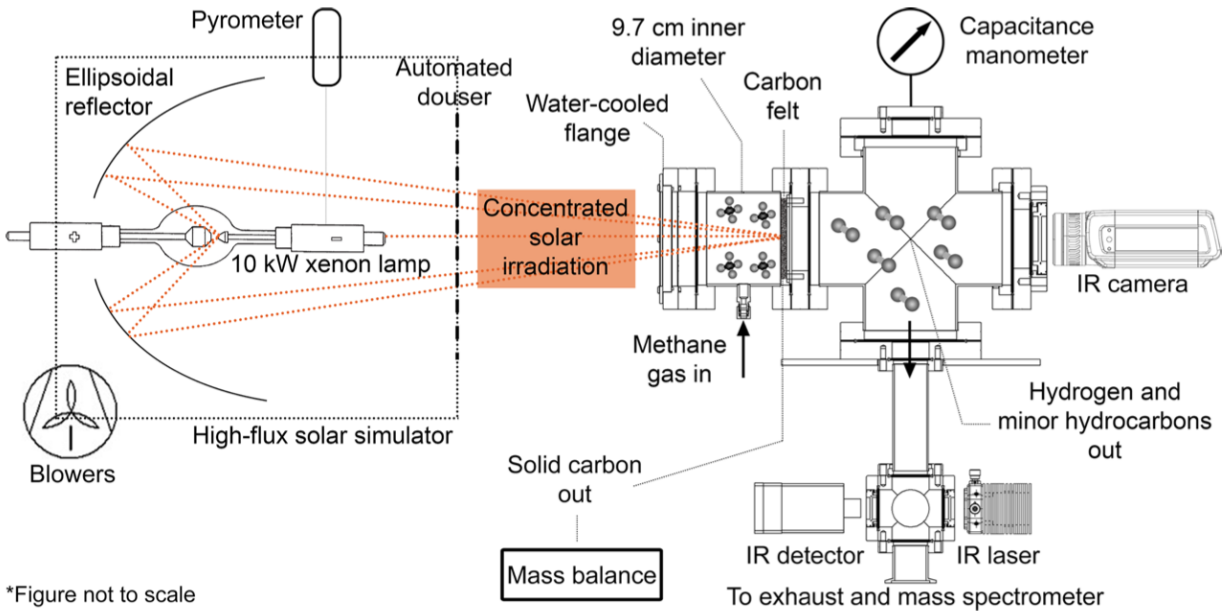

Figure 5.1: Experimental setup of methane decomposition (ref. [124])

5.2 Methods

5.2.1 Electronic transitions and absorption coefficient

Electronic transitions in PAH are computed using TD-DFT implemented in the Q-Chem package. Structure relaxation and excitation energies are calculated with the B3LYP functional.

The absorption coefficient is assumed to be a Gaussian shape function:

$$\varepsilon_i(\nu) = \varepsilon_i^{max}\, exp\Big[-\Big(\frac{\nu-\nu_i}{\sigma}\Big)^2\Big] \tag{5.1}$$

where ν_i is the energy of excitation i, ε_i^{max} is the energy when the incident photon energy ν is equal to the electronic excitation energy ν_i, and σ is the half-width of the Gaussian function. ε_i^{max} is related to the dipole strength D_i via

$$D_i = 4\Big[\frac{3\cdot 1000\; ln(10)\; h\; c}{32\;\pi^3\; N_A}\Big]\;\varepsilon_i^{max}\sqrt{\pi}\;\frac{\sigma}{\nu_i} \tag{5.2}$$

where h is Planck's constant, c is the speed of light and N_A is Avogadro's number. The dipole

strength is related to the dimensionless oscillator strength via

$$f_i = \frac{8\ \pi^2\ \nu_i\ m_e\ c}{3\ h\ e^2}\ D_i \tag{5.3}$$

where m_e is the electron mass and e is the electron charge.

Combining Eq. 5.2 and Eq. 5.3, Eq. 5.1 becomes

$$\varepsilon_i(\nu) = \frac{\sqrt{\pi}\ e^2\ N_A}{1000\ ln(10)\ c^2\ m_e}\ \frac{f_i}{\sigma}\ exp\Big[-\Big(\frac{\nu-\nu_i}{\sigma}\Big)^2\Big] \tag{5.4}$$

and the total molar absorption coefficient contributed by all the electronic excitations is the sum of individual coefficients:

$$\varepsilon(\nu) = \sum_i \varepsilon_i(\nu) \tag{5.5}$$

5.2.2 Specific heat

The internal energy E is related to the partition function q via

$$E = N_A\ k_B\ T^2 \Big(\frac{\partial lnq}{\partial T}\Big)_V \tag{5.6}$$

where k_B is the Boltzmann constant. The constant volume specific heat is the amount of energy required to raise the temperature by one unit:

$$C_v = \Big(\frac{\partial E}{\partial T}\Big)_{N,V}. \tag{5.7}$$

The partition function of the translational component reads

$$q_t = \Big(\frac{2\ \pi\ m\ k_B\ T}{h^2}\Big)^{3/2}\ V, \tag{5.8}$$

the partition function of the rotational component of nonlinear polyatomic molecules is

$$q_r = \frac{\pi^{1/2}}{\sigma_r} \frac{T^{3/2}}{(\Theta_{r,x}\,\Theta_{r,y}\,\Theta_{r,z})^{1/2}} \tag{5.9}$$

where σ_r is the symmetry number and $\Theta_{r,x(y,z)}$ is the rotational temperature associated with moment of inertia about the $x(y,z)$ axis, and the partition function of the vibrational component is

$$q_v = \prod_i \frac{e^{-\Theta_{v,i}/2T}}{1 - e^{-\Theta_{v,i}/T}} \tag{5.10}$$

where i is the index of the vibrational mode and $\Theta_{v,i} = h\nu_i/k_B$ is the vibrational temperature and ν_i is the vibrational frequency of the vibrational mode i.

Inserting Eq. 5.8, 5.9 and 5.10 into Eq. 5.6 and 5.7, we obtain specific heats from translational, rotational and vibrational components as follows:

$$C_{V,t} = \frac{3}{2} R \tag{5.11}$$

$$C_{V,r} = \frac{3}{2} R \tag{5.12}$$

$$C_{V,v} = R \sum_i e^{-\Theta_{v,i}/T} \left(\frac{\Theta_{v,i}/T}{e^{-\Theta_{v,i}/T} - 1} \right)^2 \tag{5.13}$$

5.3 Results and discussion

In this work, we consider four PAHs: Pyrene $C_{16}H_{10}$, Coronene $C_{24}H_{12}$, Ovalene $C_{32}H_{14}$ and Circumpyrene $C_{42}H_{16}$. Figure 5.2 shows the electronic transitions calculated by TD-DFT. The long wavelength excitations increase with the number of carbon rings. The smallest energy excitation shifts to long wavelengths with the size of the PAH molecule because the smallest energy excitation is mostly contributed by the HOMO-LUMO transitions, and as the number of carbon rings increases the HOMO-LUMO gap decreases due to more π-conjugation.

Molar absorption coefficients in PAHs are calculated according to Eq. 5.4 and 5.5 as shown in Fig. 5.3. The range of absorption becomes broader as the size of the PAH molecule increases.

By mapping the absorption coefficient to the light intensity profile in the experiment indicated in Fig. 5.4, spectral absorption and accumulated absorption are obtained, as shown in Fig. 5.5. The absorption in the visible light range grows with the number of carbon rings in PAH. The cutoff frequency of Pyrene is about 450 nm while the cutoff frequency of Circumpyrene is almost 750 nm. By varying the size of PAH molecules, the absorption spectra could be tuned.

The intensity of vibrational modes increase with the PAH size. More vibrational modes between 500 cm^{-1} to 1500 cm^{-1} appear as the size of PAH grows, causing a rise in heat capacity shown in Fig. 5.7. The calculated temperature dependent heat capacity is compared with reference [125].

5.4 Summary

In order to better understand the experimentally observed conversion rate in methane decomposition under solar light irradiation and to investigate photo-thermal effect, we use TD-DFT to calculate electronic transitions and molar absorption coefficients of four PAH molecules. Vibrational transitions and specific heats are also computed to estimate the temperature rise of PAH molecules under irradiation.

Future work could be direct modeling of chemical reactions of PAHs under irradiation and separating photo-driven effect from thermal-driven effect.

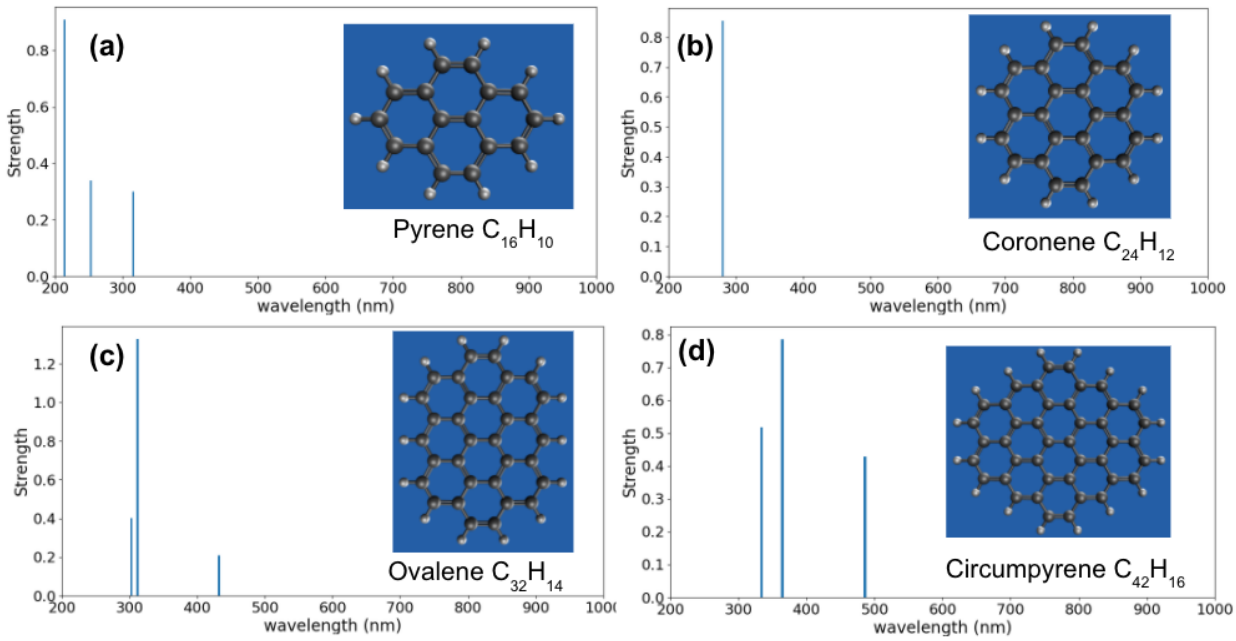

Figure 5.2: Electronic transitions in (a) Pyrene, (b) Coronene, (c) Ovalene and (d) Circumpyrene.

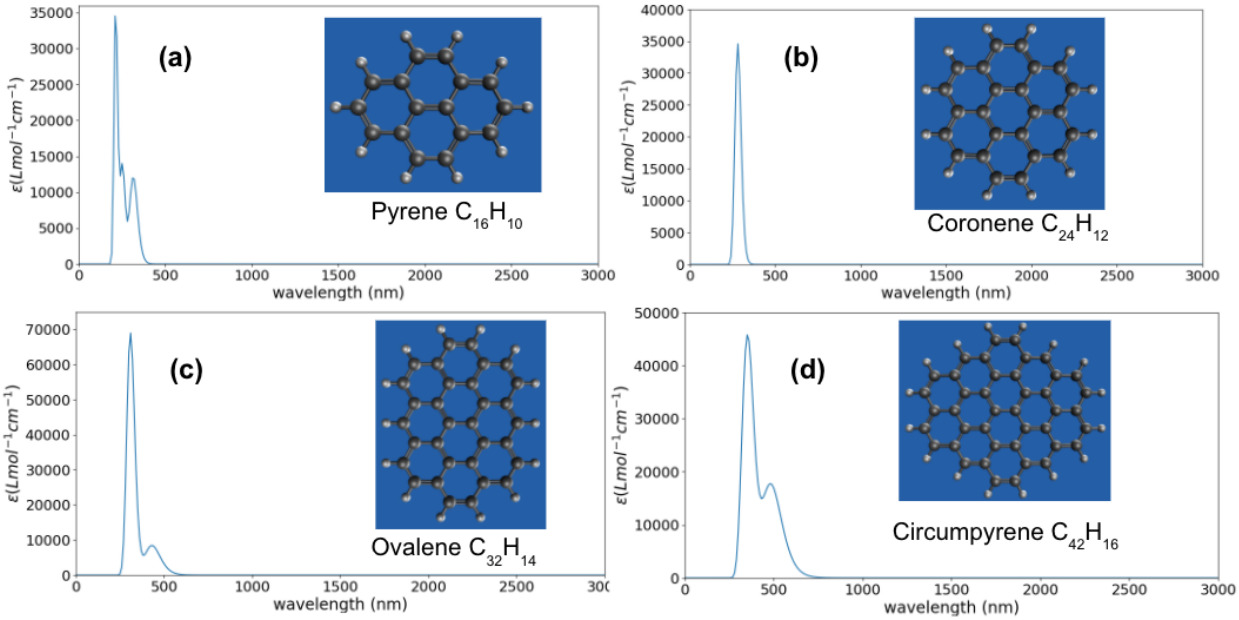

Figure 5.3: Molar absorption coefficient of (a) Pyrene, (b) Coronene, (c) Ovalene and (d) Circumpyrene.

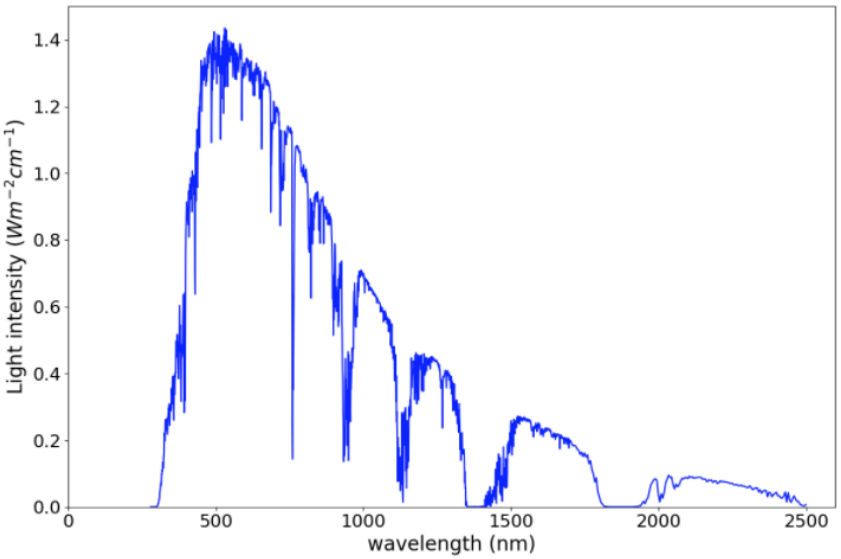

Figure 5.4: Light intensity profile

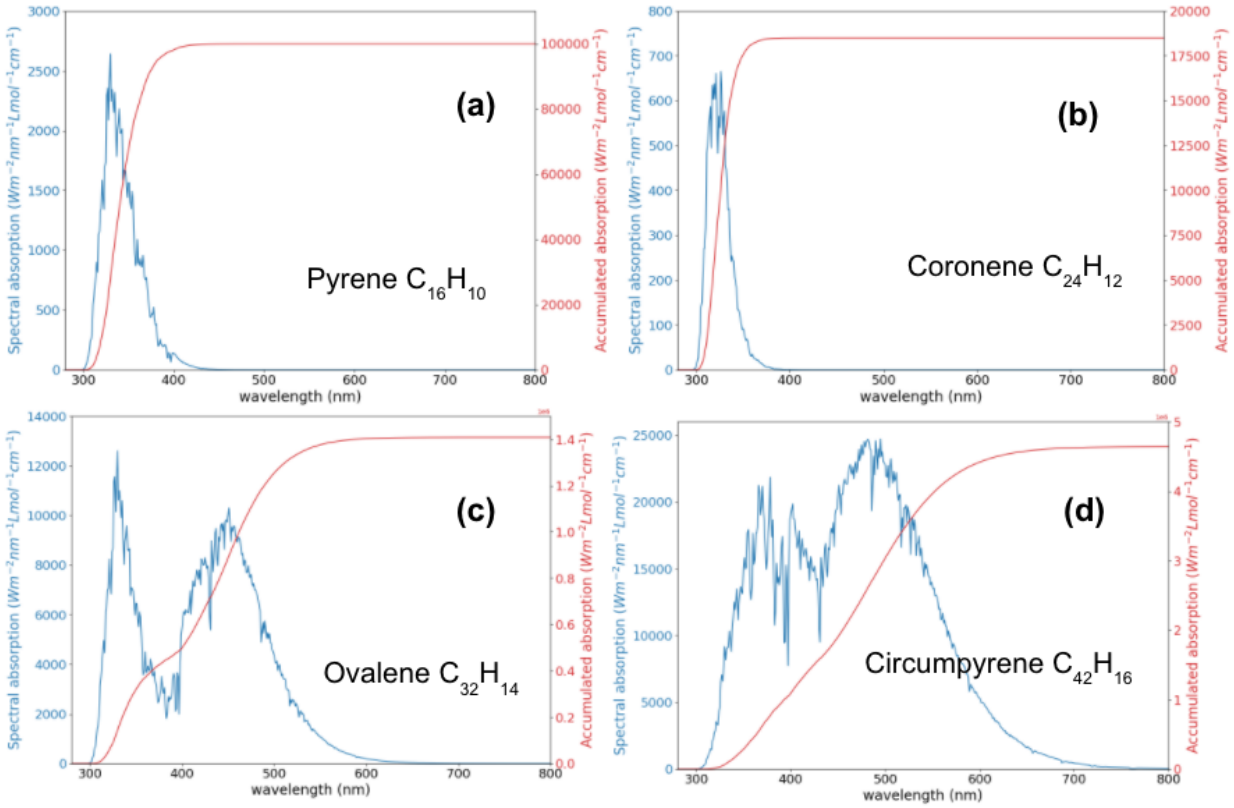

Figure 5.5: Spectral and accumulated absorption of (a) Pyrene, (b) Coronene, (c) Ovalene and (d) Circumpyrene.

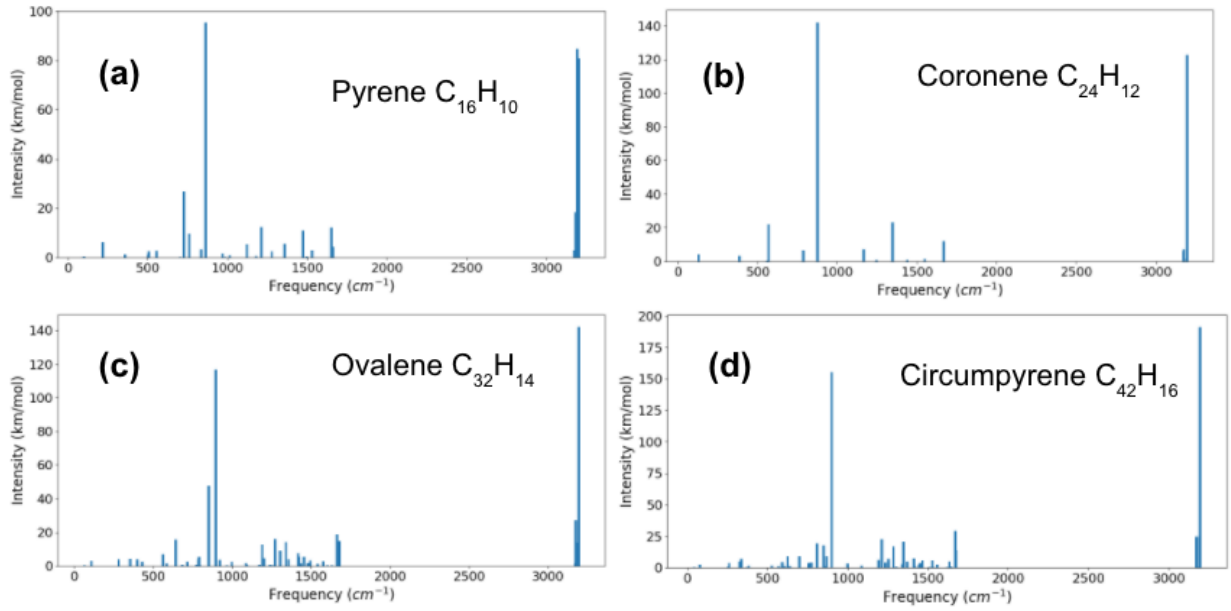

Figure 5.6: Vibrational transitions in (a) Pyrene, (b) Coronene, (c) Ovalene and (d) Circumpyrene.

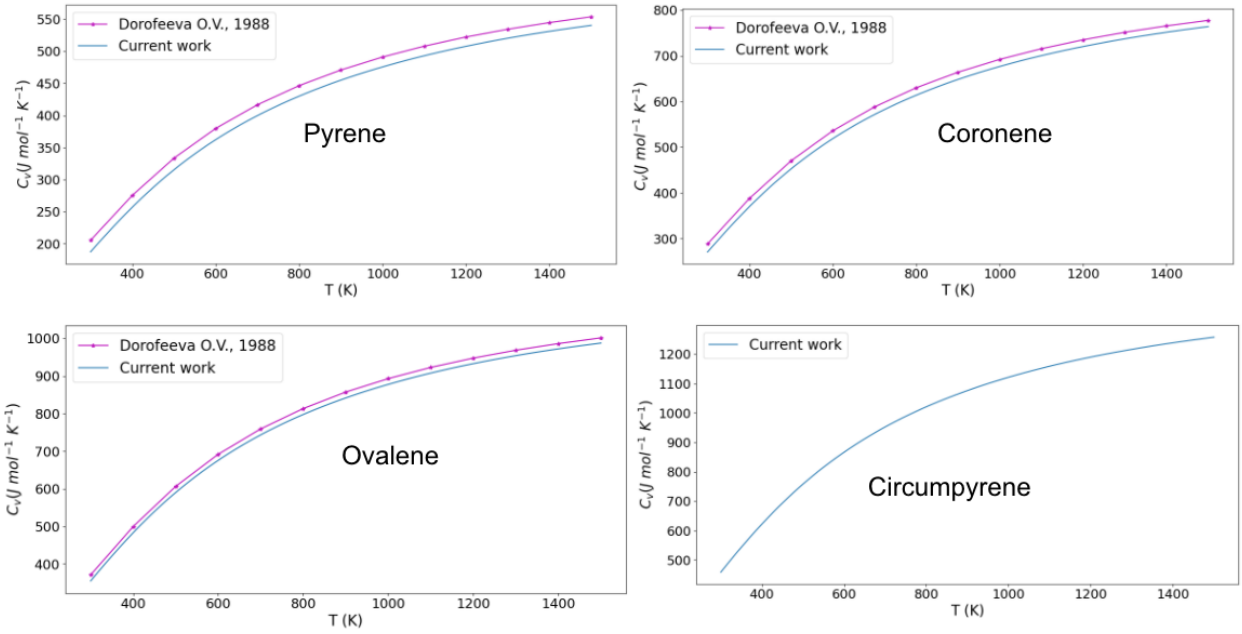

Figure 5.7: Specific heat of (a) Pyrene, (b) Coronene, (c) Ovalene and (d) Circumpyrene. The calculated results are comapred with [125].

CHAPTER 6

Summary

This dissertation concerns the study of interactions between quantum particles and their effects on thermal transport at surfaces and interfaces. Three major interactions are considered in this work:

• Electron-phonon interaction in bilayer graphene is computed and its effect on photoconductivity is calculated for bilayer graphene with different doping levels.

• Magnon-phonon interaction in a Co/Cu interface is considered through the Heisenberg exchange interaction. We calculate the thermal boundary conductance across the interface using equilibrium molecular dynamics and the non-equilibrium Green's function method, respectively.

• Electron-electron screening in armchair graphene nanoribbons is calculated using the GW method. We include the electron-hole interaction in predicting the optical absorption spectra by solving the Bethe-Salpeter equation.

The contribution of this work is summarized below in three sections.

6.1 Modeling of electron-phonon interaction and photoconductivity

This work investigates electron-phonon coupling in bilayer graphene and its effect on photoconductivity. The contribution from this work is summarized below.

• Electron-phonon coupling constants are computed with DFPT and interpolated to a denser grid using Wannier interpolation. The electron scattering rates due to the phonon interaction is then calculated based on Fermi's golden rule using the previously obtained electron-phonon coupling constants. We have found that in intrinsic bilayer graphene at 300 K near the phonon Γ point, LA$'$ and TA$'$ modes dominate the electron-phonon scattering for electronic states with energies lower

than 200 meV. LO and TO modes only participate in phonon emission process at both phonon Γ and K points because phonons of energies higher than 200 meV are not excited at 300 K.

• By fixing the phonon temperature at 300 K and increasing the electron temperature from 300 K to 700 K, the emission of optical phonons at phonon Γ point increases for electrons with low energies. At phonon K point, TO branch phonon absorption process starts to appear due to expansion of the Fermi window at higher electron temperatures. The rise of electron temperature increases the electron-phonon scattering rates at low energies but the most contribution comes from the TO mode phonons while the acoustic modes barely feel the increase of electron temperature.

• We assume the initial electron temperature to be 2000 K and initial phonon temperature to be 300 K. The evolution of temperature is calculated based on a two-temperature model and the heat transfter from electrons to phonons is computed in a similar way as the scattering rates based on Fermi's golden rule. In a bilayer graphene with Fermi level 10 meV, the electron temperature drops rapidly in the first 0.4 ps. Phonon temperature remains around 300 K during the whole relaxation process due to large heat capacity. Most of the energy is transferred to optical phonons near the phonon K point.

• Photoconductivities in bilayer graphene with different doping levels are calculated based on a Drude model with the previously obtained scattering rates, electron temperatures and phonon temperatures. The case $E_{fermi} = 10$ meV matches the experiment best in both the trend and intersection of the real and imaginary parts at all four times considered.

• Deformation potentials for acoustic and optical phonon modes are derived from a semiclassical deformation-potential approach. Photoconductivity calculated from the derived deformation potentials shows a large deviation from experimental values which indicates that the momentum-dependent electron-phonon scattering potential and scattering rates are important in photoconductivity calculations.

In the present work, we consider intrinsic electron-phonon coupling in bilayer graphene; however, the interaction between electrons and phonons in the substrate exists in reality. To better compare the simulations with experiments, electron-phonon coupling between bilayer graphene and substrates could be included in future work. The current work deals with pure bilayer graphene

and the doping level is varied from 0 meV to 60 meV. In the future, defects and their effect on electronic structures and electron-phonon scattering rates should be considered. The initial electron temperature is an estimate in this work, the accurate electron temperature should be obtained from the ultra fast electron relaxation process.

6.2 Modeling of magnon-phonon interaction and thermal boundary conductance

This work focuses on the magnon-phonon interaction within bulk materials and across interfaces. Thermal boundary conductance is calculated considering magnon-phonon interaction and phonon-phonon interaction. The major contribution is summarized below.

• Electronic band structure of fcc cobalt is computed using the spin-polarised scalar relativistic KKR Green's function method and the Heisenberg exchange constants are calculated using the Lichtenstein formula with single site t-matrix and scattering path matrix obtained from KKR Green's function within the atomic sphere approximation. The computed Heisenberg exchange constants are further fitted to a continuous Bethe-Slater curve.

• Thermal conductivity of bulk fcc cobalt is calculated by running spin-lattice dynamics with the previously obtained exchange interaction between spins. Thermal conductivity of fcc cobalt contributed by magnons is comparable to that contributed by phonons. The effect of spins is small on phonon thermal conductivities. Increasing the temperature reduces both magnon and phonon thermal conductivities but the reduction is more significant for magnons.

• Electronic and magnetic properties of a supercell consisting of 8 layers cobalt and 8 layers copper atoms are computed using KKR Green's function method, similar to bulk cobalt. The copper layers next to the interface are magnetized and there is a weak exchange interaction between copper and cobalt atoms near the interface.

• Thermal boundary conductance of the Co/Cu interface is calculated based on fluctuation-dissipation theorem using the heat flux obtained from equilibrium spin-lattice dynamics. The inclusion of magnons decreases the interfacial thermal conductance due to magnon-phonon in-

teraction inside the cobalt contact. Spin waves are not effectively transmitted across the interface even though the copper layers next to the interface weakly interact with cobalt layers on the other side of the interface.

• NEGF calculations are conducted and the inelastic scattering is accounted for by attaching Büttiker probes to atoms. The scattering rates are obtained by fitting bulk Co and Cu thermal conductivities computed from equilibrium spin-lattice dynamics. The heat flux in Co and Cu contacts increases with magnon effects but the normalized accumulated heat flux is not significantly modulated in the entire frequency range in the presence of magnon effects. The NEGF method shows a similar trend for thermal boundary conductance as the EMD method.

In this work, the magnon-phonon interaction is weak across the Co/Cu interface. The thermal conductance contributed by magnons is small compared with phonons, due to the little acoustic impedance mismatch between Co and Cu and the weak interaction between Co layers and Cu layers at the interface. Future work could be extending the methodology developed in this work to other material systems and searching for an interface where magnon-phonon interaction plays an important role in thermal boundary conductance. The inelastic scattering rates in the NEGF method are obtained by fitting bulk thermal conductivities; however, more accurate scattering rates could be calculated from third-order force constants.

6.3 Modeling of electron-electron screening and optical response

This work focuses on optical response of graphene nanoribbons and studies the effect of widths and edge alignments on the absorption spectra. The contribution from this work is summarized as below.

• Electronic band structures of single layer armchair graphene nanoribbons are computed using the GW method considering the electron-electron screening effect with ground-state energies and wave functions obtained from static DFT. Band gaps of graphene nanoribbons decrease with width. The $3n+1$ family has the largest band gaps and the corrections due to many-body effects are the most significant among three families studied.

• Dielectric functions are calculated considering the electron-hole interaction by solving the Bethe-Salpeter equation. The peaks in the real and imaginary part of dielectric functions shift to lower photon energies with increasing widths and the $3n+1$ family has highest onset photon energies, showing a similar trend as band gaps.

• The inclusion of the electron-hole interaction significantly shifts the absorption peaks to lower incident photon energies. Large exciton binding energies are also observed. The exciton wave functions in $3n+2$ family graphene nanoribbons are most delocalized, indicating the most π-conjugation. This is consistent with the smallest band gaps, lowest onset energy in the absorption spectra and the smallest exciton binding energies.

• Electronic and optical properties of bilayer graphene nanoribbons are calculated and compared to single layer graphene nanoribbons. Two alignments are considered: the α alignment and the β alignment. Bilayer α alignment nanoribbons have smaller band gaps and lower onset absorption energies than the bilayer β alignment nanoribbons and single layer nanoribbons of same widths. The optical properties of graphene nanoribbons could be tuned by vary widths, number of layers and edge alignments.

REFERENCES

[1] Q. Ma *et al.*, "Giant intrinsic photoresponse in pristine graphene," *Nature nanotechnology*, vol. 14, no. 2, p. 145, 2019.

[2] M. Sigrist and K. Ueda, "Phenomenological theory of unconventional superconductivity," *Reviews of Modern physics*, vol. 63, no. 2, p. 239, 1991.

[3] P. B. Allen and B. Mitrović, "Theory of superconducting tc," in *Solid state physics*, vol. 37, Elsevier, 1983, pp. 1–92.

[4] E. R. Margine and F. Giustino, "Anisotropic migdal-eliashberg theory using wannier functions," *Physical Review B*, vol. 87, no. 2, p. 024 505, 2013.

[5] S. Sadasivam *et al.*, "Thermal transport across metal silicide-silicon interfaces: First-principles calculations and green's function transport simulations," *Physical Review B*, vol. 95, no. 8, p. 085 310, 2017.

[6] K Uchida *et al.*, "Observation of the spin seebeck effect," *Nature*, vol. 455, no. 7214, pp. 778–781, 2008.

[7] E Saitoh, M Ueda, H Miyajima, and G Tatara, "Conversion of spin current into charge current at room temperature: Inverse spin-hall effect," *Applied physics letters*, vol. 88, no. 18, p. 182 509, 2006.

[8] S. O. Valenzuela and M Tinkham, "Direct electronic measurement of the spin hall effect," *Nature*, vol. 442, no. 7099, pp. 176–179, 2006.

[9] S. Wolf *et al.*, "Spintronics: A spin-based electronics vision for the future," *science*, vol. 294, no. 5546, pp. 1488–1495, 2001.

[10] I. Žutić, J. Fabian, and S. D. Sarma, "Spintronics: Fundamentals and applications," *Reviews of modern physics*, vol. 76, no. 2, p. 323, 2004.

[11] C. Chappert, A. Fert, and F. N. Van Dau, "The emergence of spin electronics in data storage," in *Nanoscience And Technology: A Collection of Reviews from Nature Journals*, World Scientific, 2010, pp. 147–157.

[12] K.-i. Uchida, H. Adachi, T. Ota, H. Nakayama, S. Maekawa, and E. Saitoh, "Observation of longitudinal spin-seebeck effect in magnetic insulators," *Applied Physics Letters*, vol. 97, no. 17, p. 172 505, 2010.

[13] J. Xiao, G. E. Bauer, K.-c. Uchida, E. Saitoh, S. Maekawa, *et al.*, "Theory of magnon-driven spin seebeck effect," *Physical Review B*, vol. 81, no. 21, p. 214 418, 2010.

[14] H. Adachi, J.-i. Ohe, S. Takahashi, and S. Maekawa, "Linear-response theory of spin seebeck effect in ferromagnetic insulators," *Physical Review B*, vol. 83, no. 9, p. 094 410, 2011.

[15] K.-i. Uchida *et al.*, "Long-range spin seebeck effect and acoustic spin pumping," *Nature materials*, vol. 10, no. 10, pp. 737–741, 2011.

[16] R. M. Wentzcovitch, W. W. Schulz, and P. B. Allen, "Vo 2: Peierls or mott-hubbard? a view from band theory," *Physical review letters*, vol. 72, no. 21, p. 3389, 1994.

[17] M. M. Qazilbash *et al.*, "Mott transition in vo2 revealed by infrared spectroscopy and nano-imaging," *Science*, vol. 318, no. 5857, pp. 1750–1753, 2007.

[18] J. P. Perdew, "Density functional theory and the band gap problem," *International Journal of Quantum Chemistry*, vol. 28, no. S19, pp. 497–523, 1985.

[19] J. P. Perdew *et al.*, "Understanding band gaps of solids in generalized kohn–sham theory," *Proceedings of the national academy of sciences*, vol. 114, no. 11, pp. 2801–2806, 2017.

[20] E. Runge and E. K. Gross, "Density-functional theory for time-dependent systems," *Physical Review Letters*, vol. 52, no. 12, p. 997, 1984.

[21] S. Baroni, P. Giannozzi, and A. Testa, "Green's-function approach to linear response in solids," *Physical Review Letters*, vol. 58, no. 18, p. 1861, 1987.

[22] D. Pines and D. Bohm, "A collective description of electron interactions: Ii. collective vs individual particle aspects of the interactions," *Physical Review*, vol. 85, no. 2, p. 338, 1952.

[23] D. Bohm and D. Pines, "A collective description of electron interactions: Iii. coulomb interactions in a degenerate electron gas," *Physical Review*, vol. 92, no. 3, p. 609, 1953.

[24] H.-C. Weissker *et al.*, "Dynamic structure factor and dielectric function of silicon for finite momentum transfer: Inelastic x-ray scattering experiments and ab initio calculations," *Physical Review B*, vol. 81, no. 8, p. 085 104, 2010.

[25] G. Onida, L. Reining, and A. Rubio, "Electronic excitations: Density-functional versus many-body green's-function approaches," *Reviews of modern physics*, vol. 74, no. 2, p. 601, 2002.

[26] E. K. Gross and N. T. Maitra, "Introduction to tddft," in *Fundamentals of Time-Dependent Density Functional Theory*, Springer, 2012, pp. 53–99.

[27] L. Hedin, "New method for calculating the one-particle green's function with application to the electron-gas problem," *Physical Review*, vol. 139, no. 3A, A796, 1965.

[28] M. S. Hybertsen and S. G. Louie, "Electron correlation in semiconductors and insulators: Band gaps and quasiparticle energies," *Physical Review B*, vol. 34, no. 8, p. 5390, 1986.

[29] F. Aryasetiawan and O. Gunnarsson, "The gw method," *Reports on Progress in Physics*, vol. 61, no. 3, p. 237, 1998.

[30] L. Hedin and S. Lundqvist, "Effects of electron-electron and electron-phonon interactions on the one-electron states of solids," in *Solid state physics*, vol. 23, Elsevier, 1970, pp. 1–181.

[31] S. Albrecht, L. Reining, R. Del Sole, and G. Onida, "Ab initio calculation of excitonic effects in the optical spectra of semiconductors," *Physical review letters*, vol. 80, no. 20, p. 4510, 1998.

[32] M. Rohlfing and S. G. Louie, "Electron-hole excitations in semiconductors and insulators," *Physical review letters*, vol. 81, no. 11, p. 2312, 1998.

[33] G. Strinati, "Application of the green's functions method to the study of the optical properties of semiconductors," *La Rivista del Nuovo Cimento (1978-1999)*, vol. 11, no. 12, pp. 1–86, 1988.

[34] W Hanke and L. Sham, "Dielectric response in the wannier representation: Application to the optical spectrum of diamond," *Physical Review Letters*, vol. 33, no. 10, p. 582, 1974.

[35] ——, "Local-field and excitonic effects in the optical spectrum of a covalent crystal," *Physical Review B*, vol. 12, no. 10, p. 4501, 1975.

[36] ——, "Many-particle effects in the optical spectrum of a semiconductor," *Physical Review B*, vol. 21, no. 10, p. 4656, 1980.

[37] M. Rohlfing and S. G. Louie, "Electron-hole excitations and optical spectra from first principles," *Physical Review B*, vol. 62, no. 8, p. 4927, 2000.

[38] F. Giustino, "Electron-phonon interactions from first principles," *Reviews of Modern Physics*, vol. 89, no. 1, p. 015 003, 2017.

[39] N. W. Ashcroft and N. D. Mermin, "Solid state physics (saunders college, philadelphia, 1976)," *Appendix N*, 2010.

[40] M. Ležaić, P. Mavropoulos, G. Bihlmayer, and S. Blügel, "Exchange interactions and local-moment fluctuation corrections in ferromagnets at finite temperatures based on non-

collinear density-functional calculations," *Physical Review B*, vol. 88, no. 13, p. 134 403, 2013.

[41] A. Liechtenstein, M. Katsnelson, and V. Gubanov, "Exchange interactions and spin-wave stiffness in ferromagnetic metals," *Journal of Physics F: Metal Physics*, vol. 14, no. 7, p. L125, 1984.

[42] J Korringa, "On the calculation of the energy of a bloch wave in a metal," *Physica*, vol. 13, no. 6-7, pp. 392–400, 1947.

[43] W. Kohn and N. Rostoker, "Solution of the schrödinger equation in periodic lattices with an application to metallic lithium," *Physical Review*, vol. 94, no. 5, p. 1111, 1954.

[44] T. H. Dupree, "Electron scattering in a crystal lattice," *Annals of Physics*, vol. 15, no. 1, pp. 63–78, 1961.

[45] G. Morgan, "Bloch waves and scattering by impurities," *Proceedings of the Physical Society (1958-1967)*, vol. 89, no. 2, p. 365, 1966.

[46] A. Gonis, "Green functions for ordered and disordered systems," 1992.

[47] A. Gonis and W. H. Butler, *Multiple scattering in solids*. Springer Science & Business Media, 1999.

[48] J Braun, "The theory of angle-resolved ultraviolet photoemission and its applications to ordered materials," *Reports on Progress in Physics*, vol. 59, no. 10, p. 1267, 1996.

[49] H Ebert and S Man'kovsky, "Field-induced magnetic circular x-ray dichroism in paramagnetic solids: A new magneto-optical effect," *Physical review letters*, vol. 90, no. 7, p. 077 404, 2003.

[50] H Ebert, "Magneto-optical effects in transition metal systems," *Reports on Progress in Physics*, vol. 59, no. 12, p. 1665, 1996.

[51] P. Mavropoulos, O. Wunnicke, and P. H. Dederichs, "Ballistic spin injection and detection in fe/semiconductor/fe junctions," *Physical Review B*, vol. 66, no. 2, p. 024 416, 2002.

[52] N Papanikolaou, J Opitz, P Zahn, and I Mertig, "Spin-filter effect in metallic nanowires," *Physical Review B*, vol. 66, no. 16, p. 165 441, 2002.

[53] P. Soven, "Coherent-potential model of substitutional disordered alloys," *Physical Review*, vol. 156, no. 3, p. 809, 1967.

[54] I. Turek, V. Drchal, J. Kudrnovskỳ, M. Sob, and P. Weinberger, *Electronic structure of disordered alloys, surfaces and interfaces*. Springer Science & Business Media, 1997.

[55] R. Elliott, J. Krumhansl, and P. Leath, "The theory and properties of randomly disordered crystals and related physical systems," *Reviews of modern physics*, vol. 46, no. 3, p. 465, 1974.

[56] W. J. Yu, L. Liao, S. H. Chae, Y. H. Lee, and X. Duan, "Toward tunable band gap and tunable dirac point in bilayer graphene with molecular doping," *Nano Letters*, vol. 11, no. 11, pp. 4759–4763, 2011.

[57] Y. Zhang *et al.*, "Direct observation of a widely tunable bandgap in bilayer graphene," *Nature*, vol. 459, no. 7248, p. 820, 2009.

[58] F. Bonaccorso, Z Sun, T. Hasan, and A. Ferrari, "Graphene photonics and optoelectronics," *Nature Photonics*, vol. 4, no. 9, p. 611, 2010.

[59] Q. Bao and K. P. Loh, "Graphene photonics, plasmonics, and broadband optoelectronic devices," *ACS Nano*, vol. 6, no. 5, pp. 3677–3694, 2012.

[60] K.-J. Tielrooij *et al.*, "Photoexcitation cascade and multiple hot-carrier generation in graphene," *Nature Physics*, vol. 9, no. 4, p. 248, 2013.

[61] P. A. George *et al.*, "Ultrafast optical-pump terahertz-probe spectroscopy of the carrier relaxation and recombination dynamics in epitaxial graphene," *Nano Letters*, vol. 8, no. 12, pp. 4248–4251, 2008.

[62] S. Kar, V. L. Nguyen, D. R. Mohapatra, Y. H. Lee, and A. Sood, "Ultrafast spectral photoresponse of bilayer graphene: Optical pump–terahertz probe spectroscopy," *ACS Nano*, vol. 12, no. 2, pp. 1785–1792, 2018.

[63] T. Ohta, A. Bostwick, J. L. McChesney, T. Seyller, K. Horn, and E. Rotenberg, "Interlayer interaction and electronic screening in multilayer graphene investigated with angle-resolved photoemission spectroscopy," *Physical Review Letters*, vol. 98, no. 20, p. 206 802, 2007.

[64] S.-i. Tanaka, M. Matsunami, and S.-i. Kimura, "An investigation of electron-phonon coupling via phonon dispersion measurements in graphite using angle-resolved photoelectron spectroscopy," *Scientific Reports*, vol. 3, p. 3031, 2013.

[65] S.-F. Shi *et al.*, "Controlling graphene ultrafast hot carrier response from metal-like to semiconductor-like by electrostatic gating," *Nano Letters*, vol. 14, no. 3, pp. 1578–1582, 2014.

[66] A. Frenzel, C. Lui, Y. Shin, J Kong, and N Gedik, "Semiconducting-to-metallic photoconductivity crossover and temperature-dependent drude weight in graphene," *Physical Review Letters*, vol. 113, no. 5, p. 056 602, 2014.

[67] J. Heyman, J. Stein, Z. Kaminski, A. Banman, A. Massari, and J. Robinson, "Carrier heating and negative photoconductivity in graphene," *Journal of Applied Physics*, vol. 117, no. 1, p. 015 101, 2015.

[68] S. Adam and S. D. Sarma, "Boltzmann transport and residual conductivity in bilayer graphene," *Physical Review B*, vol. 77, no. 11, p. 115 436, 2008.

[69] A. Ferreira, J Viana-Gomes, J. Nilsson, E. R. Mucciolo, N. M. Peres, and A. C. Neto, "Unified description of the dc conductivity of monolayer and bilayer graphene at finite densities based on resonant scatterers," *Physical Review B*, vol. 83, no. 16, p. 165 402, 2011.

[70] J. Viljas and T. Heikkilä, "Electron-phonon heat transfer in monolayer and bilayer graphene," *Physical Review B*, vol. 81, no. 24, p. 245 404, 2010.

[71] C.-H. Park, F. Giustino, M. L. Cohen, and S. G. Louie, "Electron- phonon interactions in graphene, bilayer graphene, and graphite," *Nano Letters*, vol. 8, no. 12, pp. 4229–4233, 2008.

[72] S. Baroni, S. De Gironcoli, A. Dal Corso, and P. Giannozzi, "Phonons and related crystal properties from density-functional perturbation theory," *Reviews of Modern Physics*, vol. 73, no. 2, p. 515, 2001.

[73] P. K. Lam, M. M. Dacorogna, and M. L. Cohen, "Self-consistent calculation of electron-phonon couplings," *Physical Review B*, vol. 34, no. 8, p. 5065, 1986.

[74] P. B. Allen, "Theory of thermal relaxation of electrons in metals," *Physical review letters*, vol. 59, no. 13, p. 1460, 1987.

[75] T. Low, V. Perebeinos, R. Kim, M. Freitag, and P. Avouris, "Cooling of photoexcited carriers in graphene by internal and substrate phonons," *Physical Review B*, vol. 86, no. 4, p. 045 413, 2012.

[76] A. K. Vallabhaneni, D. Singh, H. Bao, J. Murthy, and X. Ruan, "Reliability of raman measurements of thermal conductivity of single-layer graphene due to selective electron-phonon coupling: A first-principles study," *Physical Review B*, vol. 93, no. 12, p. 125 432, 2016.

[77] J Bardeen and W Shockley, "Deformation potentials and mobilities in non-polar crystals," *Physical Review*, vol. 80, no. 1, p. 72, 1950.

[78] M. Lundstrom, *Fundamentals of carrier transport*. Cambridge university press, 2009.

[79] E. Hwang and S. D. Sarma, "Acoustic phonon scattering limited carrier mobility in two-dimensional extrinsic graphene," *Physical Review B*, vol. 77, no. 11, p. 115 449, 2008.

[80] P. Giannozzi *et al.*, "Quantum espresso: A modular and open-source software project for quantum simulations of materials," *Journal of physics: Condensed matter*, vol. 21, no. 39, p. 395 502, 2009.

[81] S. Poncé, E. R. Margine, C. Verdi, and F. Giustino, "Epw: Electron–phonon coupling, transport and superconducting properties using maximally localized wannier functions," *Computer Physics Communications*, vol. 209, pp. 116–133, 2016.

[82] K. Kaasbjerg, K. S. Thygesen, and K. W. Jacobsen, "Unraveling the acoustic electron-phonon interaction in graphene," *Physical Review B*, vol. 85, no. 16, p. 165 440, 2012.

[83] K Uchida *et al.*, "Spin seebeck insulator," *Nature materials*, vol. 9, no. 11, p. 894, 2010.

[84] Y Kajiwara *et al.*, "Transmission of electrical signals by spin-wave interconversion in a magnetic insulator," *Nature*, vol. 464, no. 7286, p. 262, 2010.

[85] K Uchida *et al.*, "Thermal spin pumping and magnon-phonon-mediated spin-seebeck effect," *Journal of Applied Physics*, vol. 111, no. 10, p. 103 903, 2012.

[86] C. Jaworski, J Yang, S Mack, D. Awschalom, R. Myers, and J. Heremans, "Spin-seebeck effect: A phonon driven spin distribution," *Physical review letters*, vol. 106, no. 18, p. 186 601, 2011.

[87] Y. Zhou, J. Tranchida, Y. Ge, J. Murthy, and T. S. Fisher, "Atomistic simulation of phonon and magnon thermal transport across the ferromagnetic-paramagnetic transition," *Physical Review B*, vol. 101, no. 22, p. 224 303, 2020.

[88] Z.-Q. Zhang and J.-T. Lü, "Thermal transport through a spin-phonon interacting junction: A nonequilibrium green's function method study," *Physical Review B*, vol. 96, no. 12, p. 125 432, 2017.

[89] J. Tranchida, S. Plimpton, P. Thibaudeau, and A. P. Thompson, "Massively parallel symplectic algorithm for coupled magnetic spin dynamics and molecular dynamics," *Journal of Computational Physics*, vol. 372, pp. 406–425, 2018.

[90] S. Plimpton, "Fast parallel algorithms for short-range molecular dynamics," *Journal of computational physics*, vol. 117, no. 1, pp. 1–19, 1995.

[91] K.-H. Yang and J. O. Hirschfelder, "Generalizations of classical poisson brackets to include spin," *Physical Review A*, vol. 22, no. 5, p. 1814, 1980.

[92] R. Kubo, "The fluctuation-dissipation theorem," *Reports on progress in physics*, vol. 29, no. 1, p. 255, 1966.

[93] M. Anantram, M. S. Lundstrom, and D. E. Nikonov, "Modeling of nanoscale devices," *Proceedings of the IEEE*, vol. 96, no. 9, pp. 1511–1550, 2008.

[94] H Ebert *et al.*, *The munich spr-kkr package version 3.6 http://olymp. cup. unimuenchen. de/ak/ebert*, 2005.

[95] O. K. Andersen, "Linear methods in band theory," *Physical Review B*, vol. 12, no. 8, p. 3060, 1975.

[96] S. H. Vosko, L. Wilk, and M. Nusair, "Accurate spin-dependent electron liquid correlation energies for local spin density calculations: A critical analysis," *Canadian Journal of physics*, vol. 58, no. 8, pp. 1200–1211, 1980.

[97] A. I. Liechtenstein, M. Katsnelson, V. Antropov, and V. Gubanov, "Local spin density functional approach to the theory of exchange interactions in ferromagnetic metals and alloys," *Journal of Magnetism and Magnetic Materials*, vol. 67, no. 1, pp. 65–74, 1987.

[98] L Puech, G Bonfait, and B Castaing, "Mobility of the 3 he solid-liquid interface: Experiment and theory," *Journal of low temperature physics*, vol. 62, no. 3-4, pp. 315–327, 1986.

[99] F. Xia, T. Mueller, Y.-m. Lin, A. Valdes-Garcia, and P. Avouris, "Ultrafast graphene photodetector," *Nature nanotechnology*, vol. 4, no. 12, pp. 839–843, 2009.

[100] X. Yu, Z. Dong, J. K. Yang, and Q. J. Wang, "Room-temperature mid-infrared photodetector in all-carbon graphene nanoribbon-c 60 hybrid nanostructure," *Optica*, vol. 3, no. 9, pp. 979–984, 2016.

[101] J. Yu *et al.*, "Dynamic control of high-range photoresponsivity in a graphene nanoribbon photodetector," *Nanoscale Research Letters*, vol. 15, no. 1, pp. 1–9, 2020.

[102] S. Ogawa *et al.*, "Broadband photoresponse of graphene photodetector from visible to long-wavelength infrared wavelengths," *Optical Engineering*, vol. 58, no. 5, p. 057 106, 2019.

[103] Y. Zhang *et al.*, "Broadband high photoresponse from pure monolayer graphene photodetector," *Nature communications*, vol. 4, no. 1, pp. 1–11, 2013.

[104] C. Xie *et al.*, "Schottky solar cells based on graphene nanoribbon/multiple silicon nanowires junctions," *Applied Physics Letters*, vol. 100, no. 19, p. 193 103, 2012.

[105] N. Yang, J. Zhai, D. Wang, Y. Chen, and L. Jiang, "Two-dimensional graphene bridges enhanced photoinduced charge transport in dye-sensitized solar cells," *ACS nano*, vol. 4, no. 2, pp. 887–894, 2010.

[106] H. Zhang, X. Lv, Y. Li, Y. Wang, and J. Li, "P25-graphene composite as a high performance photocatalyst," *ACS nano*, vol. 4, no. 1, pp. 380–386, 2010.

[107] Q. Li *et al.*, "Highly efficient visible-light-driven photocatalytic hydrogen production of cds-cluster-decorated graphene nanosheets," *Journal of the American Chemical Society*, vol. 133, no. 28, pp. 10 878–10 884, 2011.

[108] A. Narita *et al.*, "Synthesis of structurally well-defined and liquid-phase-processable graphene nanoribbons," *Nature chemistry*, vol. 6, no. 2, pp. 126–132, 2014.

[109] S. Zhao *et al.*, "Optical imaging and spectroscopy of atomically precise armchair graphene nanoribbons," *Nano letters*, vol. 20, no. 2, pp. 1124–1130, 2020.

[110] R. Denk *et al.*, "Exciton-dominated optical response of ultra-narrow graphene nanoribbons," *Nature communications*, vol. 5, no. 1, pp. 1–7, 2014.

[111] C. Bronner, D. Gerbert, A. Broska, and P. Tegeder, "Excitonic states in narrow armchair graphene nanoribbons on gold surfaces," *The Journal of Physical Chemistry C*, vol. 120, no. 45, pp. 26 168–26 172, 2016.

[112] D. Prezzi, D. Varsano, A. Ruini, A. Marini, and E. Molinari, "Optical properties of graphene nanoribbons: The role of many-body effects," *Physical Review B*, vol. 77, no. 4, p. 041 404, 2008.

[113] L. Yang, M. L. Cohen, and S. G. Louie, "Excitonic effects in the optical spectra of graphene nanoribbons," *Nano letters*, vol. 7, no. 10, pp. 3112–3115, 2007.

[114] A. Wright, J. Cao, and C Zhang, "Enhanced optical conductivity of bilayer graphene nanoribbons in the terahertz regime," *Physical review letters*, vol. 103, no. 20, p. 207 401, 2009.

[115] M. De Corato, C. Cocchi, D. Prezzi, M. J. Caldas, E. Molinari, and A. Ruini, "Optical properties of bilayer graphene nanoflakes," *The Journal of Physical Chemistry C*, vol. 118, no. 40, pp. 23 219–23 225, 2014.

[116] Y. Ho, J. Wu, Y. Chiu, J Wang, and M.-F. Lin, "Electronic and optical properties of monolayer and bilayer graphene," *Philosophical Transactions of the Royal Society A: Mathematical, Physical and Engineering Sciences*, vol. 368, no. 1932, pp. 5445–5458, 2010.

[117] B.-L. Huang, C.-P. Chuu, and M.-F. Lin, "Asymmetry-enriched electronic and optical properties of bilayer graphene," *Scientific reports*, vol. 9, no. 1, pp. 1–12, 2019.

[118] W. Kohn and L. J. Sham, "Self-consistent equations including exchange and correlation effects," *Physical review*, vol. 140, no. 4A, A1133, 1965.

[119] J. Deslippe, G. Samsonidze, D. A. Strubbe, M. Jain, M. L. Cohen, and S. G. Louie, "Berkeleygw: A massively parallel computer package for the calculation of the quasiparticle and optical properties of materials and nanostructures," *Computer Physics Communications*, vol. 183, no. 6, pp. 1269–1289, 2012.

[120] S. Mukherjee *et al.*, "Hot electrons do the impossible: Plasmon-induced dissociation of h2 on au," *Nano letters*, vol. 13, no. 1, pp. 240–247, 2013.

[121] R. Costi, A. E. Saunders, E. Elmalem, A. Salant, and U. Banin, "Visible light-induced charge retention and photocatalysis with hybrid cdse- au nanodumbbells," *Nano Letters*, vol. 8, no. 2, pp. 637–641, 2008.

[122] H. Robatjazi *et al.*, "Plasmon-induced selective carbon dioxide conversion on earth-abundant aluminum-cuprous oxide antenna-reactor nanoparticles," *Nature communications*, vol. 8, no. 1, pp. 1–10, 2017.

[123] X. Zhang *et al.*, "Plasmon-enhanced catalysis: Distinguishing thermal and nonthermal effects," *Nano letters*, vol. 18, no. 3, pp. 1714–1723, 2018.

[124] M. Abuseada, C. Wei, R. M. Spearrin, and T. S. Fisher, "Solar–thermal production of graphitic carbon and hydrogen via methane decomposition," *Energy & Fuels*, 2021.

[125] O. Dorofeeva, "Thermodynamic properties of polycyclic aromatic hydrocarbons in the gaseous phase," *Institute for High Temperatures, USSR Academy of Sciences: Moscow*, 1988.